

Mesoscale Modeling of Phase Behavior in Thin Films of Cylinder-Forming ABA Block Copolymers

DISSERTATION

zur Erlangung des akademischen Grades eines
Doktors der Naturwissenschaften
- Dr. rer. nat. -

im Fach Chemie der Fakultät Biologie, Chemie und Geowissenschaften
der Universität Bayreuth

vorgelegt von
Andriana Horvat
geboren in Uzhgorod, Ukraine

Bayreuth, 2008

Erklärung

Die vorliegende Arbeit wurde von mir selbstständig verfasst und ich habe dabei keine anderen als die angegebenen Hilfsmittel und Quellen benutzt. Ferner habe ich nicht versucht, anderweitig mit oder ohne Erfolg eine Dissertation einzureichen oder mich der Doktorprüfung zu unterziehen.

Bayreuth, den 01.12.2009

Andriana Horvat

Die vorliegende Arbeit wurde in der Zeit von November 2000 bis Juli 2008 am Lehrstuhl für Physikalische Chemie der Universität Bayreuth angefertigt.

Prüfungsausschuss:

Prof. Dr. M.Ballauff (Erstgutachter)

Prof. Dr. G.Krausch (Zweitgutachter)

Prof. Dr. P.Strohriegl (Vorsitzender)

Prof. Dr. M. Thelakkat

Tag der Einreichung: 16.07.2008

Tag der Prüfung: 12.01.2009

Vollständiger Abdruck der von der Fakultät für Biologie, Chemie und Geowissenschaften der Universität Bayreuth genehmigten Dissertation zur Erlangung des Grades eines Doktors der Naturwissenschaften (Dr. rer. nat.).

*Whatever the coordinate system, the physics
of the system remains unaltered.*

Ilya Prigogine, Nobel lecture 1977.

Contents

1	Motivation and aim of the thesis	1
2	Method	4
2.1	Coarse-grained models of a block copolymer chain	4
2.2	Field theoretic calculation	6
2.3	Thin films of block copolymers	10
2.4	Dynamic density functional theory: simulations	11
3	Overview of thesis	14
3.1	Results	14
3.2	Individual contribution of authors	21
4	Phase behavior in thin films of cylinder-forming <i>ABA</i> block copolymers: Mesoscale modeling	30
4.1	Introduction	30
4.2	Method	33
4.3	Results	34
4.3.1	Bulk structure	34
4.3.2	Surface reconstruction	36
4.3.3	One microdomain thick films	39
4.3.4	Phase diagrams of surface reconstructions	41
4.3.5	Structured wetting layer	43
4.4	Discussion	44
4.4.1	Mapping to the experimental phase diagram	44
4.4.2	Effect of the wetting layer	47
4.4.3	Comparison with cylinder forming diblock copolymers	48
4.4.4	Comparison with lamella-forming diblock copolymers	48
4.5	Conclusions	49
5	Phase behavior in thin films of cylinder-forming <i>ABA</i> block copolymers	52

6	Specific features of defect structure and dynamics in cylinder phase of block copolymers	61
6.1	Introduction	61
6.2	Results and Discussion	63
6.2.1	Phase Behavior in Thin Films.	63
6.2.2	Classification of Characteristic Defects.	64
6.2.3	Dynamics of Complex Defects.	72
6.3	Summary	76
6.4	Experimental Details	77
6.4.1	Polymer	77
6.4.2	Scanning Force Microscopy	77
6.4.3	Simulation	78
7	Structural Ordering in Thin Films of Cylinder Forming Block Copolymers	84
7.1	Introduction	84
7.2	Experimental	85
7.2.1	Polymer	85
7.2.2	Scanning Force Microscopy (SFM)	85
7.2.3	Experimental conditions	85
7.2.4	Simulations	85
7.3	Results	86
7.3.1	Transient perforated lamella phase (experiment)	86
7.3.2	Transient perforated lamella phase (simulations)	87
7.4	Discussion	89
8	Time evolution of surface relief structures in thin block copolymer films	92
8.1	Introduction	92
8.2	Method	94
8.2.1	Theoretical model	94
8.2.2	Simulation parameters of the free surface model	97
8.2.3	Experiment	99
8.3	Results	100
8.3.1	Film evolution in experiment	100
8.3.2	Simulation setup versus Experiment	102
8.3.3	Film evolution in simulation	104
8.4	Discussion	107
8.4.1	Comparison of simulation and experiment	107

8.4.2	Mechanisms of transitions, early and late stages	112
8.5	Conclusions	113
9	Summary	118

1 Motivation and aim of the thesis

Self-organization is a process of short-range attraction and long-range repulsion in which the internal organization of a system increases in complexity. It is driven by interparticle potentials and is opposed by the chaotic dynamics, characteristic of many non-equilibrium systems. In general, self-organization involves multiple time and length scales. Examples of self-organization can be found in behavior of social animals, in economic systems (free market economy), in mathematics and cybernetic, in biology and chemistry. The most robust and unambiguous examples of self-organizing systems are from physics and chemistry, where the term "self-organization" is often replaced by the synonymous term "self-assembly". Examples from physics include phase transitions, superconductivity and Bose-Einstein condensation, critical opalescence of fluids at the critical point, spontaneous magnetization *etc.* In chemical sciences, self-assembly is closely associated with soft matter, such as liquid crystals, colloidal crystals and phase-separated block copolymers. The last ones constitute one of the most widely studied classes of self-ordering complex fluids [1].

Block copolymers consist of two or more incompatible polymer chains (blocks) which are covalently bonded together. Due to the strong repulsion, unlike blocks tend to segregate. However, as they are chemically bounded, a macroscopic phase separation is prohibited. Instead, periodic microdomains of the size in the range from 5 to 100 nm are formed. Since the chemical identity of each block can be judiciously selected prior to copolymerization, the self-assembly of block copolymers offers one of the most general strategies for generating structures on the nanometer length scale. Therefore this class of materials opens new perspectives for modern nanoscience and nanotechnology.

Thin films of block copolymers are of particular technological interest, as the confined geometry offers additional possibilities to guide the self-assembly of nanostructures via interfacial interactions, symmetry breaking, structural frustration and confinement-induced entropy loss, resulting in richer phase behavior as compared to the bulk phase with the same composition. Nanostructured patterns from block copolymers are promising in applications as templates for nanolithography, nanowires, high-density storage devices, quantum dots, photonic crystals, nanostructured membranes, etc. [2, 3, 4, 5, 6, 7, 8, 9], where the size, shape and spatial arrangement of the self-assembled structures are utilized.

On the other side, thin films of block copolymers have proved to be suitable models for the fundamental studies of interfacial phenomena, as they offer an excellent possibility to visualize the structure and dynamics of microdomains in real time and real space [10, 11, 12]. Therefore, studies on thin block copolymer films provide a deeper understanding of mechanisms and interactions involved into self-assembly on a mesoscale, as well as of the processes of structural ordering observed in other complex systems, ranging from solid crystals [13] to membranes [14].

Indispensable for such understanding and control of the resulting nanostructures is the theoretical description of the related phenomena. Theoretical predictions rationalize and accelerate experimental studies and provide deeper understanding of processes observed experimentally. On the other hand, experiments test and validate theoretical assumptions.

In this thesis a detailed analysis of microdomain structure and their short- to long- term dynamics in thin films of asymmetric block copolymers is presented. The strength of this study is that the modeling results are directly compared with the experimental findings on block copolymer films with Scanning Force Microscopy (SFM).

The theoretical approach provides decisive understanding of the experimental results as it allows more extensive variation of the system parameters than one could achieve in experiments. Moreover, simulations allow time-resolved observation of the film structure beyond the surface layer to which the SFM experimental studies are limited.

The core of this work are the calculations based on the dynamic density functional theory (DDFT). The molecular model ($A_3B_{12}A_3$ Gaussian chain) was chosen to describe the comparative polystyrene-*block*-polybutadiene-*block*-polystyrene triblock copolymer, which has been studied experimentally with SFM by A. Knoll [15].

The first part of the work includes systematic investigation of the phase behavior of cylinder-forming block copolymers in thin films. The deviations from the cylinder bulk morphology, observed both, in simulations and in experiments, were identified as surface reconstructions. The phase diagrams of surface structures were constructed in a large parameter space covered by simulations. This allowed to distinguish between surface field and confinement effects in the observed phase behavior.

The advantage of DDFT method is that it provides the possibility to study the kinetics of structure development and related transport mechanisms in block copolymeric systems. This feature gave an impulse to establish *in-situ* SFM measurements [10] of the microdomain dynamics in thin block copolymer films.

The second part of this thesis presents a comparative study of the dynamics in thin films on two different length scales: the dynamics of individual defects (on a scale of nm) and the dynamics of surface relief structures (on a scale of several μm). The pathway of structure

formation and kinetics of phase transition give additional insight into the physics of the system. The accordance between the modeling and the experimental results supports the assumption that the material transport is governed by diffusion. Importantly, the good match between the simulations and the experiments validates the kinetic model applied in DDFT.

The new insights gained from the presented research expands the understanding of the equilibrium and dynamic behavior of block copolymers, and eventually provide means to control the nanostructures in ordered fluids.

2 Method

2.1 Coarse-grained models of a block copolymer chain

Block copolymers can be theoretically and computationally described by models pertaining to different length scales and corresponding time scales (Fig. 2.1). The level of details, resolution and degree of freedom in simulations can be done on different levels of the building blocks of a polymer chain: atoms, united atoms (chemical groups of a few atoms), monomers, groups of monomers, chain segments of various lengths and entire chain. The process of collecting many microscopic building blocks (or degrees of freedom) into fewer larger ones is referred to as coarse-graining. The choice of the smallest block in the model determines not only the spatial resolution, but also the corresponding time scales [16]. For example, atomistic models retain detailed information about the chemical composition of a single chain, but the time scales covered in atomistic simulations are some nanoseconds.

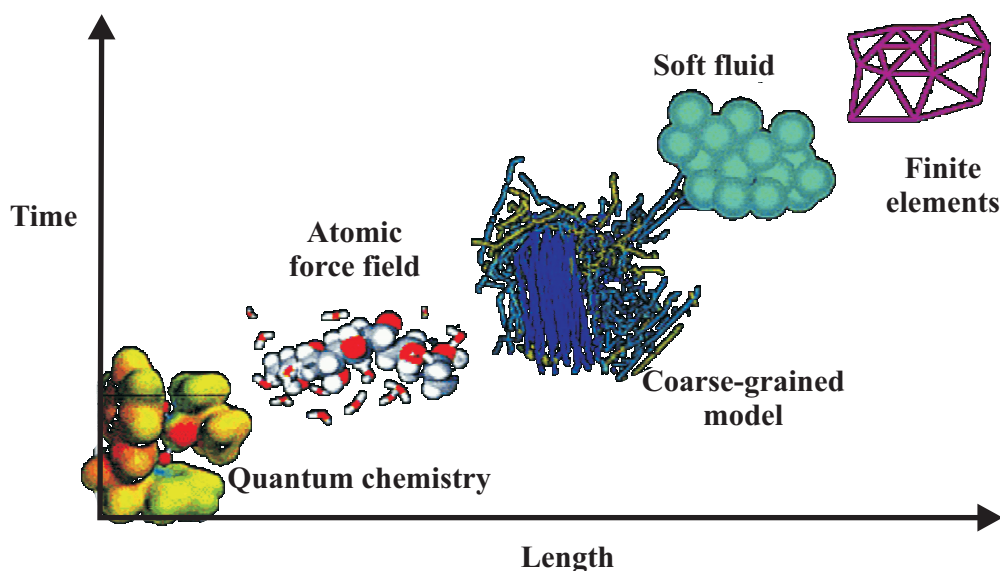


Figure 2.1: *Coarse-graining of block copolymer chain, adapted from [16]*

On a mesoscale the macromolecular nature of polymers suppresses effects related to the atomic details, providing systems where the behavior is more universal and dependent upon far

fewer parameters [17]. A well known example of a coarse grained description of polymers is the lattice based model of a polymer chain in solution, applied by Flory and Huggins [18, 19] in order to determine the entropy of mixing between the components. Here the monomers and the solvent molecules are represented as particles occupying one lattice site each and only the interaction between next nearest neighbors are taken into account by a single Flory-Huggins χ parameter. This model was later extended for the phase separation in the melt of homopolymers by de Gennes [20]. A similar coarse-grained representation of block copolymer chains is applied in particle-based Monte Carlo [21, 22] and molecular dynamics computer simulations.

Alternatively, high-molecular-weight polymers can be accurately modeled as Gaussian chains, where they are represented by smooth space curves with a simple stretching energy to treat their local configurational entropy, and the molecular interaction between A and B segments can be represented by χ . On a coarse-grained level the Gaussian chain can be represented as "spring and beads" model, where springs mimic the stretching behavior of chain segments and different kinds of beads correspond to different components. The degree of coarse-graining determines the calculation costs and is reflected in spatial resolution. The Gaussian chain model is only an example of polymer chain representation. It is well suitable to describe block copolymers characterized by a flexible backbone. Indeed, liquid crystalline polymers molecules are better described by a stiff worm-like chain [23].

2.2 Field theoretic calculation

While the applications of block copolymers often make use of the unique surface or interfacial properties, the understanding of block copolymer thermodynamics is based on the analysis of phase behavior in bulk. Theoretical studies concern with predictions regarding the microdomain geometry, size, and stability as a function of molecular parameters such as volume composition, degree of polymerization, chain architecture, interaction between components, *etc.* Theoretic description of phase separation in block copolymers is typically based on phenomenological energy expansion [24], or on particle-based simulations (e.g. Monte Carlo [21, 22]), or on field theoretic calculations [25]. Here the focus is on the latter method which has been utilized in the present work.

In field theoretic models the variables are the local concentration or density of species in a volume or the size and shape of the elements. It should be noted, that these mesoscopic models neglect atomistic details below 1 nm and time scales related to nanoseconds, nevertheless they lead to significant advances in the understanding of block copolymer structures, dynamics and phase behavior on a mesoscale.

Starting with the works of Edwards [26], field theory models have been extensively used in approximate analytical calculations for a variety of systems such as polymer solutions, polymer melts and blends and copolymers [27, 28].

The theory of phase separation in the bulk of block copolymer melts was originally developed in two limiting regimes (see Fig. 2.2): the *weak segregation limit* (WSL), which is valid near the order-disorder transition (ODT) where the magnitude of the oscillation of the local densities is small, and the *strong segregation limit* (SSL), which is valid in a well-ordered state where the interface between the microdomains is small in comparison to the microdomain size. An excellent detailed review on these two limiting regimes was written by Bates and Fredrickson [29].

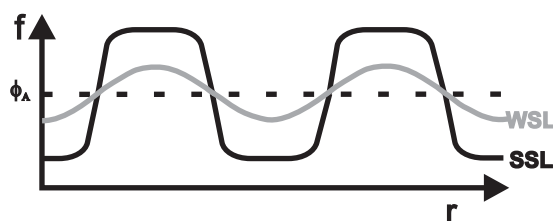


Figure 2.2: *One-dimensional composition profiles characterizing the weak (WSL) and strong (SSL) segregation limits. f refers to the local A-block volume fraction, while ϕ_A shows its macroscopic (mean) value.*

The theory of WSL was originally developed by Leibler [28] and is based on the expansion of the free energy in powers of an order parameter. This theory describes well the transition

from a disordered phase to an ordered phase. Scattering functions in the disordered phase are predicted by the theory, and the spinodal is obtained as the position of points for which the scattering function diverges. Lamellar, hexagonal and cubic phases in a weakly segregated melt of diblock copolymers were predicted by Leibler [28] within a mean field approximation by regarding preassumed periodic structures and looking for minimal free energy. His conclusion was that, at equilibrium, the bulk state of the diblock system is determined by only two relevant parameters: the copolymer chain composition f and the product χN (N is the polymerization index). Fredrickson and Helfand [30] extended the theory of Leibler by taking into account composition fluctuations, which are essential near ODT. De la Cruz and Sanchez [31] applied WSL theory to more complex block copolymer architectures like star and grafted polymers. Mayes and Sanchez [32] calculated the phase diagram for *ABA* triblock copolymers.

In strong segregation limit, the physical principles that govern the microdomain period and the selection of ordered phases have been well-established by the works of Meier [33] and Helfand [27, 34]. The strong segregation theory of Helfand [27, 34] is based on the use of direct space distribution functions which describe the probabilities of finding chain-end segments of different lengths at different positions. These probabilities predict the assumed densities. Deviations from the ideal Gaussian chain conformations are quantitatively taken into account by introduction of a spatially varying mean field. Helfand and Wasserman developed numerical techniques for calculating the phase diagram in strong segregation limit and established regions of stability for spheres [35], cylinders [36] and lamellae [34] phases. Semenov [37] suggested an analytical solution of self consistent theory in the asymptotic limit $\chi N \rightarrow \infty$.

Matsen and coworkers [38, 40, 41, 42, 43, 44, 45, 46] have solved Helfands self consistent field theoretic equations without the limiting narrow interface approximation [34] for the complete spectrum of segregations. For the simplest architecture of linear *AB* diblock copolymers, four morphologies have been determined to be thermodynamically stable in the bulk, depending on χN and the volume fractions of the two blocks: lamellae of alternating *A*-rich and *B*-rich layers, hexagonally packed cylinders of the minority component (*A*) in the matrix of the other component (*B*), *A*-spheres packed on a body-centered cubic lattice in the *B*-matrix, and a bicontinuous gyroid phase [46] (Fig. 2.3).

A promising alternative to spectral SCFT methods, which consider preassumed periodic structures, is the DDFT method, developed by Fraaije and co-workers [47, 48]. Here the minimization of the free energy automatically results from an evolution of the density distribution, driven by diffusional dynamics and gradients of chemical potentials [47]. This dynamic approach allows to study the kinetics of phase separation and phase transitions and the transport mechanisms in block copolymers. It does not require *a priori* knowledge on the structure and therefore can be used to predict new morphologies. In contrast to static approaches which clas-

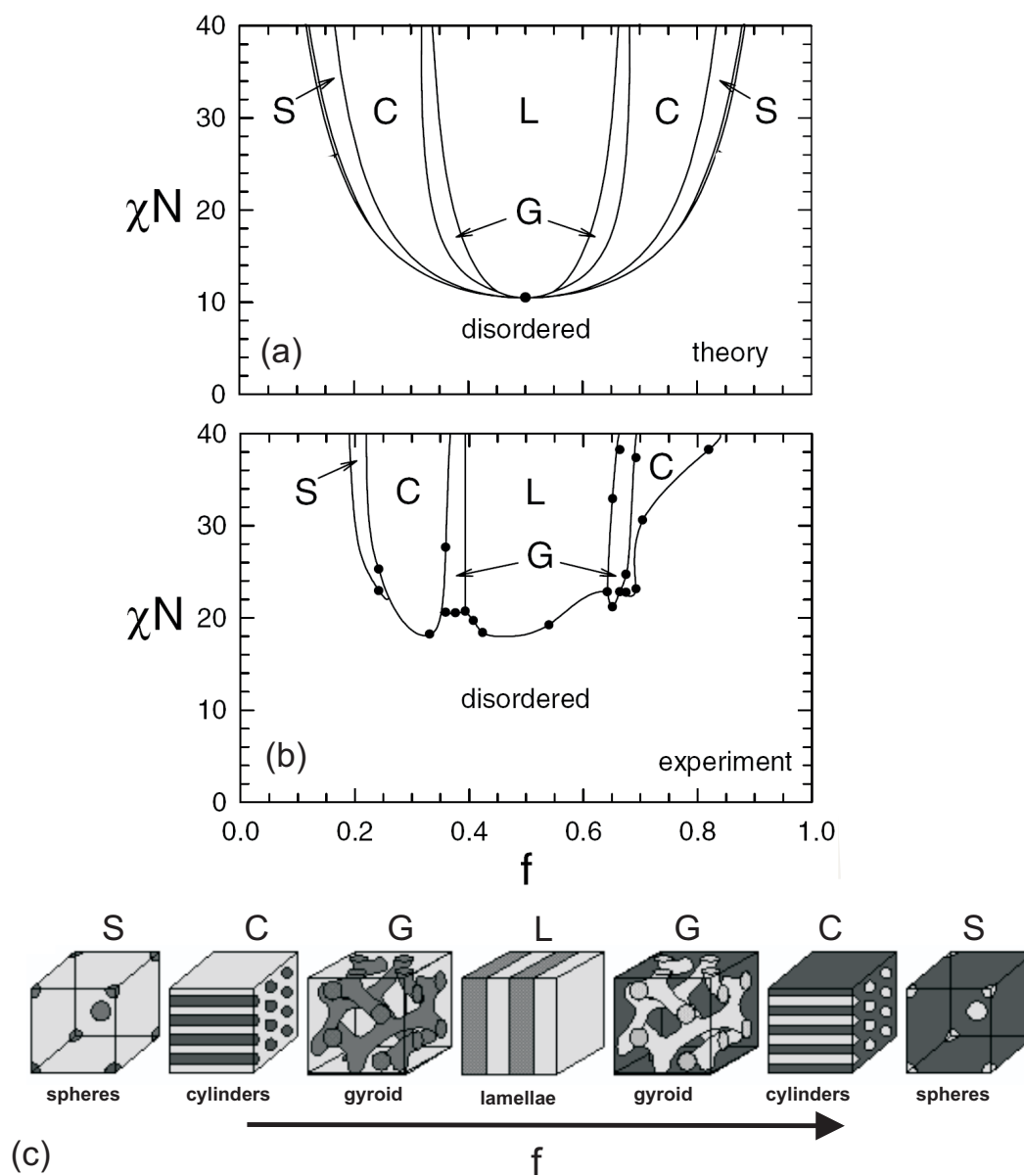


Figure 2.3: Phase diagram of self-assembled structures in AB diblock copolymer, (a) predicted by self-consistent mean field theory [38] and (b) measured experimentally using polystyrene-polyisoprene diblock copolymers [39]. (c) Schematic illustrations of equilibrium morphologies for linear AB diblock copolymer.

sify block copolymer morphologies via equilibrium theories, the dynamic approach recognizes the fact that by their nature block copolymer patterns are not always regular. In experiments, the morphology of a single sample typically includes defects and often consists of coexisting morphologies. In general, real (experimental) systems self-assemble only under the influence of thermal energy (or enhanced mobility of block copolymer). The self-organization process requires material flow and energy exchange, and hence, it can only be characterized via the dynamic properties of the system.

Another advantage of the dynamic approach is that it describes more realistically the preparation and/or processing of block copolymer samples where the typical experimental times are orders of magnitude shorter than thermodynamic relaxation times, and thus non-perfectly ordered structures substantially contribute to the behavior of the final material. Quenching in the absence of a biasing field often results in messy, irregular, nonequilibrium states with "poorly defined morphologies" [49].

Finally, it should be noted, that equilibrium structures computed with DDFT in fact represent solutions of the SCFT equations.

2.3 Thin films of block copolymers

Over the last decades thin block copolymer films have been the subject of intensive research, both experimental [3, 50, 51, 52, 53, 54, 55, 56, 57, 58, 59] and theoretical [24, 60, 61, 62]. Below, the main achievements of the theoretical description of confined block copolymers are summarized.

The effect of a single surface was firstly studied by Semenov [37] in strong segregation limit and by Fredrickson [60] in weak segregation limit. In a weakly segregated lamella-forming diblock copolymer melt Fredrickson found that surface induces sinusoidal composition oscillations which exponentially decay into the bulk. Shull [61] has extended the study of surface effects via a full mean-field treatment. He confined the block copolymer between two surfaces and analyzed thickness instabilities by means of free energy minimums. The same analysis was done by Turner [62] with a phenomenological free energy description. Walton *et al.* [55] extended the study on confined films to the case of lamellae which are oriented perpendicular to the film surfaces. Pickett and Balazs [63] analyzed the stability regions of the perpendicular orientation in lamellar thin films with self consistent field calculations taking additionally into account the preferential attraction of one component to the surface. Together with Fasolka *et al.* [64] they reported an analysis of the morphological behavior of films with thicknesses below the equilibrium period L_0 via self consistent field calculations.

Matsen [65] has first reported self consistent field (SCF) calculations of a phase diagram as a function of thickness for a lamella-forming diblock copolymer. Additionally to the stability analysis for unconfined films, he considered mixed morphologies and undulations in domain shapes.

Most of published research concerns lamella-forming systems, while block copolymers which form hexagonally ordered cylinders are considerably less studied. Here the intrinsic 3D interfacial curvature provides in thin films extra degrees of freedom, and a realistic 3D-space description of microdomain structure is required. By now it is well established that confinements and surface fields effects can cause the microdomains to deviate from the bulk cylindrical structure.

Turner predicted a transition to the non-bulk lamellar morphology in the vicinity of a surface [24], while Suh *et al.* [66] analyzed the stability regions of parallel and perpendicular orientations of cylinders as a function of the film thickness. Both studies use a phenomenological free energy model for the strong segregation limit. The first detailed study by means of SCFT as well as the first phase diagram for asymmetric diblock copolymers in a thin film were reported by Huinink *et al.* [67, 68, 69]. These papers were followed by a series of other publications based on the same method [10, 58, 70, 71, 72] or on Monte-Carlo simulations [73, 74, 75, 76, 77, 78].

2.4 Dynamic density functional theory for thin films of block copolymers: computer simulations

Computer simulations reported here were performed with the parallel MesoDyn code [79], which is based on the (Mean-Field) Dynamic Density Functional Theory (DDFT) originally proposed by Fraaije [47, 48]. In literature the theory is also referred to as Dynamic Self Consistent Field Theory (DSCFT) [25].

Molecular model and the free energy functional

A system of volume V which contains n Gaussian chains of the length $N = N_A + N_B$ is considered. The chemical composition of the polymer molecule is reflected by beads of different types, labeled by the index I . The bead index number is $s = 1, \dots, N$. We assume the volume of different beads to be the same, therefore $f_A = \frac{N_A}{N}$.

The Hamiltonian of one ideal Gaussian chain can be written as:

$$H^G = \frac{3kT}{2a^2} \sum_{s=2}^N (\mathbf{R}_s - \mathbf{R}_{s-1})^2; \quad (2.1)$$

here a is the Gaussian bond length parameter, k is the Boltzmann constant, T is the temperature, \mathbf{R}_s is the position of the s^{th} bead.

In the presence of an additional external field U the partition function for a single chain is:

$$\Phi \equiv \frac{1}{\Lambda^{3N}} \int_{V^N} [e^{-\frac{1}{kT}[H^G + \sum_{s=1}^N U_s(\mathbf{R}_s)]}] \times \prod_{s=1}^N d\mathbf{R}_s. \quad (2.2)$$

Λ^{3N} is the normalization factor [48]. The corresponding single chain distribution is given by the Boltzmann distribution:

$$\psi \equiv \frac{1}{\Phi} e^{-\frac{1}{kT}[H^G + \sum_{s=1}^N U_s(\mathbf{R}_s)]} \quad (2.3)$$

For a system of volume V the transition from the particle based to the field theoretic approach is given by **density functionals**:

$$\rho_I(\mathbf{R}) = \frac{n}{\Lambda^{3N}} \sum_{s=1}^N \delta_{Is}^K \int_{V^N} \delta(\mathbf{R} - \mathbf{R}_s) e^{-\frac{1}{kT}[H^G + \sum_{s=1}^N U_s(\mathbf{R}_s)]} \times \prod_{s=1}^N d\mathbf{R}_s, \quad (2.4)$$

This density functional for the Gaussian chain relates bijectively and in a self-consistent way the density fields ρ_I and the external potentials U_I [48, 80]. There is no known closed analytical expression for the inverse density functional $U_I(\rho)$, but it can be calculated efficiently by numerical procedures [81, 82].

The free energy for such a system can be expressed as [48]:

$$F[\rho] = -kT \ln \Phi^n / n! - \sum_I \int_V U_I(\mathbf{r}) \rho_I(\mathbf{r}) d\mathbf{r} + F^{nid}[\rho] \quad (2.5)$$

The non-ideal part of free energy F^{nid} captures two types of interactions: (1) the hard-core interactions or *incompressibility* of the polymer melt, which are included via the phenomenological Helfand penalty function [27], and (2) the cohesive interaction between the beads. The second one is commonly taken into account in the same way as by the Flory-Huggins lattice theory [19]. The compressibility of the system is included via:

$$F^e[\rho] = \frac{k_H}{2} \int_V \left(\sum_I v_I (\rho_I(\mathbf{r}) - \rho_I^0) \right)^2 d\mathbf{r} \quad (2.6)$$

Here k_H is Helfand coefficient, ρ_I^0 is the average concentration of the component I , and v_I is the bead volume.

For the cohesive interaction between the beads, a Gaussian kernel is used:

$$\varepsilon_{IJ}(\mathbf{r} - \mathbf{r}') \equiv \varepsilon_{IJ}^0 \left(\frac{3}{2\pi a^2} \right)^{3/2} e^{-\frac{3(\mathbf{r} - \mathbf{r}')^2}{2a^2}}.$$

The strength of the interaction, ε_{IJ}^0 (in kJ/mol) is directly related to the Flory-Huggins parameter ($\chi_{IJ} = 1000\varepsilon_{IJ}^0 / N_a kT$). The input to the free energy functional is:

$$F^{coh}[\rho] = \frac{1}{2} \sum_{I,J} \int_V \int_V \varepsilon_{IJ}(\mathbf{r} - \mathbf{r}') \rho_I(\mathbf{r}) \rho_J(\mathbf{r}') d\mathbf{r} d\mathbf{r}' \quad (2.7)$$

Dynamic equations

The thermodynamic forces, that drive the phase separation and the structure formation, are local gradients in the intrinsic chemical potential. The chemical potentials are derived from the functional differentiation of the free energy and are a function of the external potentials and the density fields:

$$\mu_I(\mathbf{r}) = \frac{\delta F}{\delta \rho_I(\mathbf{r})} \quad (2.8)$$

In the simulational code, applied in this thesis, the time evolution of the density field $\rho_I(\mathbf{r})$ is described by a Langevin equation for diffusion with a constant mobility (M_I) of beads [83]:

$$\frac{\partial \rho_I}{\partial t} = M_I \nabla \cdot \rho_I \nabla \mu_I + \eta_I, \quad (2.9)$$

η_I is a thermal noise, distributed according to the fluctuation-dissipation theorem [84].

Surface fields and confinement effects

The effect of a substrate in thin films is modeled via confining the block copolymer in a slit. The surfaces of the slit are regarded as hard objects and mass transport through these objects has to be forbidden. Therefore, rigid-wall boundary conditions constrain a thin film by keeping the flux perpendicular to the substrate equal zero [67, 85]: $\nabla\mu_I \times \vec{n} = 0$, where \vec{n} is the normal of the slit surface. The solid surfaces are treated like hard walls also called "mask fields". The interactions with the substrate is taken into account in the same way as the interaction between the beads (Fig. 3.1). The surface field induced term in F^{nid} is:

$$F^{surf}[\rho] = \frac{1}{2} \sum_I \int_V \int_V \epsilon_{IM}(|\mathbf{r} - \mathbf{r}'|) \rho_I(\mathbf{r}) \rho_M(\mathbf{r}') d\mathbf{r} d\mathbf{r}' \quad (2.10)$$

where $\rho_M(\mathbf{r}')$ describes the position of the mask ($\rho_M(\mathbf{r}')$ is equal 1 if \mathbf{r}' belongs to the mask, or 0 if \mathbf{r}' belongs to the polymer film).

Numerics

The Gaussian chain density functional (Eq. 2.4), the equation for intrinsic chemical potentials (Eq. 2.8), the Langevin equation for diffusion (Eq. 2.9) and the expression for the thermal noise form together a closed set. This set is integrated on a 27-stencil cubic mesh by a Crank-Nicolson scheme [81]. Zero external potential fields and homogeneous density distributions are used as starting configurations for the integration.

3 Overview of thesis

3.1 Results

In this thesis modeling results on structure formation at multiple time- and length- scales in thin films of asymmetric cylinder-forming block copolymers are presented and discussed. The complexity of the simulated system was stepwise increased to model the behavior of supported thin films of polystyrene-polybutadiene di- and tri- block copolymers, which form polystyrene cylinders in a polybutadiene matrix in bulk [11, 15, 86]. The thesis includes five publications. **Chapters 4** and **5** report on the equilibrium structures in thin films of compositionally asymmetric block copolymers. **Chapters 6** and **7** consider structural defects and their dynamics. Finally, the dynamics of surface relief structures is reported in **Chapter 8**. Each chapter includes a detailed comparison of simulations with experimental observations in order to ascertain the relevant parameters, which determine the morphology and the dynamics in thin copolymer films, and to suggest specific mechanisms, which govern the structural ordering.

Phase behavior in thin films of cylinder-forming block copolymers

Since the seminal work of Anastasiadis et al. [51], the behavior of lamella-forming block copolymers in thin films has been studied in detail and two major effects have been identified. The preferential attraction of one type of block to the surface (the surface field) causes the lamellae to align parallel to the interfaces. As a result, the film forms islands or holes where the film thickness is a (half) integer multiple of the lamella spacing in the bulk. In cases where the film thickness is not compatible with the natural bulk domain spacing or when the film/air and the film/substrate interface is not selective, lamellae can orient perpendicular to the interfaces [55, 57, 64, 87].

The behavior of cylinder-forming systems is more complex. Here, besides cylinders oriented parallel and perpendicular to the surface, a variety of deviations from the bulk structure have been observed: disordered phase [88], a wetting layer [89], spherical microdomains [90], a perforated lamella [90], as well as more complicated hybrid structures such as cylinders with

necks [91], a perforated lamella with spheres [92, 93], and an inverted phase. [94] Although various models have been developed to describe this behavior [24, 68, 73, 95] (for summary, see Ref. [73]), modeling and experimental results agree qualitatively only in parts. The goal of the research presented in chapters 4 and 5, is to clarify which of the reported phenomena are specific to the particular system and/or route of film preparation and which are general behavior, and to establish general understanding of the underlying fundamentals.

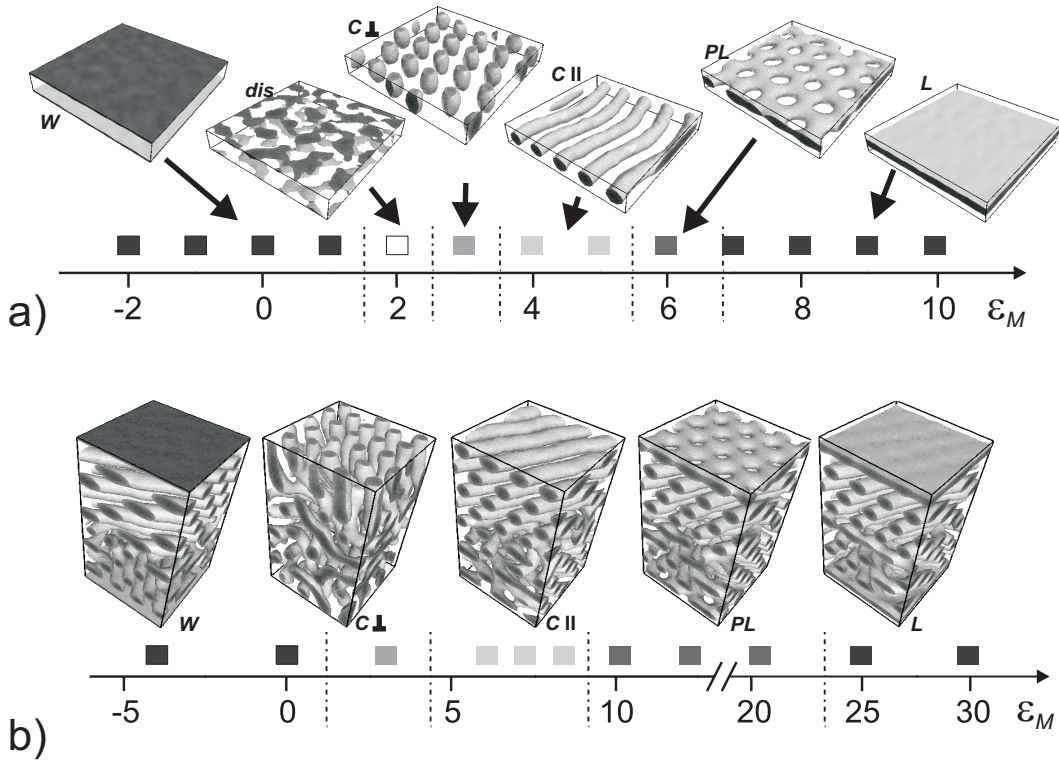


Figure 3.1: *Effect of the strength of the surface field ϵ_M on microdomain structures and surface reconstructions. Gray boxes indicate ϵ_M values where simulations have been done. Isodensity surfaces ($\rho_A = 0.45$) are shown for typical structures. (a) One microdomain thick films ($H = 6$). (b) Rather thick films (9 microdomains, $H = 54$).*

Chapter 4 reports results of numerical calculations of phase behavior in a thin films of cylinder-forming triblock copolymers in a large range of parameter (the bead-bead interaction ϵ_{AB} , the layer thickness H and the interaction with surfaces ϵ_M are varied). The effect of bead-bead interaction on a bulk morphology for a model $A_3B_{12}A_3$ Gaussian chain with a volume fraction of A component $f_A = 0.33$ is investigated in order to determine the parameter space of the cylinder morphology. Next, the effect of confinement on the cylinder phase is studied. For selected ϵ_{AB} values the thin film morphology as a function of the film thickness (H) and an effective surface interaction ($\epsilon_M = \epsilon_{AM} - \epsilon_{BM}$) is investigated. The important feature of the thin

film phase behavior is the existence of non cylindrical morphologies: a wetting layer, a perforated lamella, a lamella (see Fig. 3.1). These deviations are present in thin films (one domain spacing), as well as at surface of thick films (9 domain spacings), Fig. 3.1, and are identified as *surface reconstruction*. The same morphologies were reported also experimentally (see citations above). The results indicate that these morphologies are induced by surface fields, which extend into the bulk with a decay length of about one microdomain spacing. Furthermore, surface fields are additive, and for very thin films the effects of both surfaces combine.

Together with what is known for lamella-forming systems the calculated results give evidence of a general mechanism governing the phase behavior in thin block copolymer films: The interplay between the strength of the surface field and the deformability of the bulk structure determines how the system rearranges in the vicinity of the surface. This causes either an orientation of the bulk structure (e.g. cylinders oriented parallel or perpendicular to the substrate) or the formation of surface reconstructions (wetting layer, perforated lamella and lamella). The stability regions of the different phases are modulated by the film thickness via interference of surface fields and confinement effects.

Finally, via comparison of experimental [86] and simulational phase diagrams, the experimental control parameter (the polymer concentration in the swollen block copolymer film) is related to the interaction parameter of polymer beads with the surface used in the calculations.

Chapter 5 is published as a short communication [58]. It presents a comparative study of the phase behavior of cylinder-forming *ABA* block copolymers in thin films. The experiments are done on SBS triblock copolymers thin films, equilibrated by annealing in chloroform vapor. The morphology is measured by scanning force microscopy (SFM). The experimental system is parametrized based on the results of chapter 4. The effect of the solvent is modeled by introducing an effective surface interaction parameter proportional to the polymer concentration. The experimentally determined χN parameter of ≈ 35 corresponds to $\epsilon_{AB} = 6,5$ in simulations. The simulation of an $A_3B_{12}A_3$ block copolymer film, done in a wedge-shaped geometry (where the film thickness varies), exhibits exactly the same sequence of phases as the SFM measurements on SBS film with increasing film thickness. The good match corroborates the assignment of experimentally observed 2D surface patterns to distinct phases. In particular, the calculations allow to distinguish between perforated lamella phase (black dot pattern) and perpendicular cylinder phase (white dot pattern), Fig. 3.2. The experiment and the simulation reveal variety of phases in a single system under identical equilibration conditions. This finding indicates that, together with effective surface interaction, the film thickness is an important control parameter.

The experimental phase diagram (surface structures as a function of solvent content and film thickness) is compared with the simulated phase diagram (surface structures as a function of surface field and film thickness). Although DDFT simulations simplify the effect of solvent

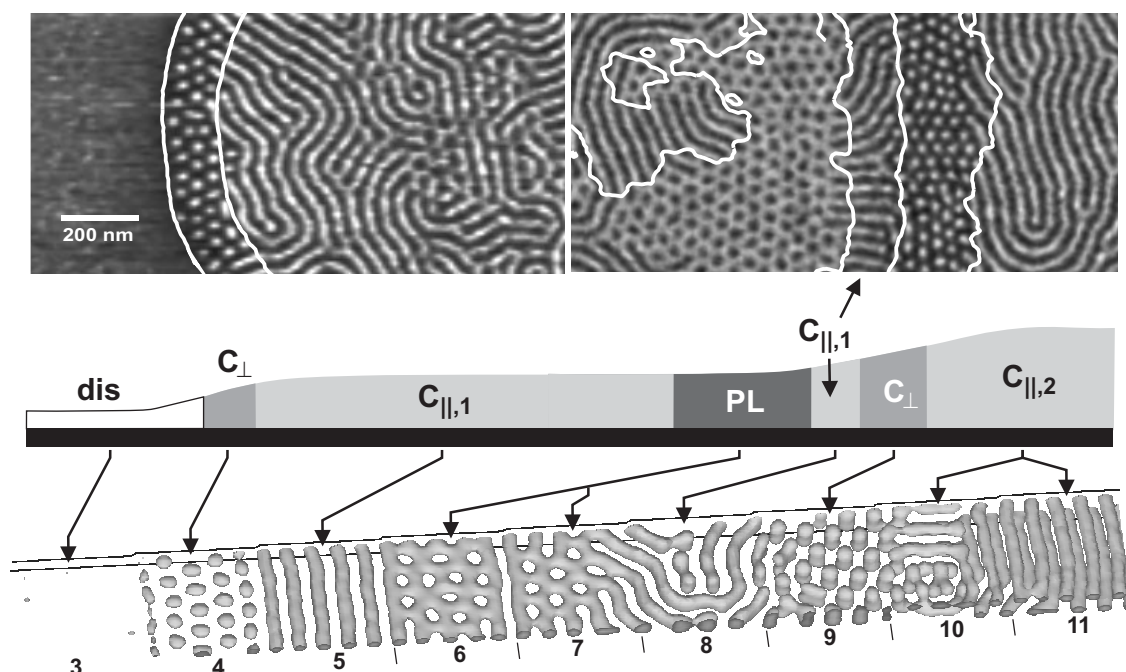


Figure 3.2: *Top: TappingMode SFM phase images of thin polystyrene-block-polybutadiene-block-polystyrene films on silicon substrates after annealing in chloroform vapor. Bright (dark) corresponds to PS (PB) microdomains below a top PB layer. Schematic height profile of the phase images shown in the middle. Bottom: Simulation of an $A_3B_{12}A_3$ block copolymer film in one large simulation box with from left to right increasing film thickness $H(x)$, $\epsilon_{AB} = 6.5$, and $\epsilon_M = 6.0$.*

annealing, they predict the experimental phase diagram with intriguing complexity: the comparison of experimental results and simulations allows to distinguish the effects of the two constraints being simultaneously present in thin films, the surface field and the film thickness. Similar phase behavior reveals the general character of the response of the cylinder phase to the above constraints.

Specific features of defect structure and dynamics in cylinder phase of block copolymers

The application of block copolymers in conventional lithography [7] requires large area of defectless nanopatterns. Various strategies such as chemical modification of the substrate [96, 97, 98] or external fields [99] are used to align and order the microdomains over macroscopically large areas. In order to control the process of ordering one needs to understand the dynamics in thin films, particularly the dynamics of defects and the mechanisms of defect annihilation. This



Figure 3.3: *Transitional perforated lamella Pl phase as captured by simulations*

makes the dynamics of nanostructured fluids in thin films to an issue of recent interest [10, 100]. **Chapters 6** and **7** consider the structure and the dynamics of typical defects in the cylinder phase of block copolymers.

Chapter 6 presents a detailed experimental and theoretical comparative study of defect features which are specific for the cylindrical structures in block copolymer films. Additionally to classical topological defect configurations, such as edge dislocations and disclinations well known for a broad range of condensed matter, including liquid crystals and block copolymers [98, 101, 102, 103, 104, 105], representative *modified*, *specific* and *grain boundary* defects have been identified.

Modified classical defects result from incorporation of elements of non-bulk structures into a classical defect. This class of defects reflects the rich phase behavior of cylinder-forming block copolymers in thin films [58].

Specific defects, such as bridge-like connections between neighboring cylinders, do not influence the orientational order parameter, but enhance the connectivity of the minority component in thin films. These specific defects stress the structural similarities between cylinder patterns and other types of soft structured matter such as lyotropic liquid crystals and biological membranes, where analogous bridging connections and their important transport function have been reported [106].

As an example of typical grain boundary defect, *T-junctions* and their dynamics are analyzed. Good agreement between the dynamic experiments and simulations on the details of the lateral propagation of a complex 3T-junction defect suggests diffusion-driven lateral transport and correlated defect motion due to the interconnectivity of the polymer chains.

The simulation results, which access the 3D structure of thin films, shows that purely topological arguments and 2D representation are not sufficient to elucidate the stability and mobility of defects in cylinder morphology. Characteristic for all types of defects in cylinder-forming thin films is the connectivity of the minority (A or polystyrene) phase. Configurations with an open cylinder end are typically short-lived elementary steps of defect reconstruction, and are, in general, less stable than defects with closed cylinder end (branched cylinders). The results indicate that the material transport in block copolymers occurs preferentially along rather than across the A-B interface.

Chapter 7 reports on temporal phase transitions as a specific defect annihilation pathway. Both, time resolved experiments and DDFT simulations reveal temporal changes of the local morphology which accompany the reorientation of cylindrical grains (see Fig. 3.3). The formation of local transient phases such as spherical domains, perforated lamella, and lamellar patches is a short-term pathway facilitating the long-term behavior. The observed structural evolution is closely related to the equilibrium phase behavior in cylinder-forming films, which has been studied in detail in chapters 4 and 5. The temporal non bulk structures have also been observed in phase diagrams (chapter 5) under variation of the film thickness or surface fields. These results demonstrate that microdomain dynamics is closely related to the intrinsic rich morphological behavior of cylinder phase under confinement.

Time evolution of surface relief structures in thin block copolymer films

Chapter 8 reports on the dynamics of the early stage of terrace formation in thin supported films of cylinder-forming triblock copolymers, studied both theoretically using DDFT and experimentally by *in-situ* SFM.

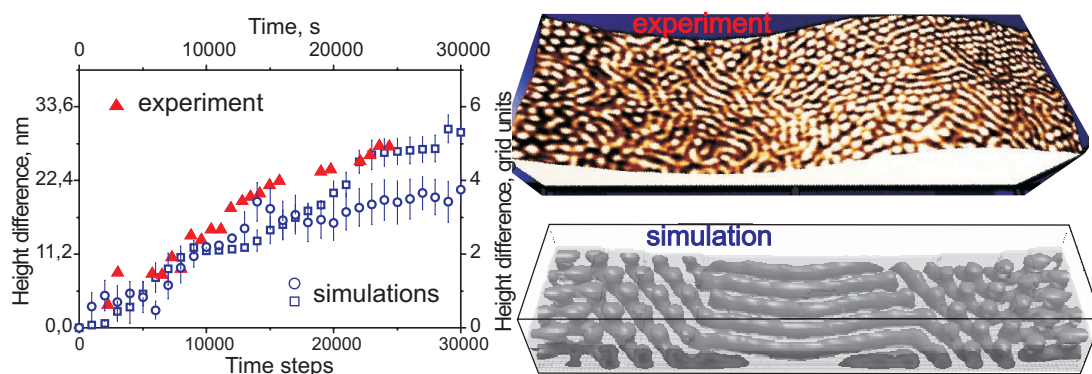


Figure 3.4: *Left: Step heights in the experiment and in the simulations are plotted as a function of time. Right: Snapshots of structure as revealed by SFM measurements and simulations after 8 hours of annealing (or 25 000 simulation steps)*

A universal experimentally observed phenomenon in thin films of block copolymers is the formation of terraces with the film thickness of a (half) integer multiple of the natural microdomain spacing [3, 50, 51, 52, 53, 107]. Experimentally, nucleation and subsequent growth of surface relief structures, are typically followed by time-resolved optical micrographs or SFM, and are studied as a function of surface fields [108, 109, 110], molecular architecture [111], film thickness [87, 112], and annealing conditions [111, 112, 113]. The main accent in the above mentioned experimental works as well as in a few theoretical works [100, 109, 114] on terrace formation dynamics is done on late stages, where the step height between the terraces has

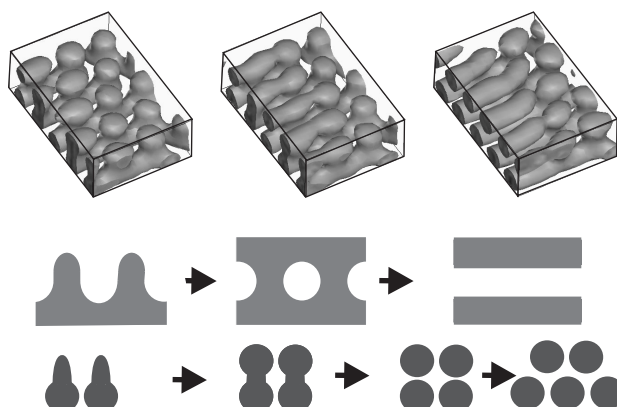


Figure 3.5: *Simulation snapshots and schematic representation of the $C_{\parallel}C_{\perp}$ - to - $C_{\parallel,2}$ transition*

reached the equilibrium value and remains constant. The late stage can be characterized by a local rearrangement in microdomain structure (ordering processes) [10] and by coalescence of terraces [114]. However, the largest part of the material transport within thin film takes place on early stages of annealing. Therefore, a detailed study of early stages gives new insights into transport mechanisms in block copolymers.

In experiment, an initially flat SBS film of incommensurable thickness is continuously imaged by SFM, and the evolution of vertical orientation of cylinders into parallel one, as well as the respective development of thickness gradient (terrace formation) is captured in detail.

In simulations the free film surface is created as an interface between the block copolymer and a third component which does not mix with the block copolymer and acts as an "air" phase [115, 116]. This interface can spontaneously change its shape during a simulation run. The focus of this study is on the early stage of terrace formation, which is characterized by the development of the step height up to 80% of its equilibrium value and by an associated reorientation of cylindrical domains. Simulations reveal that the formation of the microstructure starts at the substrate. Subsequently, the initially flat film develops terraces.

Both, the experiments and the simulations show that the change of the local height is strongly connected to the changes in the local microstructure. They show excellent agreement in details of structural phase transitions and in the dynamics of step development (see Fig. 3.4). The detailed pathways of the transitions, as revealed by simulations, suggest a diffusion of block copolymer chains along the microstructure interfaces and indicate an important role of the $C_{\parallel}C_{\perp}$ (neck) structure as material-transport-channel between neighboring terraces in thin cylinder-forming films, see Fig. 3.5. The proposed method gives direct access to the kinetics of phase transitions in real space and real time, and so can serve as an alternative (or at least complement) to dynamic studies in bulk, where only statistical mean values are available from scattering data.

3.2 Individual contribution of authors

Chapter 4 is published in J. Chem. Phys. 120, 1117 (2004) under the title **Phase behavior in thin films of cylinder-forming ABA block copolymers: Mesoscale modeling** by Horvat A., Lyakhova K.S., Sevink G.J.A., Zvelindovsky A.V., Magerle R.

I established the mesoscale modeling as a complement method to the experimental investigations of the thin film behavior. I have planned and performed all simulations presented in this work. I have mapped the experiments, performed in the same group, [86] to the theoretical phase diagram, which cover a much larger parameter space than available in the experiments. Robert Magerle contributed eminently to the scientific discussion. Katya Lyakhova has introduced the simulational code to me. Agur Sevink and Andrej Zvelindovski have supported the simulational code and were involved in the discussion. The publication was written by me.

Chapter 5 is published in Phys. Rev. Lett. 89, 035501 (2002) under the title **Phase behavior in thin films of cylinder-forming block copolymers** by Knoll A., Horvat A., Lyakhova K.S., Krausch G., Sevink G.J.A., Zvelindovsky A.V., Magerle R.

I have parametrized the simulations in respect to the experiment. I have performed all simulations and have analyzed and interpreted all theoretical results. All SFM measurements were done by Armin Knoll. Katya Lyakhova, Agur Sevink and Andrej Zvelindovski were involved in the discussion of the simulational data. Georg Krausch and Robert Magerle contributed essentially to the scientific discussion. The paper consists of two equivalent components: experimental and simulational phase diagrams, and their comparison. The contribution of experiment and of the simulation is of the same impact, but the experiment was carried out first, and therefore Armin Knoll is firstly mentioned in the author register. Both parts (simulations and experiments) presented in this Letter gave rise of two separate publications: on experimental details by Armin Knoll (see Ref. [86]) and on simulations by me (Chapter 2 or Ref. [70]). I have written this article together with Armin Knoll and Robert Magerle.

Chapter 6 is published in ACS Nano 2, 1143-1452 (2008) under the title **Specific features of defect structure and dynamics in cylinder phase of block copolymers** by Horvat A., Sevink G.J.A., Zvelindovsky A.V., Krekhov A., and Tsarkova L.

I have performed all simulations and have analyzed and evaluated all simulational results. The SFM measurements were done by Larisa Tsarkova. Agur Sevink and Andrej Zvelindovski have supported the simulational code. Alexei Krekhov has contributed to the discussion of similarities between block copolymers and liquid crystals. The manuscript was written together with Larisa Tsarkova.

Chapter 7 is published as ACS preprint (2006) under the title: "**Structural Ordering in Thin Films of Cylinder Forming Block Copolymers**" by Tsarkova L., Horvat A., Krausch G., Magerle R.

I have performed the simulations and have analyzed the simulational results. The SFM measurements were done by Larisa Tsarkova. The results were discussed with Georg Krausch and Robert Magerle. The contribution of experiment and of simulation are of the same impact. The results were presented on ACS conference by Larisa Tsarkova, and therefore she is firstly mentioned in the author register. This article was written together with Larisa Tsarkova.

Chapter 8 is published in *Macromolecules* 40, 6930-6939 (2007) under the title "**Time Evolution of Surface Relief Structure in Thin Films of Block Copolymers**" by Horvat A., Knoll A., Krausch G., Tsarkova L., Lyakhova K.S., Sevink G.J.A., Zvelindovsky A.V., Magerle R.

I have planned and performed all simulations to model terrace formation in thin films of block copolymer. The SFM measurements for comparison were supported by Armin Knoll. I have evaluated, analyzed and compared all results. I have discussed the comparison of simulation results with the experiment with Georg Krausch, Larisa Tsarkova and Robert Magerle. I have also profited from discussions with Agur Sevink, who has modified the simulational code to enable the simulations of terrace formation. Katya Lyakhova and Andrej Zvelindovski were involved in discussion. The publication was written by me.

Bibliography

- [1] P. Spontak, R. J. Alexandridis, *Current Opinion in Colloid & Interface Science*, 1999, **4**, 140–146.
- [2] J. W. Hamley, *The Physics of Block Copolymers*, Oxford University Press, Oxford, 1998.
- [3] M. J. Fasolka and A. M. Mayes, *Annu. Rev. Mater. Res.*, 2001, **31**, 323–355.
- [4] I. W. Hamley, *Nanotechnology*, 2003, **14**(10), R39–R54.
- [5] C. Park, J. Yoon, and E. L. Thomas, *Polymer*, 2003, **44**, 6725–6760.
- [6] S. Granick, S. K. Kumar, M. Amis, E. J. and Antonietti, A. C. Balazs, C. A. K., G. S. Grest, C. Hawker, P. Janmey, E. J. Kramer, R. Nuzzo, T. P. Russell, and C. Safinya, *Journal of Polymer Science: Part B: Polymer Physics*, 2003, **41**, 2755–2793.
- [7] M. P. Stoykovich and P. F. Nealey, *Materials Today*, 2006, **9**(9), 20–29.
- [8] S. Krishnamoorthy, C. Hinderling, and H. Heinzelmann, *Materials Today*, 2006, **9**(9), 40.
- [9] J. Y. Cheng, C. A. Ross, H. I. Smith, and E. L. Thomas, *Adv. Mater.*, 2006, **18**, 402505–2521.
- [10] A. Knoll, K. S. Lyakhova, A. Horvat, G. Krausch, G. J. A. Sevink, A. V. Zvelindovsky, and R. Magerle, *Nature Materials*, 2004, **3**, 886–891.
- [11] L. Tsarkova, A. Knoll, G. Krausch, and R. Magerle, *Macromolecules*, 2006, **39**(10), 3608–3615.
- [12] L. Tsarkova, A. Horvat, G. Krausch, A. V. Zvelindovsky, G. J. A. Sevink, and R. Magerle, *Langmuir*, 2006, **22**(19), 8089–8095.
- [13] N. Rehse, A. Knoll, M. Konrad, R. Magerle, and G. Krausch, *Phys. Rev. Lett.*, 2001, **87**(3), 035505–4.

- [14] A. Sperschneider, F. Schacher, M. Gawenda, L. Tsarkova, A. H. E. Mueller, M. Ulbricht, G. Krausch, and J. Koehler, *SMALL*, 2007, **3**(6), 1056–1063.
- [15] A. Knoll *Equilibrium and Dynamic Phase Behavior in Thin Films of Cylinder-Forming Block Copolymers* Ph.d. thesis, Universitaet Bayreuth, 2003.
- [16] F. Mueller-Plathe, *ChemPhysChem*, 2002, **3**, 754–769.
- [17] M. W. Matsen, *J. Phys.: Condens. Matter*, 2002, **14**, R21–R47.
- [18] P. J. Flory, *J. Chem. Phys.*, 1942, **10**, 51–62.
- [19] P. J. Flory, *Principles of Polymer Chemistry*, Cornell University Press, Cornell, 1978.
- [20] P. G. de Gennes, *J. Chem. Phys.*, 1980, **72**, 4756.
- [21] M. Binder, K. Muller, *Current Opinion in Colloid & Interface Science*, 2000, **5**, 315–323.
- [22] Q. Wang in *Nanostructured Soft Matter: Experiment, Theory, Simulation and Perspectives*, ed. Zvelindovsky; Springer Verlag, Heidelberg, 2007.
- [23] M. Hamm, G. Goldbeck-Wood, A. V. Zvelindovsky, G. J. A. Sevink, and J. G. E. M. Fraaije, *Macromolecules*, 2001, **34**(23), 8378–8379.
- [24] M. S. Turner, M. Rubinstein, and C. M. Marques, *Macromolecules*, 1994, **27**, 4986–4992.
- [25] G. H. Fredrickson, V. Ganesan, and F. Drolet, *Macromolecules*, 2002, **35**(1), 16–39.
- [26] S. F. Edwards, *Proc.Phys.Soc.*, 1965, **85**, 613.
- [27] E. Helfand, *Macromolecules*, 1975, **8**(4), 552–556.
- [28] L. Leibler, *Macromolecules*, 1980, **13**(6), 1602–1617.
- [29] F. S. Bates and G. H. Fredrickson, *Annual Review of Physical Chemistry*, 1990, **41**, 525–557.
- [30] G. H. Fredrickson and E. Helfand, *J. Chem. Phys.*, 1987, **87**, 697.
- [31] M. O. de la Cruz and I. C. Sanchez, *Macromolecules*, 1986, **19**, 2501–2508.
- [32] A. M. Mayes and M. O. de la Cruz, *J. Chem. Phys.*, 1989, **91**(11), 7228.
- [33] D. J. Meier, *J. Polymer Sci.: Part C*, 1969, **26**, 81–98.

- [34] E. Helfand and Z. R. Wasserman, *Macromolecules*, 1976, **9**(6), 879–888.
- [35] E. Helfand and Z. R. Wasserman, *Macromolecules*, 1978, **11**(5), 960–966.
- [36] E. Helfand and Z. R. Wasserman, *Macromolecules*, 1980, **13**(4), 994–998.
- [37] A. N. Semenov, *Sov. Phys. JETP*, 1985, **61**, 733.
- [38] M. W. Matsen and F. S. Bates, *Macromolecules*, 1996, **29**(4), 1091–1098.
- [39] F. S. Bates, M. F. Schulz, A. K. Khandpur, S. Frster, J. H. Rosedale, K. Almdal, and K. Mortensen, *Faraday Discussion*, 1994, **98**, 7–18.
- [40] M. W. Matsen and M. Schick, *Phys. Rev. Lett.*, 1994, **72**(16), 2660(4).
- [41] M. W. Matsen and M. Schick, *Macromolecules*, 1994, **27**(14), 4014–4015.
- [42] M. W. Matsen and M. Schick, *Macromolecules*, 1994, **27**(23), 6761–6767.
- [43] M. W. Matsen and M. Schick, *Macromolecules*, 1994, **27**(24), 7157–7163.
- [44] M. W. Matsen and M. Schick, *Current Opinion in Colloid & Interface Science*, 1996, **1**(3), 329–336.
- [45] M. W. Matsen and F. S. Bates, *Macromolecules*, 1996, **29**(23), 7641–7644.
- [46] M. W. Matsen and F. S. Bates, *J. Chem. Phys.*, 1997, **106**, 2436.
- [47] J. G. E. M. Fraaije, *J. Chem. Phys.*, 1993, **99**(11), 9202–9212.
- [48] J. G. E. M. Fraaije, B. A. C. vanVlimmeren, N. M. Maurits, M. Postma, O. A. Evers, C. Hoffmann, P. Altevogt, and G. GoldbeckWood, *J. Chem. Phys.*, 1997, **106**(10), 4260–4269.
- [49] F. S. Bates, J. H. Rosedale, and G. H. Fredrickson, *J. Chem. Phys.*, 1990, **92**(10), 6255–6270.
- [50] L. Tsarkova in *Nanostructured Soft Matter: Experiment, Theory, Simulation and Perspectives*, ed. Zvelindovsky; Springer Verlag, Heidelberg, 2007; pp. 231–268.
- [51] S. H. Anastasiadis, T. P. Russell, S. K. Satija, and C. F. Majkrzak, *Phys. Rev. Lett.*, 1989, **62**(16), 1852–1855.
- [52] T. P. Russell, G. Coulon, V. R. Deline, and D. C. Miller, *Macromolecules*, 1989, **22**(12), 4600–4606.

- [53] G. Coulon, T. P. Russell, V. R. Deline, and P. F. Green, *Macromolecules*, 1989, **22**, 2581–2589.
- [54] B. Collin, D. Chatenay, G. Coulon, D. Ausserre, and Y. Gallot, *Macromolecules*, 1992, **25**(5), 1621–1622.
- [55] D. G. Walton, G. J. Kellogg, A. M. Mayes, P. Lambooy, and T. P. Russell, *Macromolecules*, 1994, **27**(21), 6225.
- [56] G. Krausch, *Materials Science and Engineering*, 1995, **R14**(1), 1–94.
- [57] G. J. Kellogg, D. G. Walton, A. M. Mayes, P. Lambooy, T. P. Russell, P. D. Gallagher, and S. K. Satija, *Phys. Rev. Lett.*, 1996, **76**(14), 2503–2506.
- [58] A. Knoll, A. Horvat, K. S. Lyakhova, G. Krausch, G. J. A. Sevink, A. V. Zvelindovsky, and R. Magerle, *Physical Review Letters*, 2002, **89**(3), 035501/1–4.
- [59] G. Krausch and M. R., *Advanced Materials*, 2002, **14**(21), 1579–1583.
- [60] G. H. Fredrickson, *Macromolecules*, 1987, **20**, 2535–2542.
- [61] K. R. Shull, *Macromolecules*, 1992, **25**, 2122–2133.
- [62] M. S. Turner, *Phys. Rev. Lett.*, 1992, **69**(12), 1788(4).
- [63] G. T. Pickett and A. C. Balazs, *Macromolecules*, 1997, **30**(10), 3097–3103.
- [64] M. J. Fasolka, P. Banerjee, A. M. Mayes, G. Pickett, and A. C. Balazs, *Macromolecules*, 2000, **33**(15), 5702–5712.
- [65] M. W. Matsen, *J. Chem. Phys.*, 1997, **106**(18), 7781–7791.
- [66] K. Y. Suh, Y. S. Kim, and H. H. Lee, *J. Chem. Phys.*, 1998, **108**(3), 1253–1256.
- [67] H. P. Huinink, J. C. M. Brokken-Zijp, M. A. van Dijk, and G. J. A. Sevink, *J. Chem. Phys.*, 2000, **112**(5), 2452–2462.
- [68] H. P. Huinink, M. A. van Dijk, J. C. M. Brokken-Zijp, and G. J. A. Sevink, *Macromolecules*, 2001, **34**(15), 5325–5330.
- [69] G. J. A. Sevink, J. G. E. M. Fraaije, and H. P. Huinink, *Macromolecules*, 2002, **35**(5), 1848–1859.
- [70] A. Horvat, K. Lyakhova, G. J. A. Sevink, A. Zvelindovsky, and R. Magerle, *J. Chem. Phys.*, 2004, **120**(2), 1117–1126.

- [71] K. S. Lyakhova, G. J. A. Sevink, A. V. Zvelindovsky, A. Horvat, and R. Magerle, *J. Chem. Phys.*, 2004, **120**(2), 1127–1137.
- [72] S. Ludwigs, G. Krausch, R. Magerle, A. V. Zvelindovsky, and G. J. A. Sevink, *Macromolecules*, 2005, **38**(5), 1859–1867.
- [73] Q. Wang, P. F. Nealey, and J. J. de Pablo, *Macromolecules*, 2001, **34**(10), 3458–3470.
- [74] Q. Wang, P. F. Nealey, and J. J. de Pablo, *Macromolecules*, 2003, **36**(5), 1731–1740.
- [75] J. Feng, H. Liu, and Y. Hu, *Macromol. Theory Simul.*, 2002, **11**, 556–565.
- [76] J. Feng and E. Ruckenstein, *Macromol. Theory Simul.*, 2002, **11**, 630–639.
- [77] J. Feng and E. Ruckenstein, *Polymer*, 2002, **43**, 5775–5790.
- [78] G. Szamel and M. Mueller, *J. Chem. Phys.*, 2003, **118**(2), 905–913.
- [79] <http://accelrys.com/products/materials-studio/modules/mesodyn.html>.
- [80] N. D. Mermin, *Physical Review*, 1965, **137**(5A), 1441.
- [81] N. M. Maurits, P. Altevogt, O. A. Evers, and J. G. E. M. Fraaije, *Comp. Polymer Sci.*, 1996, **6**(1).
- [82] N. M. Maurits, B. A. C. van Vlimmeren, and J. G. E. M. Fraaije, *Phys. Rev. E*, 1997, **56**, 816–825.
- [83] N. M. Maurits and J. G. E. M. Fraaije, *J. Chem. Phys.*, 1997, **107**(15), 5879–5889.
- [84] B. A. C. van Vlimmeren and J. G. E. M. Fraaije, *Comput. Phys. Commun.*, 1996, **99**, 21–28.
- [85] G. J. A. Sevink, A. V. Zvelindovsky, B. A. C. van Vlimmeren, N. M. Maurits, and J. G. E. M. Fraaije, *J. Chem. Phys.*, 1999, **110**(4), 2250–2256.
- [86] A. Knoll, R. Magerle, and G. Krausch, *J. Chem. Phys.*, 2004, **120**(2), 1105–1116.
- [87] B. L. Carvalho and E. L. Thomas, *Physical Review Letters*, 1994, **73**(24), 3321–3324.
- [88] C. S. Henkee, E. L. Thomas, and L. J. Fetters, *Journal of Materials Science*, 1988, **23**(5), 1685–1694.
- [89] A. Karim, N. Singh, M. Sikka, F. S. Bates, W. D. Dozier, and G. P. Felcher, *J. Chem. Phys.*, 1994, **100**(2), 1620–1629.

- [90] L. H. Radzilowski, B. L. Carvalho, and E. L. Thomas, *Journal of Polymer Science Part B-Polymer Physics*, 1996, **34**(17), 3081–3093.
- [91] M. Konrad, A. Knoll, G. Krausch, and R. Magerle, *Macromolecules*, 2000, **33**(15), 5518–5523.
- [92] C. Harrison, M. Park, P. Chaikin, R. A. Register, D. H. Adamson, and N. Yao, *Macromolecules*, 1998, **31**(7), 2185–2189.
- [93] C. Harrison, M. Park, P. Chaikin, R. A. Register, D. H. Adamson, and N. Yao, *Polymer*, 1998, **39**(13), 2733–2744.
- [94] Q. L. Zhang, O. K. C. Tsui, B. Y. Du, F. J. Zhang, T. Tang, and T. B. He, *Macromolecules*, 2000, **33**(26), 9561–9567.
- [95] G. G. Pereira, *Phys. Rev. E*, 2001, **63**, 061809.
- [96] D. Sundrani, S. B. Darling, and S. J. Sibener, *Nano Lett.*, 2004, **4**, 273–276.
- [97] E. W. Edwards, M. F. Montague, H. H. Solak, C. J. Hawker, and P. F. Nealey, *Adv. Mater.*, 2004, **16**, 1315–1319.
- [98] S. O. Kim, B. H. Kim, K. Kim, C. M. Koo, M. P. Stoykovich, P. F. Nealey, and H. H. Solak, *Macromolecules*, 2006, **39**, 5466–5470.
- [99] T. Xu, J. Wang, and T. P. Russell in *Nanostructured Soft Matter: Experiment, Theory, Simulation and Perspectives*, ed. Zvelindovsky; Springer Verlag, Heidelberg, 2007; pp. 171–198.
- [100] R. A. Segalman, K. E. Schaefer, G. H. Fredrickson, E. Kramer, and S. Magonov, *Macromolecules*, 2003, **36**, 12.
- [101] C. Harrison, D. H. Adamson, Z. Cheng, J. M. Sebastian, S. Sethuraman, D. A. Huse, R. A. Register, and P. M. Chaikin, *Science*, 2000, **290**, 1558–1561.
- [102] J. Hahn, W. A. Lopes, H. M. Jaeger, and S. J. Sibener, *J. Chem. Phys.*, 1998, **109**, 10111–10114.
- [103] J. Hahn and S. J. Sibener, *J. Chem. Phys.*, 2001, **114**, 4730–4740.
- [104] M. R. Hammond, E. Cochran, G. H. Fredrickson, and E. J. Kramer, *Macromolecules*, 2005, **38**, 6575–6585.

- [105] M. R. Hammond and E. J. Kramer, *Macromolecules*, 2006, **39**(4), 1538–1544.
- [106] D. Constantin and P. Oswald, *Phys. Rev. Lett.*, 2000, **85**, 4297.
- [107] R. A. Segalman, *Materials Science & Engineering, R: Reports*, 2005, **R48**, 191–226.
- [108] R. D. Peters, X. M. Yang, and P. F. Nealey, *Macromolecules*, 2002, **35**(5), 1822–1834.
- [109] J. Heier, E. J. Kramer, J. Groenewold, and G. H. Fredrickson, *Macromolecules*, 2000, **33**(16), 6060–6067.
- [110] J. Heier, E. Sivaniah, and E. J. Kramer, *Macromolecules*, 1999, **32**(26), 9007–9012.
- [111] Y. Liu, W. Zhao, X. Zheng, A. King, A. Singh, M. H. Rafailovich, J. Sokolov, K. H. Dai, and E. J. Kramer, *Macromolecules*, 1994, **27**(14), 4000–10.
- [112] A. Menelle, T. P. Russell, S. H. Anastasiadis, S. K. Satija, and C. F. Majkrzak, *Phys. Rev. Lett.*, 1992, **68**(1), 67–70.
- [113] M. Maaloum, D. Ausserre, D. Chatenay, G. Coulon, and Y. Gallot, *Phys. Rev. Lett.*, 1992, **68**(10), 1575–1578.
- [114] P. C. M. Grim, I. A. Nyrkova, A. N. Semenov, G. Tenbrinke, and G. Hadziioannou, *Macromolecules*, 1995, **28**(22), 7501–7513.
- [115] K. S. Lyakhova, A. Horvat, A. V. Zvelindovsky, and G. J. A. Sevink, *Langmuir*, 2006, **22**(13), 5848–5855.
- [116] H. Morita, T. Kawakatsu, and M. Doi, *Macromolecules*, 2001, **34**(25), 8777–8783.

4 Phase behavior in thin films of cylinder-forming *ABA* block copolymers: Mesoscale modeling

Horvat A., Lyakhova K. S., Sevink G. J. A., Zvelindovsky A. V. and Magerle R.
published in *J.Chem.Phys.*, 2004, *120*, 1117–1126.

The phase behavior of cylinder-forming *ABA* block copolymers in thin films is modeled in detail using dynamic density functional theory and compared with recent experiments on polystyrene-*block*-polybutadiene-*block*-polystyrene triblock copolymers. Deviations from the bulk structure, such as wetting layer, perforated lamella, and lamella, are identified as surface reconstructions. Their stability regions are determined by an interplay between surface fields and confinement effects. Our results give evidence for a general mechanism governing the phase behavior in thin films of modulated phases.

4.1 Introduction

Block copolymers self-assemble into ordered structures with characteristic lengths determined by the molecular size, which is in the 10-100 nm range.^{1,2} This property has attracted much interest in the area of soft condensed matter physics and nanotechnology. There is large interest to understand, predict, and control structure formation in this class of ordered polymeric fluids.

In bulk, the block copolymer microdomain structure is determined mainly by the molecular architecture and the interaction between the different components (blocks). At the air-polymer interface and the film-substrate interface additional driving forces for structure formation exist. Typically, one component has a lower interfacial energy than the other. This causes a preferential attraction of one type of block to the interface (or surface), which can result either in an alignment of the bulk structure at the interface^{3–5} and/or a deviation of the microdomain structure from the bulk. These deviations in the vicinity of the interface have been shown to be analogous to surface reconstructions of crystal surfaces.⁶

In thin films, additional constraints play an important role. Here, the microdomain structure has to adjust to two interfaces and a certain film thickness, which can be a noninteger multiple of the microdomain spacing in the bulk. Both constraints together cause a complex and interesting phase behavior.

Since the seminal work of Anastasiadis *et al.*,³ the behavior of lamellae forming block copolymers in thin films has been studied in detail and two major effects have been identified (for reviews, see Refs. 7-9). The preferential attraction of one type of block to the surface (the surface field) causes the lamella to align parallel to interfaces and the film forms islands or holes where the film thickness is a (half) integer multiple of the lamella spacing in the bulk. In cases where the film thickness is not compatible with the natural bulk domain spacing or when the film/air and the film/substrate interface is not selective, lamellae can orient perpendicular to the interfaces.^{4,5}

The behavior of cylinder forming systems is more complex and less understood. Here, the natural hexagonal packing of cylinders cannot be retained close to the planar interface, which, regardless of its orientation, always breaks the symmetry of the bulk structure. As a result, besides cylinders oriented parallel and perpendicular to the surface,¹⁰⁻¹³ a variety of deviations from the bulk structure have been observed near surfaces and in thin films, such as a disordered phase,¹⁰ a wetting layer,¹⁴ spherical microdomains,¹⁵ a perforated lamella,¹⁵ as well as more complicated hybrid structures such as cylinders with necks,¹⁶ a perforated lamella with spheres,¹⁷ and an inverted phase.¹⁸

Various theories have been used to describe this behavior.¹⁹⁻²⁶ A brief summary of experimental and simulation results is given in Ref. 24. With dynamic density functional theory (DDFT), a dynamic variant of self-consistent field theory, Huinink *et al.*^{21,22} have calculated a phase diagram for thin films of cylinder forming diblock copolymers. They found that noncylindrical structures are stabilized by the surface field in the vicinity of surfaces and in thin films. With increasing strength of the surface field a sequence of phase transitions was predicted: from a wetting layer, to cylinders oriented perpendicular to the surface, to cylinders oriented parallel to the surface, to a hexagonally perforated lamella, and to a lamella.

Theoretical and experimental results agree qualitatively only in part. From the experimental point of view, only single deviations from the bulk structure and no phase diagrams have been reported. Therefore it remains unclear which of the reported phenomena are specific to the particular block copolymer and/or route of film preparation and which are general behavior. From the modeling point of view, no model predicts all experimentally observed phases. In particular, a detailed and quantitative comparison between modeling and experimental results is missing. The underlying fundamentals remain unclear.

Recently, Knoll *et al.*²⁷ have measured the phase diagram for thin films of concentrated so-

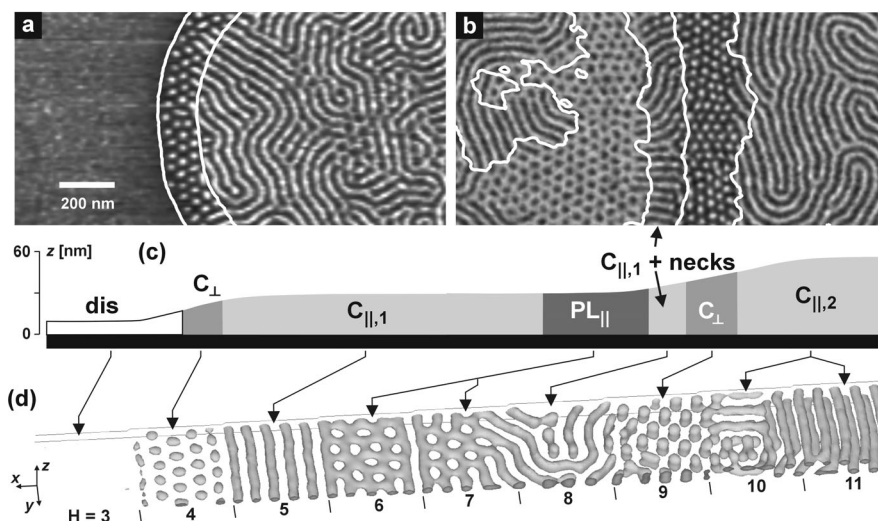


Figure 1: (a), (b) *TappingModeTM* scanning force microscopy phase images of thin polystyrene-block-polybutadiene-block-polystyrene (SBS) films on silicon substrates after annealing in chloroform vapor. The surface is covered with a homogeneous ≈ 10 -nm-thick PB layer. Bright (dark) corresponds to PS (PB) microdomains below this top PB layer. Contour lines calculated from the corresponding height images are superimposed. (c) Schematic height profile of the phase images shown in (a) and (b). (d) Simulation of an $A_3B_{12}A_3$ block copolymer film in one large simulation box with from left to right increasing film thickness $H(x)$, $\epsilon_{AB} = 6.5$, and $\epsilon_M = 6.0$. The isodensity surface $\rho_A = 0.5$ is shown. [Reprinted from: A. Knoll *et al.*, *Phys. Rev. Lett.* **89**, 035501 (2002)]

lutions of a polystyrene-*block*-polybutadiene-*block*-polystyrene (SBS) triblock copolymer in chloroform as function of film thickness and polymer concentration. In this communication²⁷ we have presented matching computer simulations of thin films of *ABA* triblock copolymers which model in stunning detail the experimentally observed phase behavior. As an example, Fig. 1 shows a comparison of the experimental results of Knoll *et al.*²⁷ and our simulations of a corresponding $A_3B_{12}A_3$ triblock copolymer film, where the interfaces preferentially attract the *B* block. In Fig. 1 the film thickness increases from left to right and a rich variety of structures is observed. With increasing film thickness, both experiments and calculations show the same sequence of thin film phases: a disordered film (dis) for the smallest thickness, *A* spheres or very short upright *A* cylinders (C_{\perp}), *A* cylinders oriented parallel to the film plane ($C_{\parallel,1}$), a perforated *A* lamella (PL), parallel oriented *A* cylinders with an elongated cross section and necks, perpendicular oriented *A* cylinders (C_{\perp}), and finally two layers of parallel oriented *A* cylinders ($C_{\parallel,2}$). The phase transitions occur at well-defined film thickness as can be seen from the white contour lines that represent points of equal film thickness [Figs. 1(a) 1(b)].

As measured three-dimensional volume images of a thin films microdomain structure are

rather rare.^{16,17,28,29} DDFT simulations as shown in Fig. 1(d) facilitate us to interpret the experimentally easy observed surface structures in terms of the volume structure of the films. Furthermore, compared to the experiments^{27,30} and previous simulations on diblock copolymers,^{21,22} our simulations cover a much larger parameter space. Only this enabled us to distinguish between the different physical phenomena governing the phase behavior in thin films. The phenomena and their interplay can be summarized in the following way: (1) The *surface field* can either orient the bulk structure or it can stabilize deviations from bulk structures, such as wetting layer, perforated lamella, and lamella, which we identified as *surface reconstructions*.⁶ (2) The *film thickness* is modulating the stability regions of the effects.

The aim of this paper is to give a detailed report of our simulation results. The experimental part is reported in the preceding companion article.³⁰ First, we report briefly the phase behavior of an $A_3B_{12}A_3$ melt in the bulk. Then we focus on the phase behavior of cylinders forming systems in thin films. The basic types of surface structures and surface reconstructions are introduced and the underlying physics is explained. Finally, we compare our results with the corresponding experiments of Knoll *et al.*³⁰ and the phase behavior of other cylinder and lamella forming block copolymers.

4.2 Method

We have modeled the phase behavior in thin films with mean-field DDFT, which was developed by Fraaije *et al.*^{31–33} for mesoscale modeling the phase separation and ordering processes of multicomponent polymeric systems. For our simulations we used the standard MESODYN code.³⁴

As a molecular model an ideal Gaussian chain is used. In this "spring and beads" model, springs mimic the stretching behavior of a chain fragment and different kinds of beads correspond to different components in the block copolymer. All nonideal interactions are included via a mean field and the strength of interaction between different components is characterized by the interaction parameter ϵ_{AB} , which we express in units of kJ/mol. This parameter can be related to the conventional Flory-Huggins parameter χ (see Sec. 4.3.1). Interfaces are treated as hard walls, with the flux perpendicular to the interface and the density at the interface kept equal to zero.³³ The interaction between components and interfaces is characterized by corresponding mean field interaction parameters ϵ_{AM} and ϵ_{BM} . As only the difference between the interaction parameters is relevant for structure formation³³ we used an effective interface-polymer interaction parameter $\epsilon_M = \epsilon_{AM} - \epsilon_{BM}$, which characterizes the strength of the surface field. A positive ϵ_{IJ} parameter corresponds to a repulsion between the components I and J . The dynamics of the component densities $\rho_I(\vec{r}, t)$, with $I = A, B$, is described by a set of functional

Langevin equations. These are diffusion equations of the component densities which take into account the noise in the system. Driving forces for diffusion are local gradients of chemical potentials $\mu_I = \delta F[\{\rho_I\}]/\delta \rho_I$. The Langevin diffusion equations are solved numerically with homogeneous initial conditions. As MESODYN is based on the same type of free energy functional as self-consistent field theory (SCFT),³⁵ it is expected to approach on long time scales the same solutions as SCFT does by searching for the absolute minimum of the free energy. With MESODYN, however, structure formation proceeds via local gradients of chemical potentials that are intrinsic to the system. In this way, long lived transition states can also be visited in a simulation run. This ambiguity, however, is shared with the experiments, where the specimen is also quenched after a finite annealing time.³⁰

The simulations were done on a cubic grid of dimensions $X \times Y \times (H + 1)$, with the interface positioned at $z = 0$. Due to the periodicity of boundary conditions, the system is confined between two interfaces separated by H grid points. The triblock copolymer is modeled as a melt of $A_3B_{12}A_3$ chains, which can be seen as two connected A_3B_6 chains. The architecture of the $A_3B_{12}A_3$ chain enters specifically in the calculation of the density fields from the external potentials and in the partition function, respectively, the free energy.^{31–33} For our simulations we partly relied on previous results (Refs. 21 and 22). Apart from the chain architecture all simulation parameters are the same as for the A_3B_6 diblock system studied in Refs. 21 and 22, with an exception for the interaction parameter ϵ_{AB} . In addition, we have varied this interaction parameter in a range where the $A_3B_{12}A_3$ system forms cylinders in the bulk. Doing so we can also study the influence of the molecular architecture on the observed phenomena by comparing our results on $A_3B_{12}A_3$ triblock copolymer with the behavior of the corresponding A_3B_6 diblock copolymer. At the same time, this study allowed us to determine the value of the interaction parameter ϵ_{AB} that best matches the experimental situation. As in Refs. 21 and 22, we followed the temporal evolution in the system until significant changes of the free energy, the order parameter, and the microdomain structure no longer occurred.

4.3 Results

4.3.1 Bulk structure

As a first step, we parametrized the system studied experimentally by Knoll *et al.*^{27,30} For this, we investigated the phase behavior in the bulk and determine the range of ϵ_{AB} where the system forms cylinders. In Fig. 2 the phase diagrams of a melt of ABA triblock copolymers with A -volume fraction $f_A = 1/3$ are shown, which were calculated with DDFT and SCFT.³⁶ The Flory-Huggins parameter χ and ϵ_{AB} are related through $\chi = (v^{-1}/2kT) [2\epsilon_{AB} - \epsilon_{AA} - \epsilon_{BB}]$

[Eq. (32) in Ref. 32]. In our case, with $\nu = 1$, $\epsilon_{AA} = \epsilon_{BB} = 0$, $N = 18$, and $T = 413$ K, $\chi N \approx \epsilon_{AB} \times 5.43$ mol/kJ.

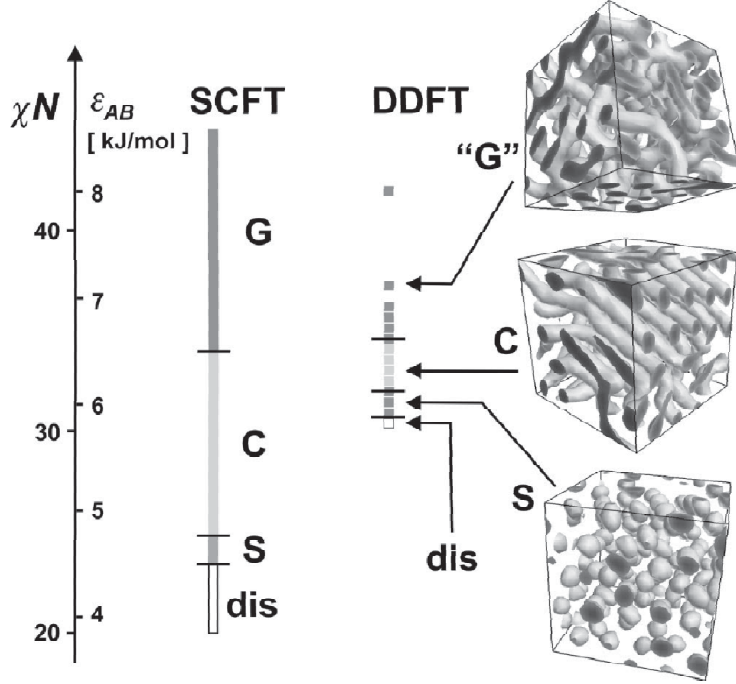


Figure 2: Bulk phase diagrams for ABA triblock copolymer melts with $f_A = 1/3$ as a function of interaction parameters χN and ϵ_{AB} . Results of Matsen (Ref. 30) obtained with SCFT are compared with our results calculated with DDFT for an $A_3B_{12}A_3$ melt in $32 \times 32 \times 32$ large simulation boxes. Phases are labeled as G (gyroid), G (gyroid-like), C (cylinders), S (spheres), and dis (disordered).

The phase separation process was simulated with DDFT in a cubic box with $32 \times 32 \times 32$ grid points and periodic boundary conditions. The calculations were started with a homogeneous melt. During the simulation run we observe similar processes as previously reported.³¹ First the segregation of the A and B blocks into interconnected domains takes place. The separation process continues with the break-up of an initially connected network of different domains into well-defined structures. Microdomains with different orientations form simultaneously during the phase separation process, which leads to a very defective structure. The last and slowest process is the long-range ordering of the microdomain structure, which proceeds via annealing of defects. Our calculations were done until 4000 time steps, where the long-range ordering process is still not completed. Nevertheless, the result is sufficient to characterize the formed microdomain structure. For $\epsilon_{AB} \leq 5.75$ no phase separation occurs. The A density ρ_A is spatially inhomogeneous with a mean value (averaged over all grid points) of 0.33 and standard deviation of 0.03. The mean value of 0.33 corresponds to the volume fraction f_A of the A component.

As the interaction parameter ϵ_{AB} increases, A -rich domains of spherical shape (S) form in a B -rich matrix for $5.8 \leq \epsilon_{AB} \leq 6.0$. In the range $6.1 \leq \epsilon_{AB} \leq 6.5$, well-separated cylindrical A microdomains (C) embedded in the B matrix were observed. For $\epsilon_{AB} \geq 6.6$, we observe an A -rich network of microdomains embedded in a B -rich matrix. Because of the large amount of three-fold connections we relate this structure to a defective gyroid phase. We have also done simulations in smaller simulation boxes, $16 \times 16 \times 16$ in size, and obtained similar results but with better ordered structures.

For $\epsilon_{AB} = 6.5$ we determined the distance between cylinders in the bulk. For this purpose we did a simulation in a $64 \times 64 \times 1$ large box, analogous to Huinink *et al.*²¹ Here, due to the periodic boundary conditions, the cylinders orient perpendicular to the 64×64 plane and show up as hexagonally packed dots. The distance between next-nearest cylinders was determined to be $a_o = 6.9 \pm 0.5$ grid units.

Our results are similar to those obtained with SCFT. With increasing interaction parameter both methods predict transitions from a disordered state to spheres, then cylinders, and a gyroid phase. We observe the transition from the disordered state to spheres at a higher value of ϵ_{AB} than predicted by Matsen *et al.*³⁶ The discrepancy could be due to the relatively small size of the chain and the nonlocality of the nonideal interactions.³² The phase boundary between the cylinder and gyroid phase is the same in both simulation results and this region of the phase diagram is of particular interest of the present study. An obvious difference is the presence of defects in the microdomain structures simulated with DDFT, which Matsens SCFT does not take into account. If defects cost very little energy a rather high density of defects might be thermally excited in the system.

4.3.2 Surface reconstruction

We now turn to the question of what happens when interfaces are added to the system. On varying the film thickness, H , and the strength of the surface field, ϵ_M , we observe a complex phase behavior. The presence of interfaces has several effects. One is a speed-up of the long range order formation. In Fig. 3 two systems with different boundary conditions and otherwise identical parameters are compared: an $A_3B_{12}A_3$ melt with $\epsilon_{AB} = 6.5$ in the bulk [Fig. 3(a)] and in a film with $H = 54$ [Fig. 3(b)]. The surface field was chosen to be $\epsilon_M = 6$. In both systems, the simulation time was 4000 time steps and both show cylinders. In the film, the temporal evolution of structure formation is similar to that of a bulk system. In addition, however, the cylinders start to align at the interfaces and the alignment propagates from the surface into the film. This causes the cylinders in the film to orient parallel to the surface and to pack in a neat hexagonal array [Fig. 3(b)]. In the bulk, however, the microdomain structure is still very

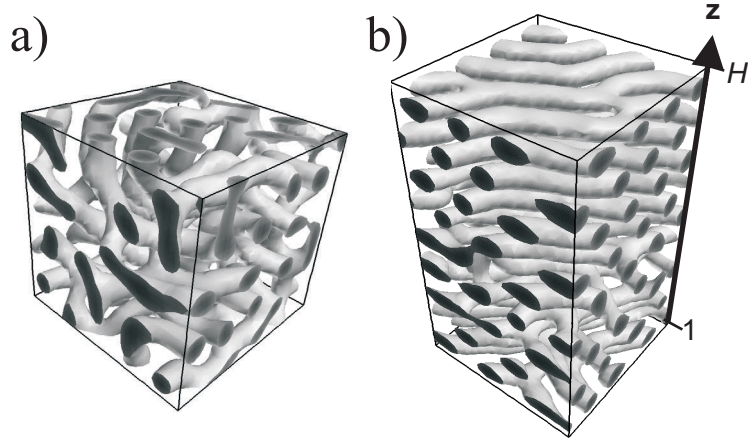


Figure 3: *Effect of the surface on the long range ordering process. Simulations for a cylinder forming system with interaction parameter $\varepsilon_{AB} = 6.5$ after 4000 time steps. (a) In the bulk, in a $32 \times 32 \times 32$ large simulation box. (b) In a confined film, where $X = Y = 32$ and $H = 54$, surfaces at $z = 0$ and 55 , and the effective surface-polymer interaction parameter $\varepsilon_M = 6$.*

defective [Fig. 3(a)]. Although the simulation box of the film system is larger than that of the bulk simulation it shows a higher degree of long-range order.

The most intriguing effect of the presence of interfaces are deviations from the bulk microdomain structure in the vicinity of the interface. This effect is called surface reconstruction and it is best seen at large film thicknesses, for instance at $H = 54$ (Fig. 4). In such films the interfaces are separated by approximately nine layers of cylinders and in the vicinity of one interface the influence of the other one is negligible. In the middle of the film, in most cases the microdomain structure remains hexagonally ordered cylinders aligned parallel to the film plane. Depending on the strength of the surface field, considerable rearrangements of microdomains near the interfaces, i.e., surface reconstructions, occur. For $\varepsilon_M < 2$, the A component is preferentially attracted to the interface and a wetting layer (W) is formed. When ε_M increases, cylinders oriented perpendicular to the surface are stabilized for $\varepsilon_M \approx 3$. As ε_M is further increased, the A component is weakly repelled from the interface and cylinders orient parallel to the surface in the range $\varepsilon_M \approx 4 - 9$. For larger ε_M , surface reconstructions with noncylindrical microdomains are induced: first, at $\varepsilon_M \approx 10$, a transition to a perforated lamellae (PL) occurs in the layer next to the surface which transforms to a lamellae (L) at $\varepsilon_M \approx 25$.

For the surface structures shown in Fig. 4 we examined the density distribution of each component. In Fig. 5(a) the (x,y) plane averaged A density $\langle \rho_A \rangle_{x,y}$ is plotted as function of the distance z . For all three ε_M values (5, 10, and 30), a modulation is observed, which corresponds

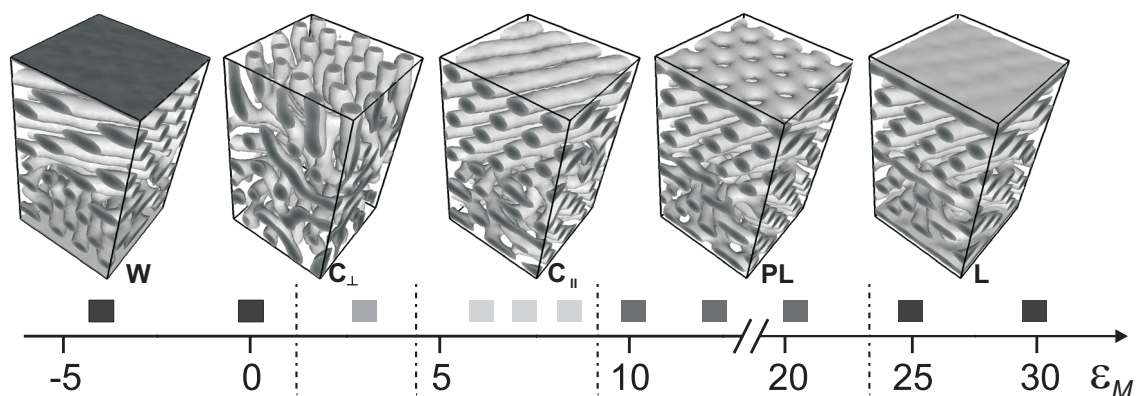


Figure 4: *Effect of the strength of the surface field ϵ_M on microdomain structures and surface reconstructions. Simulation results for an $A_3B_{12}A_3$ melt ($\epsilon_{AB} = 6.5$) in a rather thick film ($H = 54$) with surfaces at $z = 0$ and 55 at $\epsilon_M = -4, 3, 7, 12, 30$. Isodensity surfaces ($\rho_A = 0.45$) are shown for typical structures. Gray boxes indicate ϵ_M values where simulations have been done.*

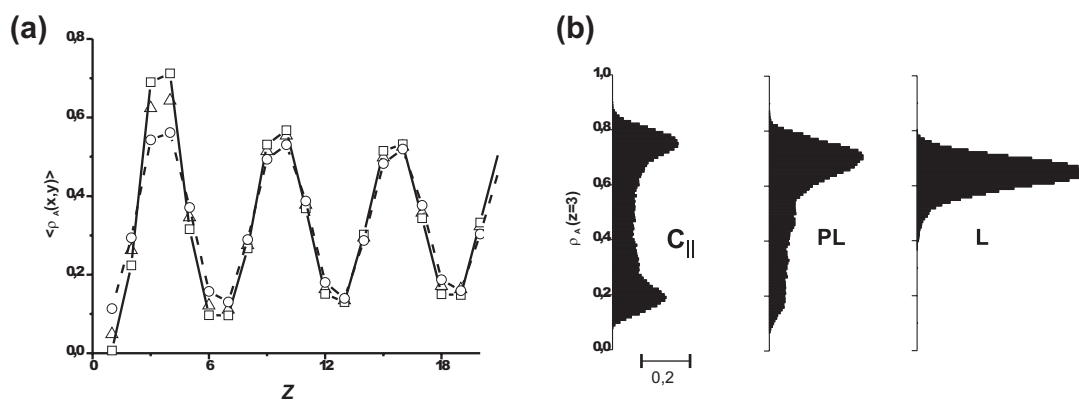


Figure 5: *Effect of the strength of the surface field on the distribution of A density. (a) The laterally averaged A density $\langle \rho_A \rangle_{x,y}$ as function of the distance z from the surface (depth profiles) for different surface fields and surface reconstructions: (circles) parallel cylinders, $\epsilon_M = 5$; (triangles) perforated lamellae, $\epsilon_M = 10$; (squares) lamellae, $\epsilon_M = 25$. (b) Histograms of the lateral averaged A density $\langle \rho_A \rangle_{x,y}$ at $z = 3$, approximately in the middle of the first A-rich microdomain next to the surface, for the surface fields shown in (a).*

to a layered microdomain structure oriented parallel to the interface. In all three of the displayed cases the B component is attracted to the interface. This causes a depletion of the A component at the interface and an increase of ρ_A in the middle of the first A microdomain next to the interface. The effect increases with increasing surface field ε_M and it is accompanied with formation of different surface reconstructions. At $z = 3$, approximately in the middle of the first A -rich microdomain next to the interface, ρ_A increases with increasing surface field ε_M from $\rho_A = 0.55$ for cylinders ($\varepsilon_M = 5$), to $\rho_A = 0.62$ for the perforated lamella ($\varepsilon_M = 10$), and 0.70 for the lamella surface reconstruction ($\varepsilon_M = 30$). In Fig. 5(b), the lateral distributions of the A density at $z = 3$ are plotted as histograms for the same values of the surface field as in Fig. 5(a). Results for $\varepsilon_M = 5$ show a broad density spectrum with two peaks, which correspond to the presence of two microphase separated components: A -rich cylinders and the B matrix. For $\varepsilon_M = 12$, the distribution is still broad and A is the majority component in this layer, the isodensity surface is a perforated lamella. For $\varepsilon_M = 30$, the density distribution shows one narrow peak, as expected for a lamella. These results indicate that with increasing surface field the density variations parallel to the interface are suppressed in the vicinity of the interface. In these structures the averaged mean curvature is gradually decreased in order to adopt to the planar symmetry of the interface.

4.3.3 One microdomain thick films

We now turn to the effect of the film thickness H . In thinner films two additional factors influence the microdomain structure in the film: the interference of the two surface fields (of the bottom and the top interface) and the commensurability of the natural domain spacing with the film thickness. First, we present the interference effect of surface fields for $H = 6$, which corresponds to one layer of cylinders (Fig. 6). For this thickness we observe similar structures as in thick films ($H = 54$) in the vicinity of the interface. For $H = 6$, however, the strength of surface field needed to form noncylindrical microdomains is strongly reduced. We observe the lamella phase already for $\varepsilon_M = 7$, compared to $\varepsilon_M = 25$ for $H = 54$. Also the perforated lamella phase appears already at $\varepsilon_M = 6$ instead of $\varepsilon_M = 10$ and it has a much smaller existence range. Perpendicular cylinders, which at $H = 6$ are very short and almost spheres, appear in both cases at $\varepsilon_M = 3$. An additional feature of thin films is the presence of a disordered phase with no well-defined microdomain structure, however, with the two components A and B being still slightly segregated. Figure 7 shows depth profiles of the laterally averaged A density for different structures in thin films of thickness $H = 6$. For $\varepsilon_M \leq 1$, the A block is preferentially attracted to the surface and a wetting layer forms at each surface. For $1 \leq \varepsilon_M \leq 2$ the disordered phase forms and the A component is only weakly attracted to the interface. Interfaces with $\varepsilon_M = 3$ appear as neutral. For this surface field value very short cylinders oriented perpen-

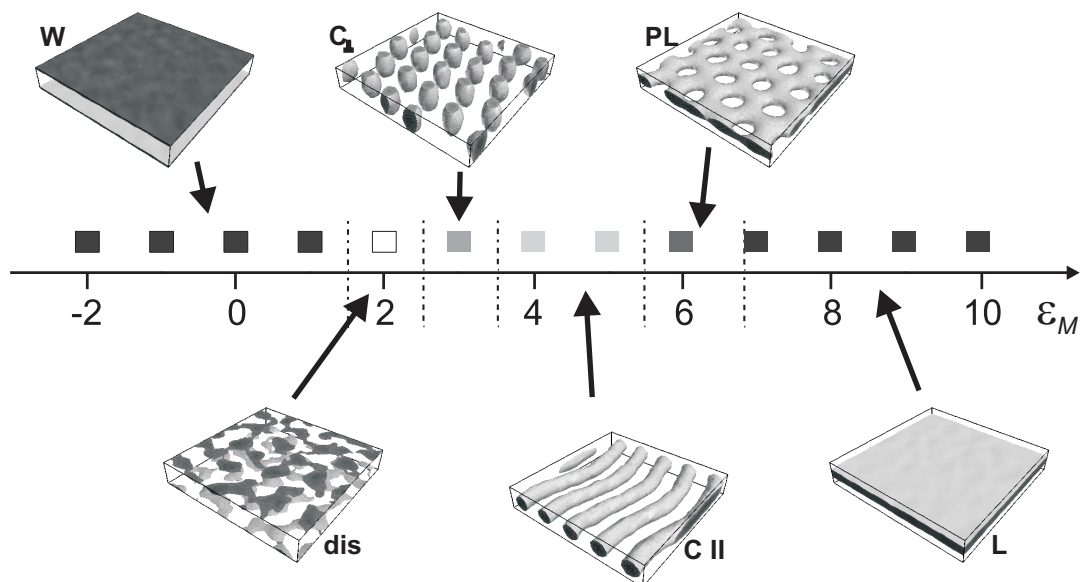


Figure 6: Simulation results for a cylinder forming $A_3B_{12}A_3$ melt ($\epsilon_{AB} = 6.5$) in thin films ($H = 6$) with different strength of the surface field ϵ_M . Isodensity profiles ($\rho = 0.45$) for typical structures are shown. Gray boxes indicate parameters were simulations have been done.

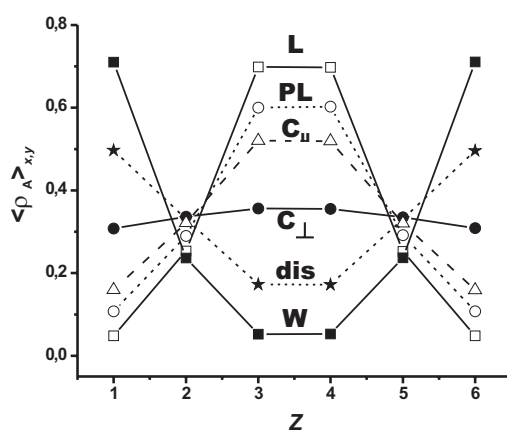


Figure 7: Effect of the strength of the surface field on the depth profiles of the laterally averaged A density $\langle \rho_A \rangle_{x,y}$ in thin films. Depth profiles are shown for: (open squares) a lamella at $\epsilon_M = 9$, (open circles) a perforated lamella at $\epsilon_M = 7$, (triangles) cylinders oriented parallel to the surface at $\epsilon_M = 5$, (filled circles) cylinders oriented perpendicular to the surface at $\epsilon_M = 3$, (stars) a disordered phase at $\epsilon_M = 2$, and (filled squares) a wetting layer at $\epsilon_M = -2$.

dicular to the surface are formed. The fact that the interface appears neutral at $\varepsilon_M = 3$ and not at $\varepsilon_M = 0$ can be explained by an entropic attraction of the shorter A block to the interface.²¹ For $\varepsilon_M > 3$ the surface preferentially attracts the B block and A -rich microdomains form in the middle of the film.

4.3.4 Phase diagrams of surface reconstructions

We have done simulations with $\varepsilon_{AB} = 6.3, 6.5,$ and 7.1 and have varied the strength of the surface field, ε_M , and the film thickness, H . We have also calculated a phase diagram where we varied ε_{AB} and ε_M simultaneously while keeping $\varepsilon_{AB} = \varepsilon_M$. Figures 8 and 9 show the phase diagrams of surface reconstructions for $\varepsilon_{AB} = 6.5$ and 6.3 , respectively. For both values cylinders are formed in the bulk (see Fig. 2) as well as in the middle of the films. Both phase diagrams clearly show that microdomain structures oriented parallel to the surface are dominant. Cylinders orient perpendicular to the surface for the neutral surfaces at $\varepsilon_M \approx 3$ and at certain thicknesses ($H = 9$ and 15) which strongly deviate from an integer multiple of a natural layer thickness. For hexagonally packed cylinders the natural thickness is $c_o = a_o\sqrt{3}/2$, where a_o is the distance between next-nearest cylinders in the bulk. In our case (see Sec. 4.1.3.A), $a_o = 6.9 \pm 0.5$ and the natural thickness of one layer of cylinders is $c_o \approx 6$.

Interference of surface fields. The important feature of the thin film phase behavior is the existence of surface reconstructions with noncylindrical morphologies: the wetting layer, the perforated lamella, and the lamella. For thick films with $H > 3c_o$ the critical surface field required to induce a surface reconstruction is independent of the thicknesses. For thinner films, this threshold value decreases: for the perforated lamella, $\varepsilon_M \approx 10, 8, 7,$ and 6 at $H = 9c_o, 3c_o, 2c_o,$ and c_o , respectively. This indicates that surface fields extend into the bulk with a decay length of about one microdomain spacing. Furthermore, they are additive and for very thin films the effects of both surfaces combine. This explains why in thin films a weaker surface field is sufficient to form a PL (or L) than in thick films. It also explains the formation of a PL beneath a wetting layer for $\varepsilon_M = 0$ at $H = 12$ and $\varepsilon_M = -2$ at $H = 19$.

Confinement effects modulate the stability regions of phase oriented parallel to the interfaces. An integer multiple of a natural layer thickness is energetically favored. This causes easier deformable phases to occur at intermediate film thicknesses. For very small thicknesses ($H < c_o$) and weak surface fields, confinement prevents microphase separation and stabilizes a disordered phase.

The phase diagram for $\varepsilon_{AB} = 6.3$ (Fig. 9) displays a very similar behavior to the one for $\varepsilon_{AB} = 6.5$ (Fig. 8). The two main differences between the two phase diagrams is that for $\varepsilon_{AB} = 6.3$ the stability region of the disordered phase is larger and that the threshold values for the formation of surface reconstruction are shifted to larger strengths of the surface field, in particular for the

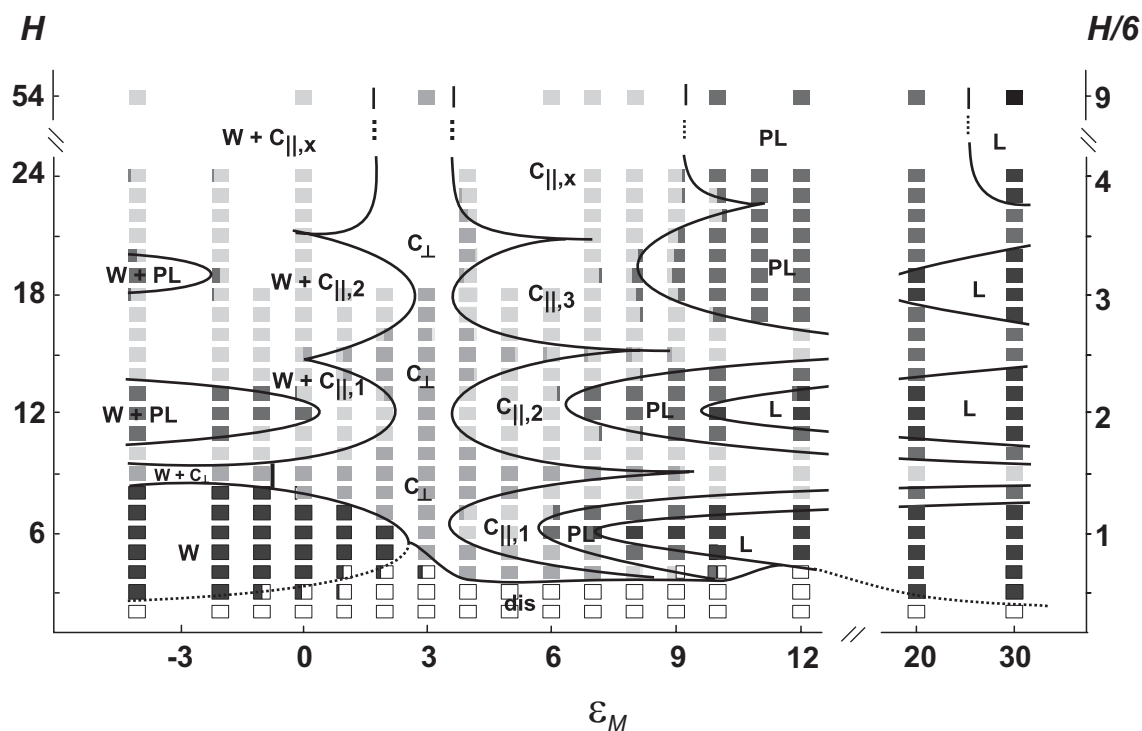


Figure 8: Phase diagram of surface reconstructions calculated for an $A_3B_{12}A_3$ melt with $\epsilon_{AB} = 6.5$ as function of film thickness H and surface field ϵ_M . Boxes indicate where simulations have been done. Boxes with two shades of gray indicate that two phases coexist after the finite simulation time. Smooth phase boundaries have been drawn to guide the eyes. The right scale indicates the film thickness in units of the natural layer thickness $c_o \approx 6$.

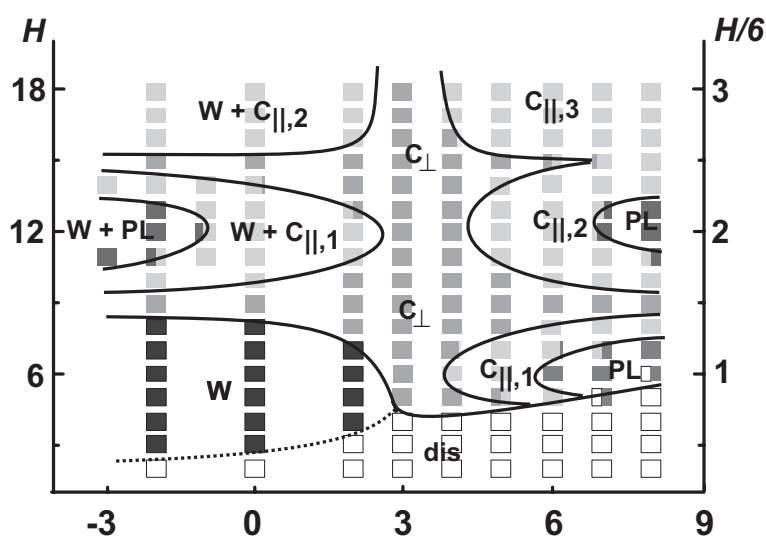


Figure 9: Same as Fig. 7 but for $\epsilon_{AB} = 6.3$.

lamella surface reconstruction.

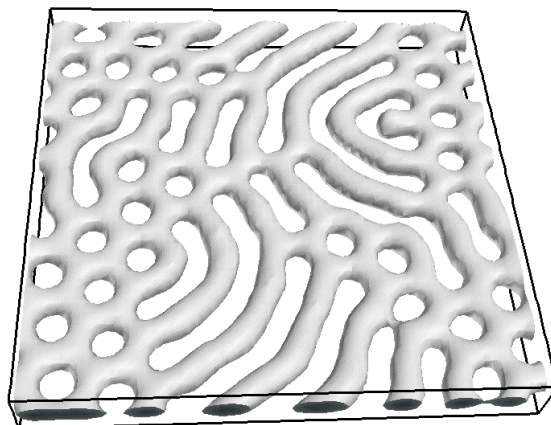


Figure 10: *Coexistence of parallel cylinders and perforated lamellae for an $A_3B_{12}A_3$ melt with $\epsilon_{AB} = 6.5$, $\epsilon_M = 6.0$, and $H = 7$. The isodensity level is $\rho_A = 0.45$. The size of the simulation box is $64 \times 64 \times 8$.*

Order of phase transitions. An important feature of our simulations is the coexistence of different phases in one layer. Figure 10 shows such a situation where parallel cylinders and a perforated lamella coexist. This simulation was done until 11 000 time steps and after 5000 time steps no significant changes were observed. The coexistence of phases corresponds nicely to the experimental observation [see Fig. 1(b) and Refs. 27 and 30]. The presence of coexistent phase clearly indicates a first-order phase transition. The same is also valid for the PL to L transition. The dashed lines in the phase diagrams denote continuous transitions between the W and "dis", and the "dis" and L phase.

4.3.5 Structured wetting layer

A result not displayed in the phase diagrams is the structure of the wetting layer. For thin films ($4 \leq H \leq 8$), where the entire film consists only of two wetting layers, the wetting layer has no lateral structure. However, in thicker films and for small values of the surface field ($-1 \leq \epsilon_M \leq 2$) the wetting layer has a structure which is complementary to the microdomain structure next to it in the middle of the film (Fig. 11). The entire structure shown in Fig. 11(a) is very similar to hexagonally packed cylinders.³⁷ In Fig. 12, histograms of the lateral density distributions within the wetting layer are shown for different values of the surface field ϵ_M . For $\epsilon_M = 1$ and 2, two peaks appear in the histogram which correspond to a lateral microphase

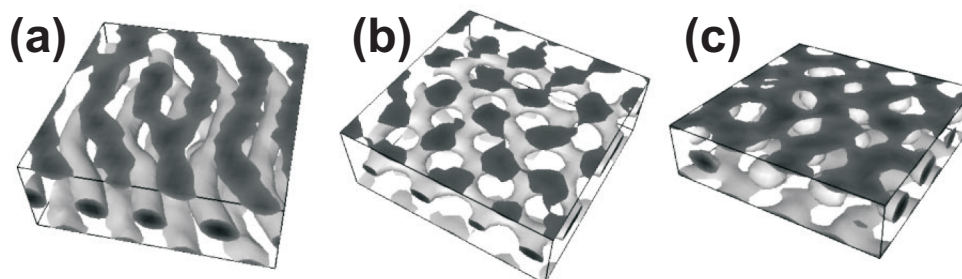


Figure 11: *Structured wetting layers for an $A_3B_{12}A_3$ melt, $\varepsilon_{AB} = 6.5$ [simulation box $32 \times 32 \times (H + 1)$, after 2000 time steps]. (a) $H = 12$, $\varepsilon_M = 2$, and isodensity level $\rho_A = 0.45$; the wetting layer resembles half-cylinders. (b) $H = 12$, $\varepsilon_M = 0$, and isodensity level $\rho_A = 0.45$; the wetting layer consists of isolated dots. (c) A perforated wetting layer at $H = 9$, $\varepsilon_M = -1$, and isodensity level $\rho_A = 0.6$.*

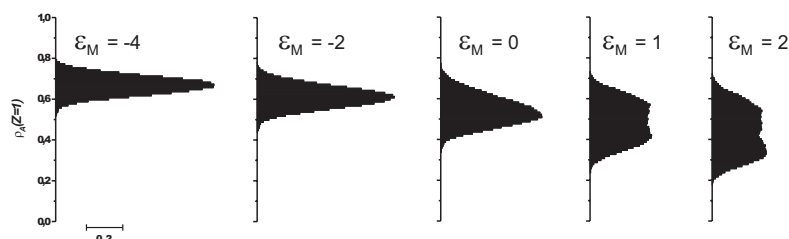


Figure 12: *Effect of the strength of the surface field on the lateral density distribution in the wetting layer. Histograms of the A density at the surface ($z = 1$) are shown for different surface interactions ε_M . Simulations have been done in $32 \times 32 \times 13$ large simulation boxes with $H = 12$. With decreasing ε_M , the A blocks are more strongly attracted to the surface and the lateral homogeneity of the wetting layer increases.*

separation, for example, stripes of A and B density. For smaller values ε_M , the two peak merge, which reflects the fact that the structure continuously transforms to a homogeneous wetting layer. Its histogram is similar to that in the middle of a lamella at $\varepsilon_M = 25$ [see Fig. 5(b)] which supports an interpretation as a half lamella.

4.4 Discussion

4.4.1 Mapping to the experimental phase diagram

Our simulations reproduce all essential features of the experimentally observed phase behavior of thin films of polystyrene-*block*-butadiene-*block*-polystyrene (SBS) triblock copolymers

studied by Knoll *et al.*^{27,30} In particular, the sequence of phases as function of film thickness is correctly modeled. This is nicely seen in Fig. 1 where a simulation done in a wedge-shaped geometry is shown. Also the phase diagrams shown in Figs. 8 and 9 nicely match the experimental one (see Fig. 3 in Ref. 27), indicating that the experimental control parameter, the polymer concentration Φ_P , is directly related to the control parameter in the simulations, namely the surface field ε_M .

In order to keep the model as simple as possible we chose to model the SBS/chloroform solution as a melt of $A_3B_{12}A_3$ block copolymer. As chloroform is a nonselective solvent it acts as a plasticizer, which merely induces chain mobility.^{27,30} The nonselective solvent chloroform screens the interaction between the block copolymer components and the interfaces. This effect is modeled by interaction parameters ε_{AB} and ε_M , which depend on the polymer concentration Φ_P .

The experimentally observed phase diagram (see Fig. 2 in Ref. 27) has three characteristic features: (1) The disordered phase neighbors the C_{\perp} phase for all polymer concentrations. (2) Both regions of the PL phase have a limited range of polymer concentrations where they are stable. (3) The thicker the film, the higher the critical polymer concentration where the PL appears.

We investigate the range of parameters covered by our simulations [Fig.13(a)] which give these three characteristic features. As a first reference point, the phases neighboring the disordered phase are shown in Fig. 13(d). The critical phase boundary $C_{\perp}/C_{\parallel,2}$, which limits the regime where simulations and experimental results are compatible, is shown as a bold dashed line. Figures 13(c) and 13(b) show the phases occurring for $H = c_o$ and $2c_o$ including the characteristic phase boundaries $C_{\parallel,1}/PL$ and $C_{\parallel,2}/PL$, respectively.

We look for paths in the parameter space which include all three characteristic features. This can be done by projecting the surfaces shown in Figs. 13(b), 13(c), and 13(d) on each other, which is done in Fig. 13(e). The paths have to fulfill the following three conditions: (1) They should completely lay in the C_{\perp} region and should not cross the $C_{\perp}/C_{\parallel,1}$ boundary. (2) They should first cross the $C_{\parallel,1}/PL$ and (3) then the $C_{\parallel,2}/PL$ boundary.

The gray region displayed in Fig. 13(e) centers at $\varepsilon_M = 6.0$ and corresponds to a region in the experimental phase diagram centered at $\Phi_P = 0.59$.³⁰ Therefore, the most simple way to parameterize such a path is given by the linear relation $\varepsilon_M = \varepsilon_M^{melt} \Phi_P$, with $\varepsilon_M^{melt} = 10 \pm 1$, which is displayed in Fig. 13(e) as arrow α . The discrepancy with our previous publication²⁷ is due to the fact that the experimental phase diagram was presented in units of the chloroform vapor pressure, whereas here we use the measured polymer concentration from Ref. 30. Nevertheless, both values are close and the physical picture remains the same. By adjusting a single parameter the measured and calculated phase diagrams can be perfectly matched. In particular

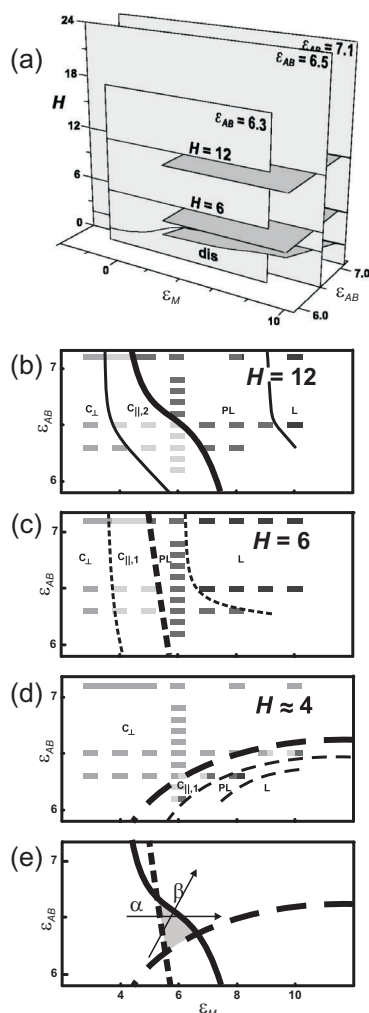


Figure 13: (a) Range of parameters covered by our simulations. The planes $\epsilon_{AB} = 6.3$ and 6.5 correspond to Figs. 8 and 9, respectively. The dark gray surfaces are displayed in detail in (b)(d). (b) Surface reconstructions formed in films with $H = 12$ as function of ϵ_{AB} and ϵ_M . (c) Same as (b) for $H = 6$. (d) Surface reconstructions next to the region of the disordered phase. This region is approximately bounded by $H = 4$. Lines indicate phase boundaries. (e) The phase boundaries $C_{\parallel,2}/PL$, $C_{\parallel,1}/PL$, and $C_{\perp}/C_{\parallel,1}$ taken from (b), (c), and (d), respectively. The arrows α and β correspond to two possible models of how the interaction parameters can change with changing polymer concentration Φ_P . Both models cross the gray region where a characteristic sequence of phases observed in experiments and simulations coincides.

the predicted ε_M values for the onset of the PL phase at $H = 6$ and 12 agree nicely with the experiments. Remarkably, the experiments can be described by a parametrization where only ε_M changes with Φ_P while ε_{AB} is constant. Other possibilities would be arrows like β , where both parameters, ε_{AB} and ε_M , change with Φ_P . The choice of the path a is supported by the experimental observation that the SBS/chloroform system studied by Knoll *et al.*³⁰ forms cylinders in the bulk in the whole range of accessed polymer concentrations. This suggests that the influence of Φ_P on ε_{AB} is rather weak. This is consistent with the fact that the gray region in Fig. 13(e) has a considerable larger extent along the ε_M axis than along the ε_{AB} axis.

4.4.2 Effect of the wetting layer

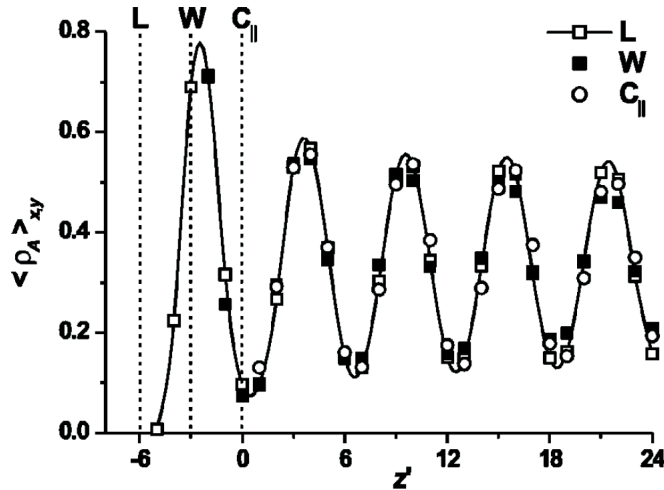


Figure 14: Depth profiles of the laterally averaged A density $\langle \rho_A \rangle_{xy}$ in thin films with $H = 54$ and $\varepsilon_{AB} = 6.5$ for different surface fields. The depth profiles are shifted according to $z' = z$ for $C_{||}$ ($\varepsilon_M = 6$), $z' = z - 3$ for W ($\varepsilon_M = -4$), and $z' = z - 6$ for L ($\varepsilon_M = 30$). The solid line is a spline through the L data.

In Fig. 14 depth profiles of the laterally averaged A density are compared. The profiles of the film forming the lamella and wetting layer surface reconstruction coincide with that of the film forming parallel cylinders when the profile corresponding to the lamella is shifted by c_o and that of the wetting layer is shifted by $c_o/2$. This indicates that the wetting layer can be regarded as a half lamella with thickness $c_o/2$. Furthermore, both the lamella and the wetting layer screen the surface field and the depth profile below them is that of a film forming cylinders oriented parallel to the interface. Effectively, the A -wetting layer induces a B -rich layer at $c_o/2$, which corresponds to a situation at the interface of a film which preferentially attracts the B

component. The lamella screens a strong surface field in a similar way.

In experiments with supported films the interactions at the air/film and the film/substrate interface are in general different. In a situation where one interface attracts the A and the other the B component, the formation of a wetting layer at one interface can lead to a situation where the film can be treated as having effectively both interfaces attracting the B component. Therefore, the phase diagram measured by Knoll *et al.*³⁰ can be well described in simulations with equal interfaces, although the experiments clearly indicate the presence of an A -wetting layer at the film/substrate interface and the preferential attraction of the B component at the air/film interface.

4.4.3 Comparison with cylinder forming diblock copolymers

The influence of the molecular architecture on the observed phenomena can be studied by comparing our results on $A_3B_{12}A_3$ triblock copolymers with the behavior of the corresponding A_3B_6 diblock copolymer studied by Huinink *et al.*²¹ The comparison is made easy since in both studies the same parameters were used and we varied (in addition) the interaction parameter ϵ_{AB} only slightly. For both systems we are well in the part of the phase diagram where cylinders form in the bulk.

At first glance, no utterly significant difference between the phase diagrams of the A_3B_6 diblock copolymer (Fig. 5 in Ref. 21 and Fig. 4 in Ref. 22) and our $A_3B_{12}A_3$ triblock copolymers is visible. Only the position of phase boundaries between different phases differs slightly. This fact leads us to the important conclusion that the observed phenomena and mechanisms are present in many cylinder-forming block copolymers. In particular, the molecular architecture plays only a minor role and enters only via the specific values of the interaction parameters. This is further corroborated by results of Wang *et al.*²⁴ obtained with Monte Carlo simulations, which also show a similar phase behavior for cylinder-forming systems in thin films.

4.4.4 Comparison with lamella-forming diblock copolymers

We note that the orientation behavior of the cylinders is analogous to the phase behavior of lamella-forming diblock copolymers as both are controlled by the interplay between the surface field and confinement effects.^{4,5} Thus, the sequence $C_{\parallel} \rightarrow C_{\perp} \rightarrow C_{\parallel}$ at steps between terraces corresponds to the sequence $L_{\parallel} \rightarrow L_{\perp} \rightarrow L_{\parallel}$.³⁸ Second, in cases where the two confining surfaces favor different orientations (L_{\parallel} , L_{\perp}) the two orientations can coexist and a hybrid (or mixed) structure (HY) forms³⁹ which is similar to cylinders with necks.¹⁶ We note that in such a HY

structure the bulk microdomain structure is preserved and a grain boundary is stabilized in the thin film by the antisymmetric surface field. Furthermore, a disordered phase has been reported for ultrathin films of lamella-forming diblock copolymers^{3,10} and is in nice agreement with our findings and the experiments of Knoll *et al.*^{27,30} In addition to the alignment effect, hexagonally ordered cylinders can adopt to the planar surface by formation of surface reconstructions (W, PL, L) which also dominate the phase behavior in thin films.

4.5 Conclusions

Though based on a rather simple microscopic model, our DDFT simulations correctly predict a phase diagram with intriguing complexity. This close match with the experimental data together with the large range of parameters covered by both experiments and simulations, make us believe that we have identified the relevant physical parameters and the mechanisms governing structure formation in the films cylinder forming block copolymers. In particular, the large parameter space covered allows us to distinguish the effects of the two constraints being simultaneously present in a thin film situation: the surface field and the film thickness. Our results also reveal the mechanism of how both interplay.

We identified the deviations from the bulk structure, both in the vicinity of surfaces and in thin films of cylinderforming block copolymers as surface reconstructions. Together with what is known for lamella-forming systems our results give evidence for a general mechanism governing the phase behavior in thin films of modulated phases: The strength of the surface field and the deformability of the bulk structure determines how the system rearranges in the vicinity of the surface. This causes either an orientation of the bulk structure or the formation of surface reconstructions. The stability regions of the different phases are modulated by the film thickness via interference and confinement effects.

This concept along with the presented method might provide the means to understand and eventually control a wealth of thin film structures in a wide class of ordered fluids, such as linear and star multiblock copolymers as well as surfactant based fluids.

ACKNOWLEDGMENTS

We thank G. Krausch, A. Knoll, and M. Hund for discussions and help. We acknowledge support from the Deutsche Forschungsgemeinschaft (SFB 481), the Volkswagen- Stiftung, and the NWO-DFG bilateral program.

REFERENCES

1. I. W. Hamley *The physics of block copolymers* (Oxford Univ. Press, Oxford, 1998).
2. F. S. Bates and G. H. Fredrickson, *Annu. Rev. Phys. Chem.* **41**, 525 (1990).
3. S. H. Anastasiadis *et al.*, *Phys. Rev. Lett.* **62**, 1852 (1989).
4. D. G. Walton, G. J. Kellog, A. M. Mayes, P. Lambooy, and T. P. Russell, *Macromolecules*, **27**(21), 6225 (1994).
5. G. J. Kellogg, D. G. Walton, A. M. Mayes, P. Lambooy, T. P. Russell, P. D. Gallagher, and S. K. Satija, *Phys. Rev. Lett.* **76**(14), 2503–2506 (1996).
6. N. Rehse, A. Knoll, M. Konrad, R. Magerle, and G. Krausch, *Phys. Rev. Lett.* **87**, 035505 (2001).
7. M. W. Matsen, *Curr. Opin. in Coll. Interf. Sci.* **3**, 40 (1998).
8. K. Binder, *Adv. Polym. Sci.* **138**, 1 (1999).
9. M. J. Fasolka and A. M. Mayes, *Ann. Rev. Mat. Res.* **31**, 323 (2001).
10. C. S. Henkee, E. L. Thomas, and L. J. Fetters, *Journal of Materials Science* **23**(5), 1685–1694 (1988).
11. M. A. van Dijk and R. van den Berg, *Macromolecules* **28**, 6773 (1995).
12. P. Mansky, P. Chaikin, and E. L. Thomas, *J. Mater. Sci.* **30**, 1987 (1995).
13. G. Kim and M. Libera, *Macromolecules* **31**, 2569 (1998); **31**, 2670 (1998).
14. A. Karim *et al.*, *J. Chem. Phys.* **100**, 1620 (1994).
15. L. H. Radzilowski, B. L. Carvalho, and E. L. Thomas, *J. Polym. Sci., Part B: Polym. Phys.*, **34**, 3081 (1996).
16. M. Konrad, A. Knoll, R. Magerle, and G. Krausch, *Macromolecules* **33**, 5518 (2000).
17. Ch. Harrison *et al.*, *Macromolecules* **31**, 2185 (1998); *Polymer* **30**, 2733 (1998).
18. Q. Zhang *et al.*, *Macromolecules* **33**, 9561 (2000).
19. M. S. Turner, M. Rubinstein, and C. M. Marques, *Macromolecules* **27**, 4986 (1994).
20. G. Brown and A. Chakrabarti, *J. Chem. Phys.* **101**, 3310 (1994); **102**, 1440 (1995).

21. H. P. Huinink, J. C. M. Brokken-Zijp, M. A. van Dijk, and G. J. A. Sevink, *J. Chem. Phys.* **112**, 2452–2462 (2000).
22. H. P. Huinink *et al.*, *J. Chem. Phys.* **112**, 2452 (2000); *Macromolecules* **34**, 5325 (2001).
23. G. G. Pereira, *Phys. Rev. E* **63**, 061809 (2001).
24. Q. Wang, P. F. Nealy, and J. J. de Pablo, *Macromolecules* **34**, 3458 (2001).
25. J. Feng, H. Liu, and Y. Hu, *Macromol. Theory Simul.* **11**, 556–565 (2002); J. Feng and E. Ruckenstein, *Polymer* **43**, 5775 (2002).
26. G. Szamel and M. Mueller, *J. Chem. Phys.* **118**, 905–913 (2003).
27. A. Knoll, A. Horvat, K. S. Lyakhova, G. Krausch, G. J. A. Sevink, A. V. Zvelindovsky, and R. Magerle, *Phys. Rev. Lett.* **89**, 035501/1–4 (2002).
28. R. J. Spontak, M. C. Williams, and D. A. Agard, *Polymer* **29**, 387 (1988).
29. R. Magerle, *Phys. Rev. Lett.* **85**, 2749 (2000).
30. A. Knoll, R. Magerle, and G. Krausch, *J. Chem. Phys.* **120**, 1105–1116 (2004).
31. J. G. E. M. Fraaije, *J. Chem. Phys.* **99**, 9202 (1993).
32. J. G. E. M. Fraaije, B. A. C. van Vlimmeren, N. M. Maurits, M. Postma, O. A. Evers, C. Hoffmann, P. Altevogt, and G. Goldbeck-Wood, *J. Chem. Phys.* **106**, 4260 (1997);
33. G. J. A. Sevink, A. V. Zvelindovsky, B. A. C. van Vlimmeren, N. M. Maurits, and J. G. E. M. Fraaije, *J. Chem. Phys.* **110**, 2250 (1999).
34. Available from Accelrys Inc., San Diego, CA.
35. G. H. Fredrickson, V. Ganesan, and F. Drolet, *Macromolecules* **35**, 16 (2002).
36. M. W. Matsen and R. B. Thompson, *J. Chem. Phys.* **111**, 7139 (1999)
37. A structured wetting layer similar to the one shown in Fig. 11 (a) (half-cylinders) was found theoretically for diblock copolymer thin films by Wang *et al.* (Ref. 24) and by Pereira (Ref. 23).
38. B. L. Carvalho and E. L. Thomas, *Phys. Rev. Lett.* **73**, 3321 (1994).
39. M. J. Fasolka *et al.*, *Macromolecules* **33**, 5702 (2000).

5 Phase behavior in thin films of cylinder-forming *ABA* block copolymers

Knoll A., Horvat A., Lyakhova K. S., Krausch G., Sevink G. J. A., Zvelindovsky A. V. and Magerle R.

published in **Phys.Rev.Lett.**, 2002, 89, 035501/1–4.

We have experimentally determined a phase diagram for cylinder-forming polystyrene-*block*-polybutadien-*block*-polystyrene triblock copolymer in thin films. The phase behavior can be modeled in great detail by dynamic density functional theory. Deviations from the bulk structure, such as wetting layer, perforated lamella, and lamella, are identified as surface reconstructions. Their stability regions are determined by an interplay between surface fields and confinement effects.

Ordered fluids are a fascinating class of materials as they combine crystal-like order on mesoscopic length scales with liquidlike disorder on microscopic scales. As a typical example, amphiphilic block copolymers tend to self-assemble into ordered microstructures with characteristic lengths determined by the molecular size, i.e., in the 10–100 nm range.¹ The microdomain structure in the bulk is determined mainly by the molecular architecture, in particular the ratio of block lengths and the interaction between the two components (blocks). At interfaces and in thin films an additional driving force for structure formation exists, because one component typically has a lower interfacial energy than the other. This phenomenon belongs to a class of *interfaces of modulated phases*.^{2,3} Related phenomena of two-component systems are wetting and surface enrichment, surface directed spinodal decomposition,⁴ and surface-induced ordering and orientation.^{5,6} Recently, we have shown that in analogy to surface reconstructions of crystal surfaces the near-surface structure can deviate from the bulk structure in block copolymers as well.⁷ In thin films, additional constraints exist. Here, the microdomain structure has to adjust to two boundary surfaces and a certain film thickness, which can be a noninteger multiple of the "natural" bulk repetition length. Both constraints together cause a complex and interesting phase behavior.

Based on the pioneering work by Anastasiadis *et al.*⁶ numerous studies have dealt with thin films of lamellar block copolymers and two major effects have been identified.⁸ The preferential attraction of one type of block to the surface (the surface field) causes the lamella to align parallel to the interfaces and the film form islands or holes (terraces) where the film thickness is a (half) integer multiple of the bulk lamella size.

While any cross section parallel to a lamella exhibits the same symmetry as a planar surface, the situation is more complex in the case of cylinder-forming systems. Here, a planar surface, regardless of its orientation, always breaks the symmetry of the bulk structure and the microdomain structure has to adjust. Indeed, a variety of deviations from the bulk structure have been observed near surfaces and in thin films such as a wetting layer,⁹ spherical microdomains,¹⁰ a perforated lamella,¹⁰ cylinders with necks,¹¹ and more complicated structures.^{12,13} Although various models have been developed to describe this behavior^{14–17} (for summary, see Ref. 17), modeling and experimental results agree qualitatively only in parts. It remains unclear which of the reported phenomena are specific to the particular system and/or route of film preparation and which are general behavior. As a result, no general agreement is reached about the underlying fundamentals.

In this Letter we present a unifying description of these phenomena. With experiments and computer simulations based on dynamic density functional theory (DDFT) we show that the phase behavior in thin films of cylinder-forming block copolymers is dominated by surface reconstructions. Their stability regions are determined by the surface field and the film thickness and we show how these two constraints interact.

As a model system we have chosen thin films of a cylinder-forming polystyrene-*block*-polybutadiene-*block*-polystyrene (SBS) triblock copolymer swollen in chloroform vapor. SBS was obtained from Polymer Source Inc. with molecular weights of blocks $M_{w,PS} = 14k$, $M_{w,PB} = 73k$, and $M_{w,PS} = 15k$ (PS is polystyrene, PB is polybutadiene). Thin SBS films were spun cast from toluene solution onto polished silicon substrates. In order to equilibrate (anneal) the microdomain structure, the films were exposed for 7 h to a controlled partial pressure p of chloroform vapor.¹⁸ The total pressure was 1.3 ± 0.1 atm and the temperature was kept at 25.0 ± 0.1 °C. The resulting microdomain structures were quenched via fast solvent removal. During annealing, the nonselective solvent, CHCl_3 , acts as a plasticizer, which merely induces chain mobility. Within the studied range of $\tilde{p} = p/p_S$ (p_S is the partial pressure of saturated CHCl_3 vapor at 25.0 °C) the lateral spacing between two neighboring PS cylinders, a_0 , decreases with increasing \tilde{p} from $a_0 \approx 41$ to 39 nm, similar to Ref. 19.

During vapor annealing the films form terraces with thicknesses smaller and larger than the original thickness. We have determined the step heights using TappingModeTM scanning force microscopy (TM-SFM). TM-SFM phase images were recorded along with the height images to

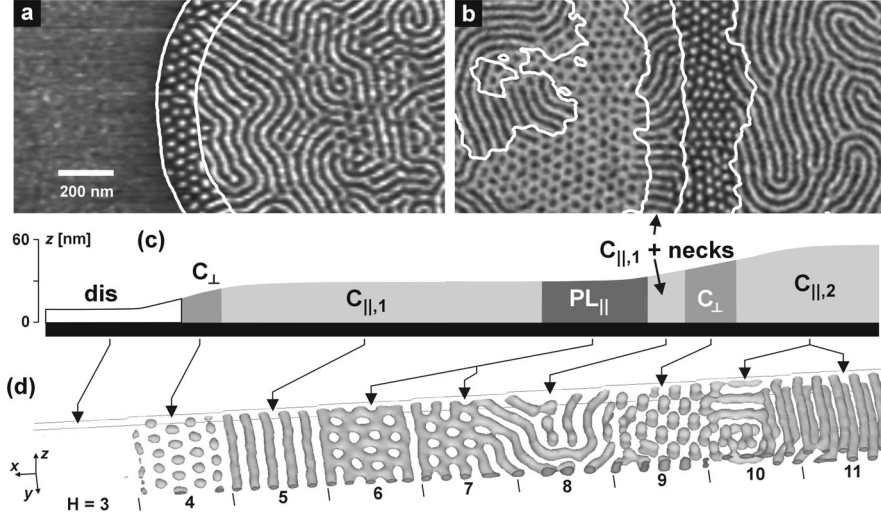


Figure 1: (a), (b) TM-SFM images of thin SBS films on Si substrates after annealing in chloroform vapor at $\tilde{p} = 0.62$. The surface is everywhere covered with an ≈ 10 -nm-thick PB layer. Bright (dark) corresponds to PS (PB) microdomains below this top PB layer.²¹ Contour lines calculated from the corresponding height images are superimposed. (c) Schematic height profile of the phase images shown in (a,b). (d) Simulation of an $A_3B_{12}A_3$ block copolymer film in **one** large simulation box of $[352 \times 32 \times H(x)]$ grid points with increasing film thickness $H(x)$, $\epsilon_{AB} = 6.5$, and $\epsilon_M = 6.0$. The latter corresponds to a preferential attraction of B beads to the surface. The isodensity surface $\rho_A = 0.5$ is shown.

map (via the difference in modulus) the lateral distribution of PS and PB near the film surface.²⁰

Figures 1(a) and 1(b) show TM-SFM phase images of two annealed SBS films with different initial film thicknesses. Both films have formed regions of well-defined film thickness as indicated by the height profile shown in Fig. 1(c). At the same time well-defined microdomain patterns have formed, which change systematically as a function of the gradually changing film thickness (at steps between terraces). In particular, boundaries between different structures correspond to height contour lines. A major fraction of the surface displays bright stripes, which are indicative of PS cylinders oriented parallel to the surface (C_{\parallel}). In thinner regions of the film two additional patterns are found: One is characterized by hexagonally ordered dark spots, indicative of PB microdomains in an otherwise continuous PS layer, i.e., a perforated PS lamella (PL). The slopes between neighboring terraces display a hexagonal pattern of bright dots, indicative of PS cylinders oriented perpendicular to the surface (C_{\perp}). Finally, the thinnest parts of the films display no lateral structure at all, indicative of either a disordered (dis) phase or a lamellar wetting layer (W). In thicker films, the sloped regions between terraces display stripes as well. Previous work has shown that the parallel orientation of PS cylinders continues through the depth of the film to the substrate.^{18,22} We note that these phases were all reported earlier

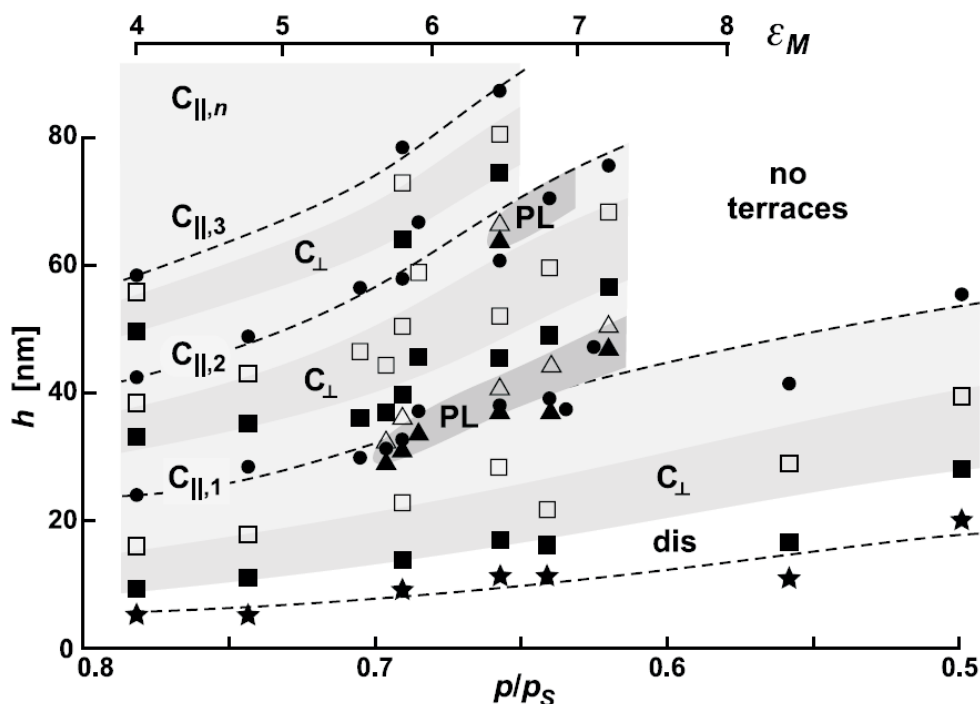


Figure 2: Phase diagram of thin SBS block copolymer films on Si substrates after annealing in chloroform vapor. Data are given for equilibrium film thicknesses of $C_{||,n}$ (circles) and dis (stars) and for upper and lower bounds (open and closed symbols, respectively) of C_{\perp} (squares) and PL (triangles) phases. The latter correspond to contour lines such as those shown in Figs. 1(a) and 1(b). All lines and areas are drawn to guide the eye.

and for various experimental conditions and cylinder-forming block copolymers. In the present experiments, however, *all* phases appear in a *single* system and under identical experimental conditions. This finding indicates that the film thickness is an important control parameter.

In order to explore the role of the strength of the surface field, the above experiment was repeated as a function of solvent vapor pressure \tilde{p} during annealing. With increasing \tilde{p} , the total polymer concentration, Φ_P , in the film decreases, which effectively reduces the interaction parameter between the two polymeric components and between the polymers and the confining surfaces. The experimental results are summarized in a phase diagram (Fig. 2) displaying the stability regions of the various phases as functions of \tilde{p} and film thickness (after drying). Note that films annealed at larger \tilde{p} shrink more in the vertical z direction upon drying than films prepared at smaller \tilde{p} .

The PL phase is predominantly observed in the lower terrace when the neighboring terrace forms the $C_{||,2}$ phase. With increasing \tilde{p} , the area fraction of the lower terrace forming a PL decreases. For $\tilde{p} = 0.64, 0.68,$ and 0.70 the area fraction is 9%, 80%, and 50%, respectively. For $\tilde{p} > 0.71$, no PL is observed. In thicker films only for $h \approx 60$ nm and $\tilde{p} = 0.66$, a small

fraction, 10%, of the terraces forms a PL.

The assignment of surface patterns to distinct phases is corroborated by DDFT simulations of the complete thin film structure. We have used the MESODYN code²³ to simulate a melt of $A_3B_{12}A_3$ molecules. Briefly, the block copolymer is modeled as a Gaussian chain with different beads A and B . For the bead-bead interaction potential a Gaussian kernel is used characterized by ε_{AB} . The film interfaces were treated as mask (M) with a corresponding bead-mask interaction parameter $\varepsilon_M = \varepsilon_{AM} - \varepsilon_{BM}$. The spatiotemporal evolution of bead densities $\rho_i(\vec{r}, t)$ is obtained using the complete free energy functional $F[\{\rho_i\}]$ and the chemical potentials $\mu_i = \delta F[\{\rho_i\}]/\delta \rho_i$. The Langevin diffusion equation is solved numerically starting from homogeneous densities. Appropriate noise is added to the dynamics. We have done simulations with $\varepsilon_{AB} = 6.3, 6.5,$ and 7.1 (in kJ/mol) and varied systematically the strength of the polymer/surface interaction ε_M and the film thickness H . We have used the parametrization of Ref. 15 and have followed the temporal evolution until significant changes no longer occurred. We chose to model the swollen SBS film as a melt to keep the total number of parameters as small as possible. The effect of the nonselective solvent CHCl_3 is modeled as an effective interaction parameter $\varepsilon_M = \varepsilon_M^{melt} \Phi_P$.

We find that modeling with $\varepsilon_{AB} = 6.5$ matches our experimental data best. Figure 1(d) shows the result of a simulation done in a wedge-shaped geometry. It exhibits exactly the same sequence of phases as the experimental data. Starting from a disordered phase (dis) for $H = 3$ grid units, spheres or very short upright cylinders, C_{\perp} , form ($H = 4$). These are followed by parallel cylinders, $C_{\parallel,1}$ ($H = 5$), a perforated lamella, PL ($H = 6$), a PL coexisting with $C_{\parallel,1}$ ($H = 7$), cylinders with ripples or necks ($H = 8$), then upright cylinders, C_{\perp} ($H = 9$), and two layers of parallel cylinders, $C_{\parallel,2}$ ($H = 10, 11,$ and 12). The film thickness at which phase transitions occur as well as the relative domain spacings are correctly predicted. The distance between next-nearest holes of the PL is found to be 1.15 times larger than the distance between next-nearest cylinders, $a_0 = 7.0 \pm 0.5$ grid units, of the C_{\parallel} and the C_{\perp} phase. We also observe this in our experiments [Fig. 1(b)].

For a systematic study of the influence of ε_M and H on the thin film structure we have done simulations in smaller boxes with $[32 \times 32 \times (H + 1)]$ grid points and a mask in the $z = 0$ plane. The structures found for $\varepsilon_{AB} = 6.5$ are summarized in a phase diagram shown in Fig. 3. The middle part of the phase diagram resembles the one reported for A_3B_6 diblock copolymers¹⁵ but covers a much larger parameter space.

The simulation results match nicely the experimental phase diagram shown in Fig. 2. For a quantitative comparison of the two phase diagrams, one has to take into account that the film thickness relevant for structure formation is the thickness in the swollen state. Furthermore, we need to relate the vapor pressure, \tilde{p} , to the effective interaction parameter between the polymer

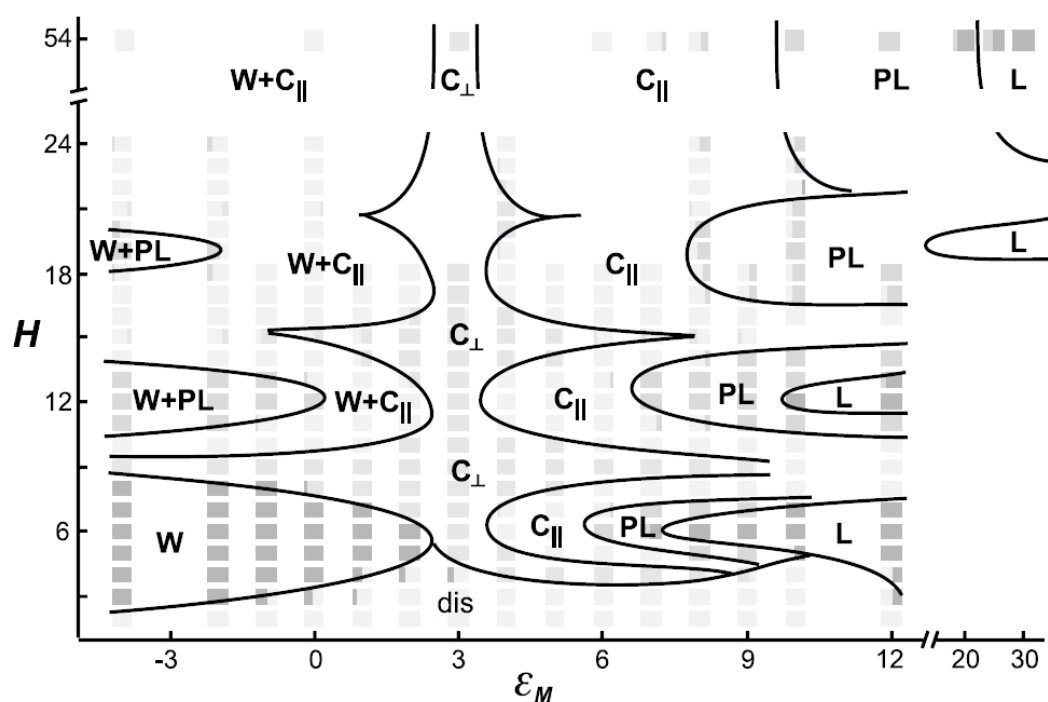


Figure 3: Phase diagram of surface reconstructions of a $A_3B_{12}A_3$ block copolymer film calculated with MESODYN for $\epsilon_{AB} = 6.5$. The boxes indicate where simulations have been done. The boxes with two shades of grey indicate that two phases coexist after the finite simulation time. Smooth phase boundaries have been drawn to guide the eye.

blocks and the confining surface, ε_M . We assume that $\varepsilon_M = \varepsilon_M^{melt} \Phi_P$, where Φ_P can be estimated from the amount of shrinkage during drying: $\Phi_P = h^{dry}/h^{wet}$. The thickness after drying, h^{dry} , has been measured, whereas h^{wet} has been calculated from the film structure assuming an ideal hexagonal structure: $h_{C_{\parallel,2}}^{wet} = a_0\sqrt{3}$ for $C_{\parallel,2}$. By choosing $\varepsilon_M^{melt} = 6.5$, the ε_M scale in Fig. 2 was adjusted such that $\tilde{p} = 0.68$ corresponds to $\varepsilon_M = 6.0$. With this simple estimate the measured and calculated phase diagrams can be perfectly matched by the adjustment of a single parameter. In particular, the predicted ε_M value for the onset of the PL phase at $H = 12$ agrees nicely with experiments.

Although based on a rather simple microscopic model, the DDFT simulations correctly predict a phase diagram with intriguing complexity. The large parameter space covered in both simulations and experiments allows us to distinguish the effects of the two constraints being simultaneously present in a thin film situation: the surface field and the film thickness. Our results also reveal the mechanism which shows how both interplay.

Surface fields. The effect of a single surface is best seen at a large film thickness ($H = 54$). The simulations show that the preferential attraction of one type of block to the surface (the surface field) is sufficient to induce considerable rearrangements of microdomains near the surface, i.e., surface reconstructions. In the middle of the simulation box, cylinders form in all cases. Moving in Fig. 3 from left to right the following surface reconstructions occur for $H = 54$. For $\varepsilon_M \leq 2$, A-beads are effectively attracted to the surface and a thin A-wetting layer (W) forms (which might also be viewed as a half lamella). At $\varepsilon_M \approx 3$, cylinders orient perpendicular to the surface (C_{\perp}). For $\varepsilon_M \approx 4 - 8$, A-beads are weakly repelled from the surface, and cylinders align parallel to the surface (C_{\parallel}). As ε_M is further increased surface reconstructions with noncylindrical microdomains are induced; first a PL, then a lamella (L). In these structures the averaged mean curvature is gradually decreased in order to adopt to the planar symmetry of the surface.

Interference of surface fields. Our results indicate that surface fields extend into the bulk with a decay length of about one microdomain spacing. Furthermore, they are additive, and for very thin films the effect of both surfaces combines. This explains why, in thin films, a weaker surface field is sufficient to form a PL (or L) than in thick films. It also explains the formation of a PL beneath a wetting layer (W + PL).

Confinement effects modulate the stability regions of phases oriented parallel to the surfaces. An integer multiple of a natural layer thickness is energetically favored. This causes easier deformable phases to occur at intermediate film thicknesses. For very small thicknesses ($H \leq$ microdomain size) and weak surface fields, confinement prevents microphase separation and stabilizes a disordered phase (dis).

We note that the orientation behavior of the cylinders is analogous to the phase behavior of lamella-forming diblock copolymers as both are controlled by the interplay between the surface

field and confinement effects.²⁴ Thus, the sequence $C_{\parallel} \rightarrow C_{\perp} \rightarrow C_{\parallel}$ at steps between terraces corresponds to the sequence $L_{\parallel} \rightarrow L_{\perp} \rightarrow L_{\parallel}$.²⁵ Also, in cases where the two confining surfaces favor different orientations (L_{\parallel} , L_{\perp}), the two orientations can coexist and a hybrid (or mixed) structure (HY) forms²⁶ which is similar to cylinders with necks.¹¹ We note that in such a HY structure, the bulk microdomain structure is preserved and a grain boundary is stabilized in the thin film by the antisymmetric surface field. Furthermore, a disordered phase has been reported for ultrathin films of lamella-forming diblock copolymers²⁶ and is in good agreement with our findings. In addition to the alignment effect, hexagonally ordered cylinders can adopt to the planar surface by formation of surface reconstructions (W, PL, L) which also dominate the phase behavior in thin films.

In conclusion, we have identified the deviations from the bulk structure, both in the vicinity of surfaces and in thin films of cylinder-forming block copolymers as surface reconstructions. Together with what is known for lamellaforming systems our results give evidence of a general mechanism governing the phase behavior in thin films of modulated phases: The interplay between the strength of the surface field and the deformability of the bulk structure determines how the system rearranges in the vicinity of the surface. This causes either an orientation of the bulk structure or the formation of surface reconstructions. The stability regions of the different phases are modulated by the film thickness via interference and confinement effects.

This concept along with the presented methods might provide the means to understand and eventually control a wealth of thin film structures in a wide class of ordered fluids, such as linear and star multiblock copolymers as well as surfactant-based fluids.

ACKNOWLEDGMENTS

We thank M. Hund, J. G. E. M. Fraaije, R. A. Segalman, and H. Hänsel for help and discussions, and acknowledge support from the Deutsche Forschungsgemeinschaft (SFB 481) and the NWO-DFG bilateral program.

REFERENCES

1. F. S. Bates and G. H. Fredrickson, *Annu. Rev. Phys. Chem.* **41**, 525 (1990); I.W. Hamley, *The Physics of Block Copolymers* (Oxford University Press, Oxford, 1998).
2. M. Seul and D. Andelman, *Science* **267**, 476 (1995).
3. R. R. Netz, D. Andelman, and M. Schick, *Phys. Rev. Lett.* **79**, 1058 (1997).
4. R. A. L. Jones *et al.*, *Phys. Rev. Lett.* **66**, 1326 (1991).
5. G. F. Fredrickson, *Macromolecules* **20**, 2035 (1987).

6. S. H. Anastasiadis *et al.*, Phys. Rev. Lett. **62**, 1852 (1989).
7. N. Rehse *et al.*, Phys. Rev. Lett. **87**, 035505 (2001).
8. For reviews, see, M.W. Matsen, Curr. Opin. Colloid Interface Sci. **3**, 40 (1998); K. Binder, Adv. Polym. Sci. **138**, 1 (1999); M. J. Fasolka and A. M. Mayes, Annu. Rev. Mater. Res. **31**, 323 (2001).
9. A. Karim *et al.*, J. Chem. Phys. **100**, 1620 (1994).
10. L. H. Radzilowski, B. L. Carvalho, and E. L. Thomas, J. Polym. Sci. Part B Polym. Phys. **34**, 3081 (1996).
11. M. Konrad *et al.*, Macromolecules **33**, 5518 (2000).
12. Ch. Harrison *et al.*, Macromolecules **31**, 2185 (1998); Polymer **30**, 2733 (1998).
13. Q. Zhang *et al.*, Macromolecules **33**, 9561 (2000).
14. M. S. Turner, M. Rubinstein, and C. M. Marques, Macromolecules **27**, 4986 (1994).
15. H. P. Huinink *et al.*, J. Chem. Phys. **112**, 2452 (2000); Macromolecules **34**, 5325 (2001).
16. G. G. Pereira, Phys. Rev. E **63**, 061809 (2001).
17. Q. Wang, P. F. Nealy, and J. J. de Pablo, Macromolecules **34**, 3458 (2001).
18. G. Kim and M. Libera, Macromolecules **31**, 2569 (1998); **31**, 2670 (1998).
19. T. Hashimoto, M. Shobayama, and H. Kawai, Macromolecules **16**, 1093 (1983).
20. S. N. Magonov *et al.*, Surf. Sci. **389**, 201 (1997).
21. A. Knoll, R. Magerle, and G. Krausch, Macromolecules **34**, 4159 (2001).
22. R. Magerle, Phys. Rev. Lett. **85**, 2749 (2000).
23. J. G. E. M. Fraaije, J. Chem. Phys. **99**, 9202 (1993); J. G. E. M. Fraaije *et al.*, *ibid.* **106**, 4260 (1997); G. J. A. Sevink *et al.*, *ibid.* **110**, 2250 (1999).
24. D. G. Walton *et al.*, Macromolecules **27**, 6225 (1994); G. J. Kellogg *et al.*, Phys. Rev. Lett. **76**, 2503 (1996).
25. B. L. Carvalho and E. L. Thomas, Phys. Rev. Lett. **73**, 3321 (1994).
26. M. J. Fasolka *et al.*, Macromolecules **33**, 5702 (2000).

6 Specific features of defect structure and dynamics in cylinder phase of block copolymers

Horvat A., Sevink G. J. A., Zvelindovsky A. V., Krekhov A. and Tsarkova L.
published in **ACS Nano** 2008, 2, 1143–1152.

We present a systematic study of defects in thin films of cylinder-forming block copolymers upon long-term thermal or solvent annealing. In particular, we consider in detail the peculiarities of both classical and specific topological defects, and conclude that there is a strong defect structure-chain mobility relationship in block copolymers. In the systems studied, representative defect configurations provide connectivity of the minority phase in the form of dislocations with a closed cylinder end or classical disclinations with incorporated alternative, nonbulk structures with planar symmetry. In solvent-annealed films with enhanced chain mobility, the neck defects (bridges between parallel cylinders) were observed. This type of nonsingular defect has not been identified in block copolymer systems before. We argue that topological arguments and 2D defect representation, sufficient for lamellar systems, are not sufficient to determine the stability and mobility of defects in the cylindrical phase. In-situ scanning force microscopy measurements are compared with the simulations based on the dynamic self-consistent mean field theory. The close match between experimental measurements and simulation results suggests that the lateral defect motion is diffusion-driven. In addition, 3D simulations demonstrated that the bottom (wetting) layer is only weakly involved into the structure ordering at the free surface. Finally, the morphological evolution is considered with the focus on the motion and interaction of the representative defect configurations.

6.1 Introduction

Thin films of block copolymers have been intensively studied over the last decades to gain understanding and control of the parameters affecting the microdomains structure, orientation, and order.^{1–3} Surface fields are important external potentials which influence the equilibrium structures and the dynamics of microdomains. Substrate modification by chemical or topographic patterning is now widely used to control the selectivity and the strength of the polymer-substrate

interactions and thus to guide the morphology and its orientation as well as long-range order in nano-patterned films.^{4–7}

It is recognized that topological defects in the local microdomain structure decrease the long range periodicity and limit the technological performance of block copolymer materials. The generation and annihilation of topological defects are the elementary processes by which long range order evolves in microdomains under the influence of thermal energy^{8,9} and application of external fields.^{10,11} Therefore, defect analysis is important for establishing the transport mechanisms in nanostructured soft materials.

Several theoretical approaches have been developed to describe 2D defect configurations,^{12,13} their interfacial properties,^{14,15} and their role in microdomain reorientation.¹⁶ In experiments, detailed information about structure and dynamics of individual defects in block copolymers is accessed by non-destructive time-resolved real-space imaging techniques, such as scanning force microscopy (SFM). The seminal work by Harrison et al. on defect evolution in stripped surface pattern¹⁷ and related studies,^{5,18–20} convincingly demonstrated that classical defects such as disclinations and dislocations, widely known from the solid crystals and nematic liquid crystal phases, play an important role in the ordering dynamics of block copolymers microdomains. The observations of defects in sphere-forming diblock copolymer films allowed conclusions to be drawn regarding the mechanisms of 2D crystal to hexatic transition, and on further melting *via* continuous defect generation process.^{21,22} Also, grain coarsening in hexagonally ordered dotlike structures which are composed of either of spheres^{23,24} or standing cylinders²⁵ has been analyzed in detail.

The research mentioned above focused on the similarities of defect interaction and their motion in block copolymers and thermotropic nematics or smectics. Thermo-tropic liquid crystals, however, are one-component homogeneous systems and are characterized by a nonconserved orientational order parameter. In contrast, in block copolymers the local concentration difference between two components is essentially conserved. In this respect, the microphase separated structures in block copolymers are anticipated to have close similarities with lyotropic systems which are composed from polar medium (water) and nonpolar medium (surfactant structure). The phases of the lyotropic systems (such as lamella, cylinder or micellar phases) are determined by the surfactant concentration. Similar to lyotropic phases, the morphology in block copolymers is ascertained by the volume fraction of the components and their interaction. Therefore, in lyotropic systems and in block copolymers the dynamics and annihilation of structural defects require a change in the local concentration difference between components as well as a change in the orientational order. Consequently, if single defect transformations could be monitored in real time and space, block copolymers could be considered as suitable model systems for studying transport mechanisms and phase transitions in two-dimensional

fluid materials such as membranes,^{26,27} lyotropic liquid crystals,²⁸ and microemulsions.²⁹

In this work, we observe structural defects and their short- to long-term dynamics in block copolymer films using SFM, including *in-situ* measurements at elevated temperatures with high temporal resolution, and we compare the experimental findings to simulations based on the dynamic self-consistent mean field theory (DSCFT). In the experiments we used polystyrene-*block*-polybutadiene copolymer, designated here as SB and composed from the polystyrene (PS) and polybutadiene (PB) blocks. In simulations, the molecular model is an $A_3B_{12}A_3$ Gaussian chain with A and B corresponding to the PS and to the PB components, respectively. We focus on specific defects in the cylinder phase which are kinetically trapped in thermal equilibrium during the lateral ordering of lying microdomains. The strength of our approach is that 2D structures and defects visualized with SFM are directly compared with computational simulations which give access to the bulk structure in the interior of the film. We distinguish between classical, modified, specific, and grain boundary defect configurations. For each defect type, we address its relative stability, interaction with the other defect types, and its role in the overall structure development.

With this approach, we discovered the strong correlation between defect structure and chain mobility, a feature which is specific to block copolymer materials due to the covalent bonding between the blocks and their large molecular weight and a feature which is not common in nematic thermotropic and lyotropic liquid crystals. The interconnectivity of the polymer chains is then manifested in the lateral propagation of a complex 3T-junction-defect, which has been captured both by *in-situ* SFM measurements and by DSCFT simulations. Finally, we discuss the lateral migration of complex and specific structural defects which are involved in the coarsening of surface patterns.

6.2 Results and Discussion

6.2.1 Phase Behavior in Thin Films.

As indicated in Figure 1 the bulk structure of SB diblock copolymer resides well in the cylinder regime within the mean-field-calculated phase diagram.³⁰ However, it is well established that confinement and surface fields effects in thin films of cylinder-forming block copolymers can cause the microdomains to deviate from the corresponding structure in bulk.³¹ Simulated images in Figure 1 are examples of surface structures³² which are also identified experimentally in thin films of cylinder-forming di- and triblock copolymers. In particular, the nonbulk perforated lamella (PL) and lamella (L) phases were reported for this type of block copolymers under strong surface fields or thickness constraints.^{30,31,33,34} The PL structure can be viewed as

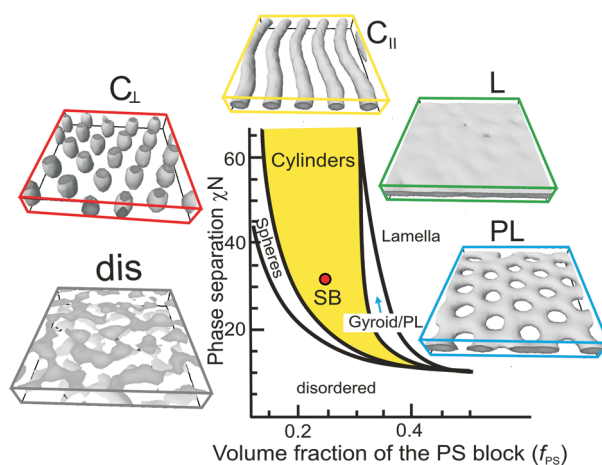


Figure 1: Schematically represented phase diagram of AB diblock copolymer melt.³⁰ SB-Labeled point indicates the parameters of the SB block copolymer under the experimental conditions reported in this study. The DSCFT simulations illustrate surface structures that are predicted theoretically and observed experimentally in thin films of cylinder-forming block copolymers under surface fields or thickness constraints: disordered phase (dis), vertically oriented cylinders (C_{\perp}), cylinders aligned parallel to the film plane (C_{\parallel}), lamella (L), and hexagonally perforated lamella (PL) phases.

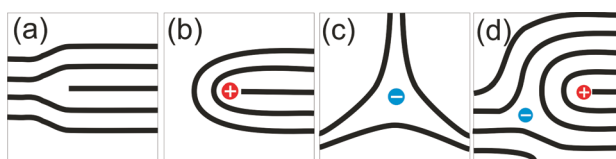


Figure 2: Schematic representation of classical topological defect configurations: (a) edge dislocation; (b) $+1/2$ disclination; (c) $-1/2$ disclination; and (d) paired $\pm 1/2$ disclinations.

alternative layers of block copolymer components with hexagonally ordered perforations in the minority phase and is tentatively similar to mesh-like liquid crystalline phase. Since to the best of our knowledge the gyroid phase has not yet been reported for thin films of diblock copolymers and of two-component triblock copolymers, the PL phase in the above systems presumably represents a 2D analogue of the bicontinuous gyroid structure.

6.2.2 Classification of Characteristic Defects.

Classical Defects. The theory and classification of defects are well-developed for certain types of materials such as solid crystals, nematic liquid crystals, and superfluids.^{35,36} In general, a topological defect is characterized by a core region (point, line, or wall) where the order parameter is destroyed and a far field region where it relaxes slowly in space. The most common topological defects in block copolymers are generally analogous to that in liquid crystals, so the

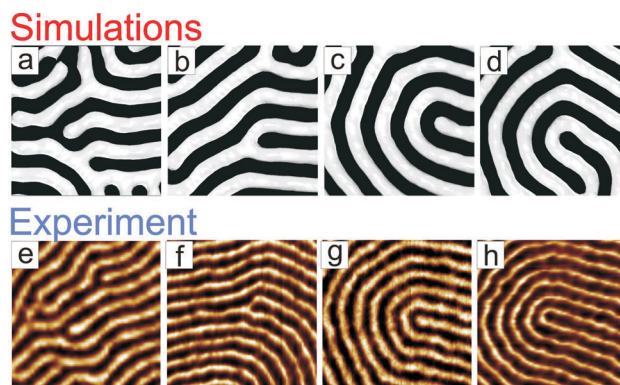


Figure 3: *Simulated images (top panel) and SFM phase images ($300\text{ nm} \times 300\text{ nm}$) presenting classical topological defect configurations in lying cylinders: (a,e) cyl-dislocation; (b,f) m-dislocation (see definition in text); (c,d) $+1/2$ cyl-disclination and (g,h) $-1/2$ m-disclination. SB films have been annealed under 70% of the saturated vapor pressure of chloroform. Here and in the following simulated/experimental images white stripes correspond to the A minority phase/PS cylinders; dark stripes correspond to B majority phase/PB matrix.*

nomenclature classifying them is similar.³⁵

Figure 2 displays sketches of classical topological defects which are common to different types of materials including block copolymers: an edge dislocation (a), $+1/2$ disclination (b), $-1/2$ disclination (c) and a pair of oppositely charged disclinations (d). Such defects have been considered in the earlier studies on microdomain ordering in cylinder- and lamella-forming block copolymers.^{17–19}

Figure 3 presents examples of simulated (top panel) and measured classical defects in triblock and diblock copolymers, respectively. In these pictures as well as in the following SFM and simulated 2D images, the white color corresponds to PS cylinders (minority phase). In a two-component system, topological defects can be formed by each phase. Images a,e and b,f in Figure 3 display edge dislocations which are formed by white and dark compartments, respectively. These defect configurations are topologically identical. Similarly, shown in Figure 3c,g, $+1/2$ disclination can be transformed into $+1/2$ disclination in Figure 3d,h by color inversion. Purely topological arguments are sufficient to describe defects in films with upstanding lamella; here a topological defect always implies the abruptness of one component. In contrast, in cylinder phase the majority dark-colored matrix (PB phase) is always interconnected, while the 2D representation of topological defects conceals this important property.

To account for the real 3D structure of cylindrical microdomains, we denote the configurations in Figure 2a,e and c,g as cylinder-phase defects (cyl-dislocation and $+1/2$ cyl-disclination), and the configurations in Figure 2b,f and d,h as matrix defects (m-dislocation

and m-disclination). In our systems, cyl-dislocations (Figure 2a,e) generally develop during the early stages of film annealing when the overall defect density is high. In well-equilibrated films, cyl-dislocations are less frequent as compared to m-dislocations (Figure 2b,f), a finding that is in agreement with the earlier studies.^{19,20} The reduced stability of cyl-dislocation is likely caused by the higher energy costs of an open-cylinder-end defect.

The lifetime of these defects depends on their surrounding. Edge dislocations are highly mobile defects when they interact with an oppositely charged pair, or with disclinations. Isolated dislocations, for example, in the middle of a large cylinder grain, are harder to annihilate. Their relative immobility is attributed to the high energy costs to restructure the ordered surrounding. The same energetic arguments account for the trapping of $+1/2$ disclinations of both types (Figure 3c,d) in well-ordered samples.

The motion of cyl- or m-dislocations perpendicular to the cylinder axis involves the consecutive opening and relinking of a cylinder connection. These elementary steps of dislocation dynamics have been recently accessed with *in-situ* SFM imaging.³⁷ The estimated typical time for the rejoining of a dislocation was ≈ 10 s. The related activation energy ≈ 30 J/mol is several orders of magnitude lower compared to the value obtained by SFM snap-shot experiments.¹⁹ Importantly, m-dislocations (Figure 3b,f) can propagate along the cylinder axis without diffusion across the PS-PB interface.³⁷

Modified Classical Defects. The rich phase behavior of cylinder-forming block copolymers is reflected in the modification of classical defects by incorporation of elements of nonbulk structures. Defects in Figure 4a,d are tentatively attributed to $+1/2$ disclination with an incorporated PL ring. In this kind of defect, the PL cell often has a distorted shape and somewhat large dimensions compared to a hexagonally ordered PL unit site. It is typically isolated from other PL-like defect sites and appears to be position-trapped. The defect in Figure 4b,e can be obtained by phase inversion in the previously described $+1/2$ disclination and is therefore topologically equivalent to the above defect. However, the white dot in the middle (Figure 4b,e) can be attributed to vertically oriented cylinders, spheres, or cylinders with upstanding necks. Such defects are typically formed at early stages of structure equilibration; they stick to their original position and annihilate rather slowly due to missing lateral connectivity in the minority phase.

Figure 4c,f displays another example of a representative specific defect. This configuration is identified as a modified classical $-1/2$ disclinations with incorporated PL structure. Such defects are typically paired with $+1/2$ disclinations and are trapped at *three*-cylinder-grain junctions. The PL structure lacks the axial symmetry; therefore it effectively compensates large disorientations of cylinder grains. Additionally, the appearance of the nonbulk PL phase as a defect component in the cylinder phase can be justified by low interfacial tension between these phases.³⁸ Since the dimensions of the hexagonally ordered PL and cylinder phases are compat-

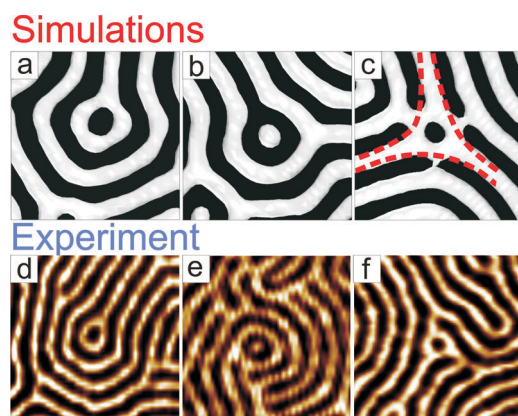


Figure 4: Simulated images (top panel) and SFM phase images (300 nm times 300 nm) presenting specific defect configurations: $+1/2$ disclination (a,d) and $-1/2$ disclination (c,f) with incorporated PL fragment; (b,e) $+1/2$ dot-disclination. SB films have been annealed under 50% of the saturated vapor pressure of chloroform.

ible, the excess of the chain stretching/confinements at defect cylinder sites is released by the local phase transition.

The modified $-1/2$ disclination can contain PL clusters of varied size (Figure 5). Generally, the size and the lifetime of the PL-defects depend on the particular experimental conditions. On one hand, they can be considered as a metastable transient phase which enhances the connectivity of the minority component as compared to the cylinder phase, and therefore facilitates the annihilation of defects. The lifetime of such temporal phases with a cluster size of $\approx 1 - 10$ PL rings ranges from minutes to hours.³⁹ On the other hand, these ring-like PL-defects may appear as nuclei of a stable PL grain when a small thickness gradient promotes coexistence of PL/ C_{\parallel} phases (Figures 5c,f and 11).^{32,34}

Another example of a frequently observed position-trapped configuration denoted as the horseshoe defect is presented in Figure 6. This defect can be viewed as a core region of $+1/2$ disclination next to a PL cluster. It is as well observed in DSCFT simulations which in some instances reveal the connection of this defect to the bottom layer of microdomains (Figure 6c). The annihilation of such defects through the formation of a transient nonbulk lamella phase was captured by *in-situ* SFM (Figure 6d).³⁷ The horseshoe defect is highly incompatible with ordered in-plane structures, and the local transition to lamella phase provides higher in-plane chain mobility as compared to that in the cylinder phase.

Specific Defects. Figure 7 presents a specific neck defect which, to our knowledge, has never been identified before in block copolymer films. This bridge-like connection between neighboring parallel cylinders can be viewed as a closely interacting pair of m-dislocations (Figure 7a and related sketch). Such necks provide connectivity of the minority phase and

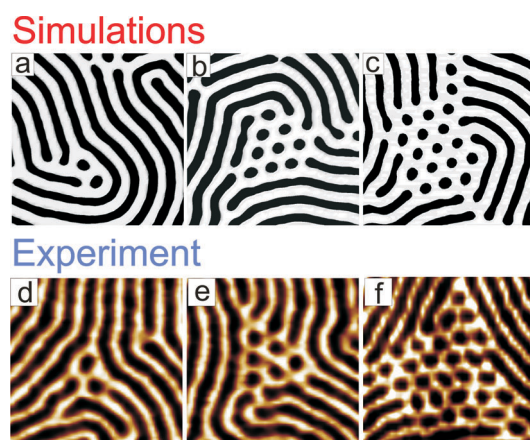


Figure 5: *Simulated images (top panel) and SFM phase images (300 nm times 300 nm) depicting specific configurations of - 1/2 disclinations with different PL - cluster size. SB films have been annealed under 50% of the saturated vapor pressure of chloroform.*

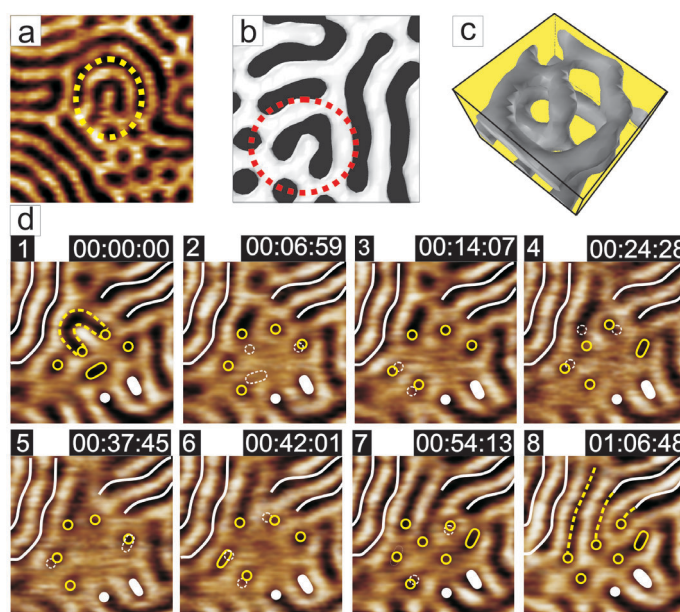


Figure 6: *SFM phase image (a) (300 nm \times 300 nm) and simulated images (b,c) presenting the horseshoe defect. (d) Selected SFM phase images (250 nm \times 250 nm) from the consecutively saved sequence illustrating the annihilation of a horseshoe defect (marked by dashed lines in frame 1). Solid white lines and filled symbols mark lattice sites which remain unchanged during the transformation. Empty symbols indicate lattice sites at the boundary of the transient lamella phase. The previous position of moving lattice sites is shown by dashed symbols. In frame 8, thick dashed lines mark cylinder domains which replace the horseshoe defect (frame 1). In-situ SFM imaging has been done at 105 $^{\circ}$ C.*

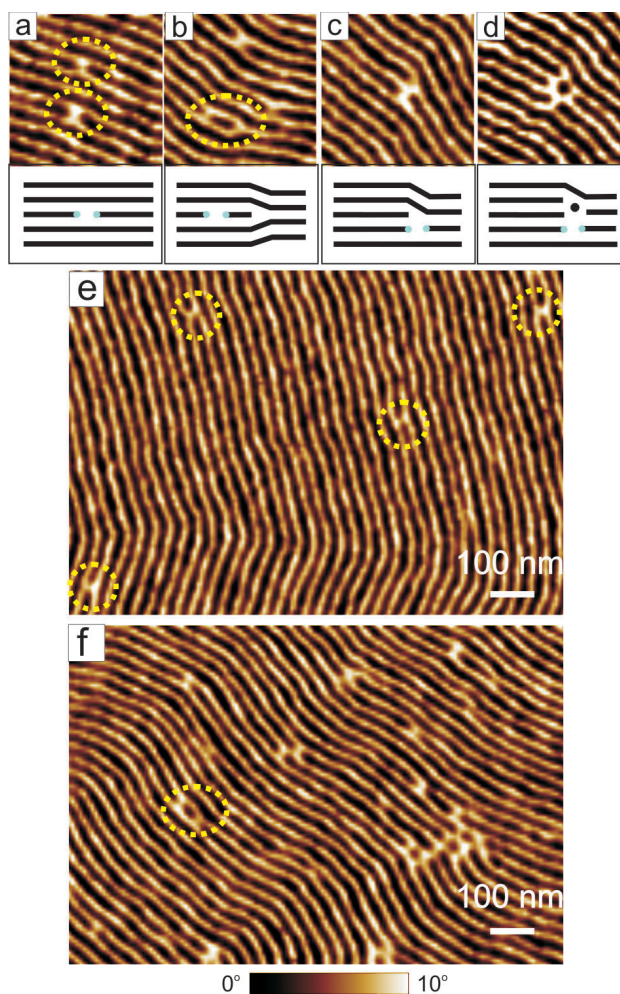


Figure 7: *SFM phase images of surface structures in SB films, which were equilibrated under 70% of the chloroform-saturated atmosphere, showing specific neck defects (a,e) (highlighted by white (yellow) circles); interaction of neck-defects with m -dislocations (b,c), and with a single PL ring (d). Image f indicates the elementary steps of the lateral defect motion and interaction.*

thereby facilitate material transport without crossing the PS-PB interface. Since the annihilation of a neck-defect does not require a discontinuous change of the order parameter, it is not a singular defect. Necks are frequently observed in the ordered cylinder phase under conditions which provide sufficient chain mobility (for example, in swollen SB films with the polymer volume fraction below ≈ 0.8 , Figure 7e,f). Such necks can group with m -dislocations along or across the cylinder axis (Figure 7 panels b and c, respectively) or with PL rings (Figure 7d). Interestingly, in DSCFT simulations neck defects are not seen in the ordered cylinder phase. This fact likely indicates a small energy difference between the neck defect and the defect-free cylinders. Considering the experimental conditions when the necks between cylinders form, we conclude that their origin is driven by local concentration fluctuations.

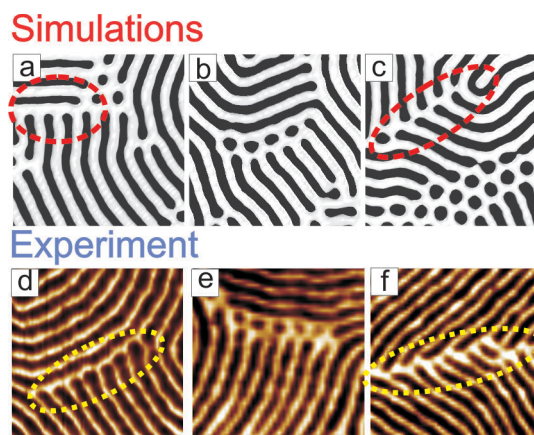


Figure 8: Simulated images (top panel) and SFM phase images ($300 \text{ nm} \times 300 \text{ nm}$) presenting grain boundaries defects: (a,d) extended T-junctions configuration; (b,e) chain of PL rings at grain boundary; (c,f) grain boundary defect between cylinder grains with a disorientation angle of $\sim 75^\circ$. SB films have been annealed under 70% (d,f) and 55% (e) of the saturated vapor pressure of chloroform.

The observed SB films neck defects are similar to those found in lyotropic liquid crystals. In particular, the important transport functions of the bridging connections in lyotropic lamella phase have been recently reported.²⁸ In this study, the abrupt increase of the diffusion coefficient across the lamella upon approaching the lamella-isotropic phase transition has been interpreted in terms of neck defects connecting the surfactant structure. Additionally, the formation of nonsingular neck defects is tentatively similar to the initial stages of the membranes/vesicles fusion.²⁶ Note that in thermotropic liquid crystals such defects are prohibited due to a nonconserved nature of the order parameter.

Grain Boundary Defects. Figure 8 presents examples of extended grain boundary defects. The T-junction defect (Figure 8a,d) is one of the most stable defect configurations and forms at large angles of disorientation ($\approx 80 - 90^\circ$) between two cylinder or lamella⁴⁰ grains. In the cylinder phase, T-junctions compensate for strong disorientation of grains and at the same time provide connectivity of PS cylinders (white stripes) between neighboring grains while the majority PB matrix (dark stripes) remains interconnected. We note that the connectivity function of a T-junction in most cases can not be realized in the lamella phase as it always abruptly terminates one component (mostly, the minority component⁴⁰). In the following, we describe the lateral mobility of such complex T-junction defects.

The extended defect in Figure 8b,e is represented by a chain of PL cells along the grain boundary and can be considered as a modified T-junction defect. Such configuration indicates the tendency of the system to undergo the cylinder-to-PL phase transition. The boundary defect in Figure 8c,f presents the case where two cylinder grains meet at a disorientation angle

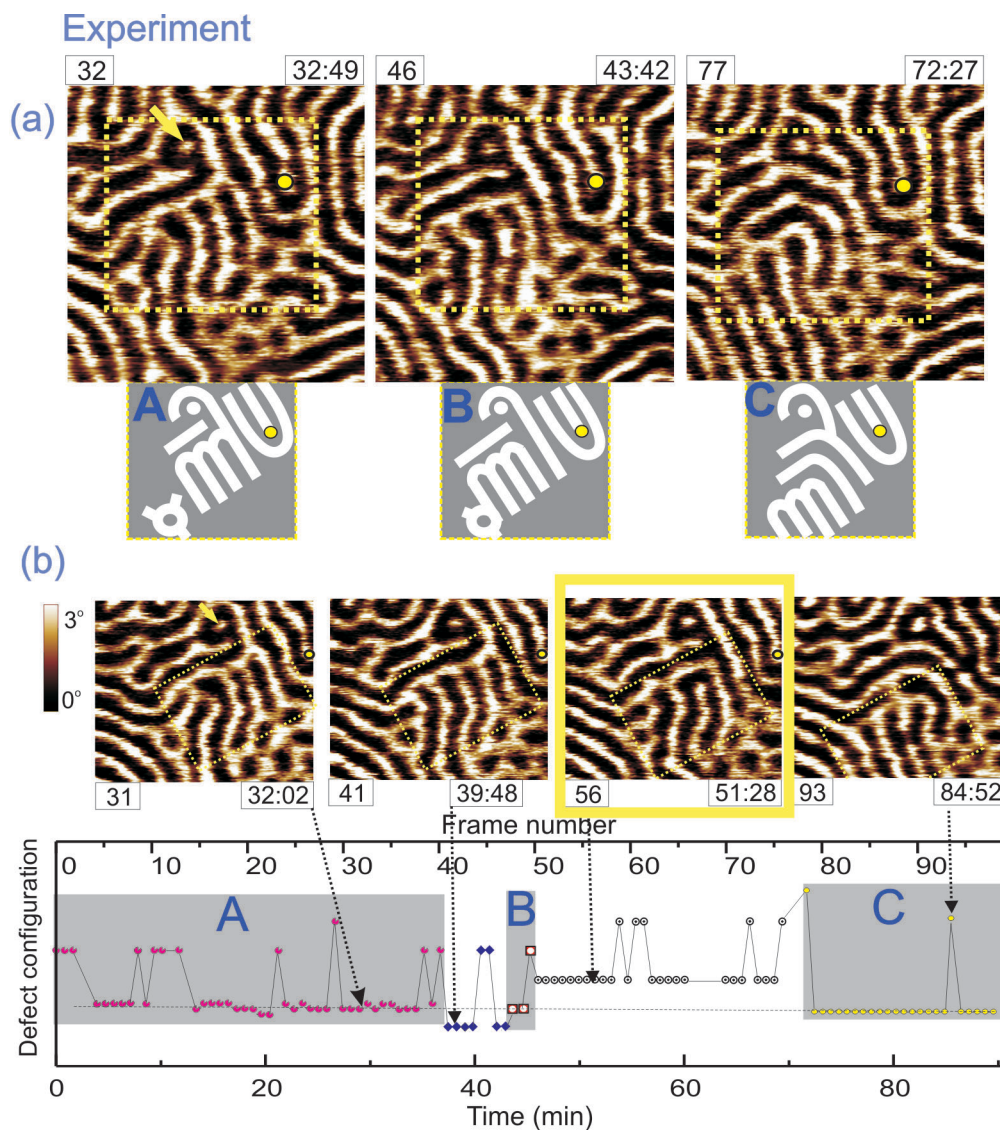


Figure 9: Dynamics of the 3T-junction defect. (a) SFM phase images from in-situ SFM movie (image size, $350 \text{ nm} \times 350 \text{ nm}$; the phase scale, 3°). Frame numbers and elapsed time of the SFM movie are indicated next to each frame. Configurations A, B, and C highlight the stages of the movement of the T-junction defect (marked with a white (yellow) square) relative to the indicated position-trapped defects. (b) Plot shows the evolution of temporal/excited configurations, which are sorted and grouped along the configuration coordinate according to the number of open ends. SFM images ($250 \text{ nm} \times 200 \text{ nm}$) in the upper panel are selected frames from SFM movie and present intermediate defect configurations.

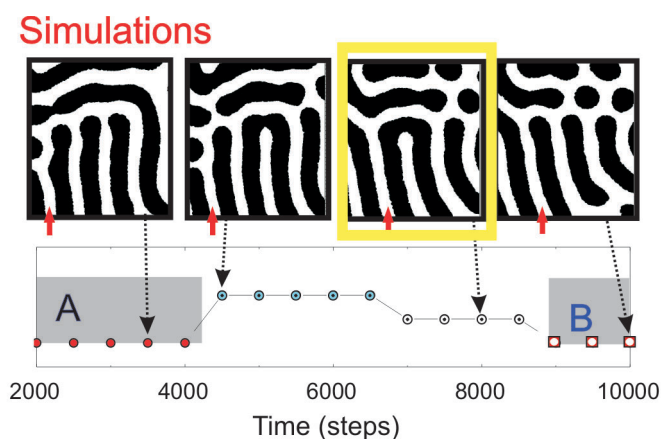


Figure 10: *Temporal evolution of the 3T-junction defect in DSCFT simulations. Data are plotted according to the same criteria as in Figure 9b. Selected frames from the simulation movie show characteristic (A and B) and intermediate stages of the 3T-junction movement. Solid arrows (red) mark the left edge of the 3T-junction upon propagation.*

of $70 - 75^\circ$. This grain boundary is characterized by considerable distortion of microdomain dimensions in the junction sites; at the same time, the connectivity of the minority PS phase between the neighboring grains is preserved. However, we note that in most cases grain boundaries with such disorientation angles are marked by a narrow region with high density of classic and specific defects described above.

6.2.3 Dynamics of Complex Defects.

Experiment. With *in-situ* SFM we followed the lateral movement of a 3T-junction defect which consists of four parallel cylinders connected to an orthogonally-oriented cylinder (Figure 9a). The SFM movie can be found as Supporting Information.⁴¹ Selected frames from this movie and the respective sketches below each image (Figure 9a) present the characteristic steps of the defect propagation. As a guide for the eye, white (yellow) dots mark the open cylinder end. The position of this $+1/2$ disclination remains stable during imaging. Another characteristic reference point is a white-dot defect which is indicated by the arrow in frame 32 of Figure 9a. In Frame 32, the 3T-junction is positioned next to the marked $+1/2$ disclination (configuration A). About 9 minutes later, the 3T-junction appears to be separated by one cylinder from the disclination (frame 46 and configuration B). Finally, in frame 77 it is separated by two cylinders from the indicated disclination, still preserving its complex structure.

The details of these transformations are captured in the SFM-movie which covers more than

70 minutes of the continuous imaging. Since we have done the measurements with high temporal resolution, we plotted in Figure 9b a temporal pathway of this defect. Here the temporal and excited defect configurations are sorted along the vertical axis according to the number of cylinder open ends. Each type of symbol indicates the presence of a certain defect configuration such as the A, B, or C type as in Figure 9a, such as the intermediate 4T-junction configuration in frame 41 (inset in Figure 9b), or a quite stable $+1/2$ disclination as in frame 56 (Figure 9b). When a configuration does not contain an open cylinder end (such as in frames 56 and 93 in Figure 9b) or a shape undulation (as the sock-like undulation in frame 31 of Figure 9b), then the symbols are placed on the horizontal dashed line. Any open cylinder end is configured as higher energy defect structure and the respective data-point is shifted up along the y-axis.

Figure 9b indicates that each of the configurations A, B, and C has a different lifetime. Configuration A was present for about 40 minutes with a short-lived break-up of the cylinder connections and shape undulations (excited configurations). The transition to configuration B was achieved via an intermediate 4T-junction defect. Configuration B was relatively short-lived, and changed quickly into a long-lived defect with $+1/2$ disclination (frame 56 in Figure 9b). The final step to configuration C proceeded with the consumption of the PL ring from the modified $-1/2$ disclination (as in Figure 4f). Configuration C appeared to be quite stable with almost no fluctuations. Importantly, in configuration C the 3T-junction now appears closer to the small PL patch (a nonbulk transient phase). Thus on a mesoscale level, the captured motion can be viewed as an elementary step towards the lateral separation of coexisting morphologies (see Figure 11).

During the captured lateral transformations, the complex 3T-junction defect has moved on a distance of two microdomain spacings ($a \approx 70$ nm) in $t \approx 70$ minutes. A simple estimation using the Einstein relation $a = (Dt)^{1/2}$ gives a diffusion constant of $D \approx 10^{-16}$ cm²/s. This result indicates that the lateral diffusion of a complex stable defect configuration is 3-4 orders of magnitude smaller compared to the self-diffusion constant determined earlier for this system.³⁷

Simulations. A lateral migration of the similar 3T-junction defect was followed with DSCFT simulations and is presented in Figure 4.10. Like in Figure 9b, defects are sorted along the Y-axis according to the number of cylinder open ends. Selected frames from the simulation movie⁴² display characteristic (A and B) and intermediate stages of the 3T-junction movement. In simulations, the defect moved on one cylinder spacing to the right relative to the initial position A. Similar to the experimental observations, the movement of the complex 3T-junction defect proceeds *via* long-living intermediate structures with $+1/2$ disclination (marked by yellow (gray) squares in Figures 9b and 10). Moreover, the movement of the defect is directed towards the developing PL phase (right image in Figure 10). From the good agreement between the simulations and the experimental observations we conclude that DSCFT on a long time scale

correctly describes defect dynamics in block copolymer films. From the above results, a single simulation step can be identified with a real experimental time of $\approx 1 - 2$ s. This value is in a good agreement with the earlier experimental and theoretical studies which are based on the comparison of the morphological phase transitions^{38,43} rather than on the analysis of the lateral defect motion.

Another important conclusion which we have derived from the dynamic simulations of a film with a wetting layer is only the weak involvement of this bottom layer in the ordering of the structures at the free surface. Slight perturbations in the volume density at the wetting layer are seen exclusively below excited defect configurations such as open-cylinder-ends (see 3D simulation movie⁴²).

Lateral Separation of Morphologies under Coexistence Conditions. Earlier theoretical and experimental studies have pointed to a relationship between the microdomain structures and transport mechanisms in block copolymer films. In particular, it is known that topological defects with open cylinder ends (such as vertically oriented cylinders, cylinders with necks, open-end dislocations) are indicative of the material transport perpendicular to the surface.^{19,43,44} Such open-end structures appear during the early stages of terrace formation,⁴³ during the directional orientation of cylinders perpendicular to the surface by external fields,^{22,45,46} and in thermal equilibrium at incompatible film thickness.³¹ Here we focus on the specific defects which are associated with the lateral ordering of lying cylinder microdomains.

In the earlier studies on the phase behavior in SB films, we established conditions in which the cylinder phase is in thermal equilibrium with the PL structures.^{34,47} At particular surface fields and segregation power, the slight thickness variation within the first layer of cylinders is reflected in the coexistence of two morphologies. Further, we noticed that the degree of the lateral separation of cylinder and PL phases essentially depends on the annealing conditions. Figure 11 presents SFM phase images of the surface structures in $\sim 1\ 1/2$ -layer thick SB films which have been annealed (a) in vacuum at elevated temperature and (b) in the atmosphere of the chloroform vapor. Both images reveal coexistence of morphologies, however with drastically differing degree of the lateral separation (different grain sizes).

Figure 11a displays coexisting PL and cylinder grains of small sizes with a high defect density in the cylinder phase. In contrast, after solvent annealing the two morphologies are well separated and exhibit a high degree of long-range order. Since in both systems the χN parameter is estimated to be ~ 35 and thus the segregation power is assumed to be similar, the difference in the degree of the structure equilibration can be attributed to the chain mobility under given annealing conditions. Obviously, the efficiency of the microdomain equilibration is higher under solvent annealing conditions. Further comparison of images in Figure 11a,b suggests that both the density of defects and their relative lifetimes depend on the chain mobility.

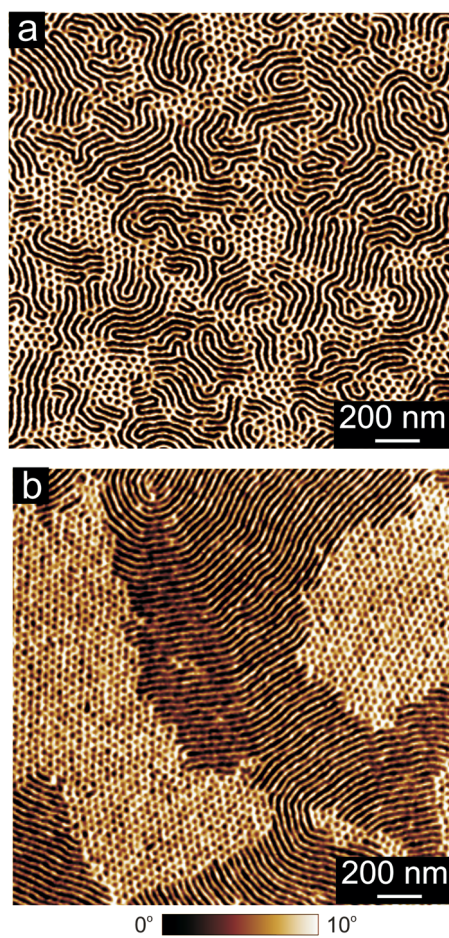


Figure 11: *SFM phase images presenting coexisting PL and cylinder morphologies in SB films annealed for 18 hours (a) in vacuum at 120 C on carbon coated silicon and (b) on silicon substrate under the atmosphere of 50% of the saturated chloroform vapor pressure.*

In thermally annealed films, all types of described above classic and modified defects (Figures 3-6 and 8) appear to be kinetically trapped. In swollen films, specific neck defects obviously dominate over other defect types which presumably have short life-times under these conditions (Figures 7e,f and 11b).

We believe that in thermally annealed films, the lateral coarsening of the PL grains proceeds predominantly through the lateral movement of PL-modified or clustered complex defect configurations such as PL-patches and T-junctions (Figures 810). In solvent-containing systems with considerable interfacial fluctuations, the neck-defects are involved in the grain coarsening at late stages of structure equilibration. It is likely that motion of neck defects, doubled necks (which are structurally similar to a single PL ring) along the cylinder axis, and their interaction with other defects or with existing grains of nonbulk phases can be considered as elementary steps of the lateral separation of morphologies in thermal coexistence (Figures 7f and 11b).

6.3 Summary

In this work, we focus on specific defects in the cylinder phase which are kinetically trapped in thermal equilibrium during the lateral ordering of lying microdomains. Using SFM measurements complemented by DSCFT simulations we show that structural defects and their interactions in cylinder-forming block copolymers can not always be described with the approaches and knowledge gained from defect studies in nematic thermotropic and lyotropic liquid crystals. In particular, the systems studied here showed a strong correlation between the defect structure and chain mobility both on short and on long-term time scales.

We have shown that purely topological arguments and 2D representation are not sufficient to elucidate the stability and mobility of defects in cylinder morphology where specific and representative classic defects provide connectivity of cylinders (of the minority component). Generally, dislocations with a closed cylinder end are more stable than configurations with an open cylinder end which are typically short-lived elementary steps of defect reconstruction. Classical $+1/2$ disclinations in the cylinder phase incorporate alternative structures, such as the nonbulk perforated lamella phase which has planar symmetry and thus a higher degree of connectivity of the minority component. Observation of nonsingular neck defects suggests similarities of transport mechanisms in block copolymers with considerable interfacial fluctuations and in other types of soft matter such as lyotropic liquid crystals and membranes.

Good agreement between the experiment and simulations on the details of the lateral propagation of a complex 3T-junction defect suggests diffusion-driven lateral transport and correlated defect motion due to the interconnectivity of the polymer chains. Additionally, simulation results show that the bottom (wetting) layer is only weakly involved in the development of the

structures at the free surface. The estimates of the motion velocity of the clustered defect configurations give insight into the molecular mechanisms of the chain transport in block copolymer materials.

The degree of lateral separation of coexisting PL and cylinder phases and related representative defects depend on the mobility of chains under given annealing conditions. Our results suggest that the chain mobility is an important factor that guides the pathways of defect annihilation and thus the transport mechanisms in block copolymer films.

6.4 Experimental Details

6.4.1 Polymer

We used polystyrene-block-polybutadiene copolymer (SB) (Polymer Source Inc.) with molecular weights of the polystyrene (PS) and polybutadiene (PB) blocks of 13.6 and 33.7 kg/mol, respectively, with a PS volume fraction of 25.5% and a polydispersity of 1.02. The glass transition temperatures of the SB components are $T_{g,PB} = -60^{\circ}\text{C}$ and $T_{g,PS} = 80 - 100^{\circ}\text{C}$. In bulk, SB forms glassy PS cylinders embedded in a soft PB matrix with a characteristic distance of 33.6 nm between the next-nearest cylinders (SAXS measurements).³⁴ SB films were prepared by spincoating a toluene solution on carbon-coated silicon wafers and further annealing either under chloroform (nearly neutral solvent) at controlled vapor pressure or at elevated temperatures in vacuum.

6.4.2 Scanning Force Microscopy

The microdomain morphology in quenched films was measured with a Dimension 3100 SFM (Veeco Instruments Inc.) operated in TappingMode using silicon tips with a spring constant of *ca.* 40 N/m, and a resonance frequency ranging from 200 to 300 kHz.

In-situ imaging was performed in the hot-stage of a MultiMode SFM (DI/Veeco Metrology Group) under a flow of dry nitrogen, with an amplitude setpoint of ~ 0.96 and a scanning frequency of 9 Hz, resulting in an acquisition time of 46 s/image. An 50 nm thick SB film on carbon coating was first annealed at 140 °C to induce terrace formation and lateral ordering of the microdomains and then quenched to 105 °C for SFM imaging. At the temperature range 105-120 °C, the combined Flory-Huggins parameter χN is about 35, which corresponds to the intermediate segregation regime.

To estimate the possible impact of the sample degradation due to the loose seal of the heating chamber, we performed separate snapshot measurements under the above temperature and nitrogen flow conditions. The first signs of the partial cross-linking of the PB component were

detected after 20 hours of annealing, which considerably exceeds the typical times of the *in-situ* measurements.

6.4.3 Simulation

Thin film behavior of a cylinder-forming block copolymer was modeled using the dynamic variant of self consistent field theory (DSCFT).⁴⁸ Earlier this method was successfully used to study equilibrium structures,^{31,32,49} dynamics of phase transitions,³⁸ and structure evolution in supported films.⁴³ Since the governing equation for structure evolution in DSCFT is a stochastic differential equation, where the stochastic term represents the thermal fluctuations, the morphology of thin film as well as the appearance and connectivity of structural defects is not predefined.

For the analysis of defects in one-layer-thick films of cylinder-forming block copolymers, we have considered three systems which phase behavior has been described in detail in earlier publications.^{32,49} Systems A and B from ref. ³² both have symmetric wetting conditions, with a film height of 7 grid units (+2 grid units for the mask) and the interaction parameter between the polymer beads $\epsilon_{AB} = 6.5$. The interaction parameters of the polymer beads with the surfaces (or with the mask) are $\epsilon_{AS} = 5$, $\epsilon_{BS} = 0$, and $\epsilon_{AS} = 6$; $\epsilon_{BS} = 0$ for systems A and B, respectively. System C from ref. ⁴⁹ has asymmetric wetting conditions, a film height of 10 grid units (+2 grid units for mask); $\epsilon_{AB} = 6.5$, and the interaction parameters of the polymer beads with the lower interface $\epsilon_{AS} = 6$, $\epsilon_{BS} = 0$, and with the upper interface $\epsilon_{AS1} = -1$, $\epsilon_{BS1} = 0$. For the present study the above systems have been simulated in large boxes with lateral sizes of 128×128 grids to exclude the influence of the boundary conditions on single defects; the examples of classical and specific defects in Figures 36, 8 are cuts (in time and position) from these simulations. For each system simulations have been done for more than 50 000 simulation steps. We note that the simulation results cannot be used for the independent statistical analysis of the representative defect configurations as even the largest simulation boxes contain not more than 20 microdomains. Here simulations are used to support experimental observations, which give access to a statistically valuable number of defect configurations.

The dynamics of a complex 3T-junction defect was followed in system C in the simulation box with lateral sizes of 64×64 grid units (Figure 10).

Acknowledgment

This work was supported by the Sonderforschungsbereich 481 (TP B7, A8) funded by the Deutsche Forschungsgemeinschaft (D.F.G.). G. Krausch and R. Magerle are gratefully acknowledged for fruitful discussions.

Supporting information available:

SFM movie: Tapping-mode scanning force microscopy movie of the surface structures in a fluid SB film at 105 C. Bright color corresponds to PS microdomains. The size of the area is $350 \times 350 \text{ nm}^2$. The frame rate is 46 s/frame, and the total imaging time is ~ 92 min. Simulational movie: Dynamic self-consistent mean-field simulations of the structure evolution in cylinder-forming block copolymer melt modeled by $A_3B_{12}A_3$ Gaussian chains. The dimensions of the simulation box are $64 \times 64 \times 12$ grid units. The displayed A-component (isodensity level $\rho_A = 0.5$) forms one structured layer on the top of wetting layer. The surface fields are set to $\epsilon_{M,1} = -1 \text{ kJ/mol}$ and $\epsilon_{M,2} = 5 \text{ kJ/mol}$. The structure dynamics is plotted every 50th time step in the simulation range from 3000 to 10000 time steps. This material is available free of charge via the Internet at <http://pubs.acs.org>.

REFERENCES AND NOTES

1. Fasolka, M. J.; Mayes, A. M. Block Copolymer Thin Films: Physics and Applications. *Annu. Rev. Mater. Res.* **2001**, *31*, 323355.
2. Segalman, R. A. Patterning with Block Copolymer Thin Films. *Mater. Sci. Eng. Res.* **2005**, *R48*, 191226.
3. Darling, S. B. Directing the Self-Assembly of Block Copolymers. *Prog. Polym. Sci.* **2007**, *32*, 11521204.
4. Stein, G. E.; Cochran, E. W.; Katsov, K.; Fredrickson, G. H.; Kramer, E. J.; Li, X.; Wang, J. Symmetry Breaking of in-Plane Order in Confined Copolymer Mesophases. *Phys. Rev. Lett.* **2007**, *98*, 158302158304.
5. Kim, S. O.; Kim, B. H.; Kim, K.; Koo, C. M.; Stoykovich, M. P.; Nealey, P. F.; Solak, H. H. Defect Structure in Thin Films of a Lamellar Block Copolymer Self-Assembled on Neutral Homogeneous and Chemically Nanopatterned Surfaces. *Macromolecules* **2006**, *39*, 54665470.
6. Sundrani, D.; Darling, S. B.; Sibener, S. J. Guiding Polymers to Perfection: Macroscopic Alignment of Nanoscale Domains. *Nano Lett.* **2004**, *4*, 273276.
7. Edwards, E. W.; Montague, M. F.; Solak, H. H.; Hawker, C. J.; Nealey, P. F. Precise Control over Molecular Dimensions of Block-Copolymer Domains Using the Interfacial Energy of Chemically Nanopatterned Substrates. *Adv. Mater.* **2004**, *16*, 13151319.

8. Corte, L.; Yamauchi, K.; Court, F.; Cloitre, M.; Hashimoto, T.; Leibler, L. Annealing and Defect Trapping in Lamellar Phases of Triblock Terpolymers. *Macromolecules* **2003**, *36*, 76957706.
9. Huang, E.; Mansky, P.; Russell, T. P.; Harrison, C.; Chaikin, P. M.; Register, R. A.; Hawker, C. J.; Mays, J. Mixed Lamellar Films: Evolution, Commensurability Effects, and Preferential Defect Formation. *Macromolecules* **2000**, *33*, 8088.
10. Amundson, K.; Helfand, E.; Quan, X.; Hudson, S. D.; Smith, S. D. Alignment of Lamellar Block Copolymer Microstructure in an Electric Field. 2. Mechanisms of Alignment. *Macromolecules* **1994**, *27*, 65596570.
11. Cohen, Y.; Thomas, E. L. Effect of Defects on the Response of a Layered Block Copolymer to Perpendicular Deformation: One-Dimensional Necking. *Macromolecules* **2003**, *36*, 52655270.
12. Fredrickson, G. H.; Ganesan, V.; Drolet, F. Field-Theoretic Computer Simulation Methods for Polymers and Complex Fluids. *Macromolecules* **2002**, *35*, 1639.
13. Bosse, A. W.; Sides, S. W.; Katsov, K.; Garcia-Cervera, C. J.; Fredrickson, G. H. Defects and Their Removal in Block Copolymer Thin Film Simulations. *J. Polym. Sci., Part B: Polym. Phys.* **2006**, *44*, 24952511.
14. Netz, R. R.; Andelman, D.; Schick, M. Interfaces of Modulated Phases. *Phys. Rev. Lett.* **1997**, *79*, 10581061.
15. Tsori, Y.; Andelman, D.; Schick, M. Defects in Lamellar Diblock Copolymers: Chevron- and W-Shaped Tilt Boundaries. *Phys. Rev. E* **2000**, *61*, 28482858.
16. Zvelindovsky, A. V.; Sevink, G. J. A. Comment on Microscopic Mechanisms of Electric-Field-Induced Alignment of Block Copolymer Microdomains. *Phys. Rev. Lett.* **2003**, *90*, 049601.
17. Harrison, C.; Adamson, D. H.; Cheng, Z.; Sebastian, J. M.; Sethuraman, S.; Huse, D. A.; Register, R. A.; Chaikin, P. M. Mechanisms of Ordering in Striped Patterns of Diblock Copolymers. *Science* **2000**, *290*, 15581561.
18. Hahm, J.; Lopes, W. A.; Jaeger, H. M.; Sibener, S. J. Defect Evolution in Ultrathin Films of Polystyrene-block-poly(methyl methacrylate) Diblock Copolymers Observed by Atomic Force Microscopy. *J. Chem. Phys.* **1998**, *109*, 1011110114.

19. Hahn, J.; Sibener, S. J. Time-Resolved Atomic Force Microscopy Imaging Studies of Asymmetric PS-B-PMMA Ultrathin Films: Dislocation and Disclination Transformations, Defect Mobility, and Evolution of Nanoscale Morphology. *J. Chem. Phys.* **2001**, *114*, 47304740.
20. Hammond, M. R.; Cochran, E.; Fredrickson, G. H.; Kramer, E. J. Temperature Dependence of Order, Disorder, and Defects in Laterally Confined Diblock Copolymer Cylinder Monolayers. *Macromolecules* **2005**, *38*, 65756585.
21. Segalman, R. A.; Hexemer, A.; Hayward, R. C.; Kramer, E. J. Ordering and Melting of Block Copolymer Spherical Domains in 2 and 3 Dimensions. *Macromolecules* **2003**, *36*, 32723288.
22. Rider, D. A.; Cavicchi, K. A.; Vanderark, L.; Russell, T. P.; Manners, I. Orientationally Controlled Nanoporous Cylindrical Domains in polystyrene-b-poly(ferrocenyl-ethylmethylsilane) Block Copolymer Films. *Macromolecules* **2007**, *40*, 37903796.
23. Harrison, C.; Adamson, D. H.; Trawick, M.; Angelescu, D. E.; Cheng, Z.; Huse, D. A.; Chaikin, P. M.; Vega, D. A.; Sebastian, J. M.; Register, R. A Pattern Coarsening in a 2D Hexagonal System. *Europhys. Lett.* **2004**, *67*, 800806.
24. Cheng, J. Y.; Mayes, A. M.; Ross, C. A. Nanostructure Engineering by Templated Self-Assembly of Block Copolymers. *Nat. Mater.* **2004**, *3*, 823828.
25. Hammond, M. R.; Sides, S. W.; Fredrickson, G. H.; Kramer, E. J.; Ruokolainen, J.; Hahn, S. F. Adjustment of Block Copolymer Nanodomain Sizes at Lattice Defect Sites. *Macromolecules* **2003**, *36*, 87128716.
26. Mueller, M.; Katsov, K.; Schick, M. A New Mechanism of Model Membrane Fusion Determined from Monte Carlo Simulation. *Biophys. J.* **2003**, *85*, 16111623.
27. Katsov, K.; Mueller, M.; Schick, M. Field Theoretic Study of Bilayer Membrane Fusion: II. Mechanism of a Stalk-Hole Complex. *Biophys. J.* **2006**, *90*, 915926.
28. Constantin, D.; Oswald, P. Diffusion Coefficients in a Lamellar Lyotropic Phase: Evidence for Defects Connecting the Surfactant Structures. *Phys. Rev. Lett.* **2000**, *85*, 4297.
29. Matsen, M. W. Elastic Properties of a Diblock Copolymer Monolayer and Their Relevance to Bicontinuous Microemulsion. *J. Chem. Phys.* **1999**, *110*, 46584667.

30. Matsen, M. W.; Schick, M. Stable and Unstable Phases of a Linear Multiblock Copolymer Melt. *Macromolecules* **1994**, *27*, 71577163.
31. Knoll, A.; Horvat, A.; Lyakhova, K. S.; Krausch, G.; Sevink, G. J. A.; Zvelindovsky, A. V.; Magerle, R. Phase Behavior in Thin Films of Cylinder-Forming Block Copolymers. *Phys. Rev. Lett.* **2002**, *89*, 035501035501/035504.
32. Horvat, A.; Lyakhova, K. S.; Sevink, G. J. A.; Zvelindovsky, A. V.; Magerle, R. Phase Behavior in Thin Films of Cylinder-Forming ABA Block Copolymers: MesoScale Modeling. *J. Chem. Phys.* **2004**, *120*, 11171126.
33. Huinink, H. P.; van Dijk, M. A.; Brokken-Zijp, J. C. M.; Sevink, G. J. A. Surface-Induced Transitions in Thin Films of Asymmetric Diblock Copolymers. *Macromolecules* **2001**, *34*, 53255330.
34. Tsarkova, L.; Knoll, A.; Krausch, G.; Magerle, R. Substrate-Induced Phase Transitions in Thin Films of Cylinder-Forming Diblock Copolymer Melts. *Macromolecules* **2006**, *39*, 36083615.
35. de Gennes, P. G.; Prost, J. *The Physics of Liquid Crystals*; Clarendon Press: Oxford, U.K., 1993.
36. Chaikin, P. M.; Lubensky, T. C. *Principles of Condensed Matter Physics*; Cambridge University Press: New York, 1995; Chapter 9.
37. Tsarkova, L.; Knoll, A.; Magerle, R. Rapid Transitions between Defect Configurations in a Block Copolymer Melt. *Nano Lett.* **2006**, *6*, 15741577.
38. Knoll, A.; Horvat, A.; Lyakhova, K. S.; Krausch, G.; Sevink, G. J. A.; Zvelindovsky, A. V.; Magerle, R. Direct Imaging and Mesoscale Modelling of Phase Transitions in a Nanostructured Fluid. *Nat. Mater.* **2004**, *3*, 886891.
39. Tsarkova, L.; Horvat, A.; Krausch, G.; Zvelindovsky, A. V.; Sevink, G. J. A.; Magerle, R. Defect Evolution in Block Copolymer Thin Films via Temporal Phase Transitions. *Langmuir* **2006**, *22*, 80898095.
40. Duque, D.; Schick, M. Self-Consistent Field Theory of Twist Grain Boundaries in Block Copolymers. *J. Chem. Phys.* **2000**, *113*, 55255530.
41. SFM movie, see Supporting Information.
42. Simulation movie, see Supporting Information.

43. Horvat, A.; Knoll, A.; Krausch, G.; Tsarkova, L.; Lyakhova, K. S.; Sevink, G. J. A.; Zvelindovsky, A. V.; Magerle, R. Time Evolution of Surface Relief Structures in Thin Block Copolymer Films. *Macromolecules* **2007**, *40*, 69306939.
44. Kim, H.-C.; Russell, T. P. Ordering in Thin Films of Asymmetric Diblock Copolymers. *J. Polym. Sci., Part B* **2001**, *39*, 663668.
45. Lin, Y.; Bker, A.; Sill, K.; Xiang, H.; Abetz, C.; Wang, J.; Emrick, T.; Balazs, A.; Russell, T. P Self-Directed Self-Assembly of Nanoparticle/Copolymer Mixtures. *Nature* **2005**, *434*, 5559.
46. Kim, S. H.; Misner, M. J.; Russell, T. P. Solvent-Induced Ordering in Thin Film Diblock Copolymer/Homopolymer Mixtures. *Adv. Mater.* **2004**, *16*, 21192123.
47. Tsarkova , L. In *Nanostructured Soft Matter:Experiment, Theory, Simulation and Perspectives*. Zvelindovsky, A. V., Ed.; Springer: Heidelberg, Germany, 2007; 231266.
48. Sevink, G. J. A.; Zvelindovsky, A. V.; van Vlimmeren, B. A. C.; Maurits, N. M.; Fraaije, J. Dynamics of Surface Directed Mesophase Formation in Block Copolymer Melts. *J. Chem. Phys.* **1999**, *110*, 22502256.
49. Lyakhova, K. S.; Sevink, G. J. A.; Zvelindovsky, A. V.; Horvat, A.; Magerle, R. Role of Dissimilar Interfaces in Thin Films of Cylinder-Forming Block Copolymers. *J. Chem. Phys.* **2004**, *120*, 11271137.

7 Structural Ordering in Thin Films of Cylinder Forming Block Copolymers

Tsarkova L., **Horvat A.**, Krausch G. and Magerle R.
published as ACS Preprint, 2006

7.1 Introduction

Block copolymers are complex materials which form periodic nanostructures. Expanding applications of ordered microdomains in nanotechnologies^{1–3} are strong incentives for developing an improved understanding of the block copolymer dynamics and control over the ordering of nanopatterned surfaces.

While topological defects in polymer thin films resemble those commonly observed in liquid crystalline^{4–8} or even solid crystalline materials,⁹ block copolymers exhibit a wide spectrum of morphological and dynamic properties that are related to their polymeric nature. It is now well established that cylinder forming block copolymers in confined geometries frequently exhibit non-bulk structures or hybrid morphologies in response to thickness and surface fields constraints.^{10–12} Recently in-situ scanning force microscopy (SFM) has been used to image the phase transition from the cylinder to the perforated lamella (PL) phase in a thin film of a concentrated block copolymer solution.¹³ This work has shown that on large time scales the microdomain dynamics can be described in great detail with a mean-field approach and dynamic density functional theory (DDFT). Furthermore, quantitative analysis of defect motion led to an estimate of the interfacial energy between the cylinder and the perforated lamella (PL) phases.

Here we report on an in-situ investigation of microdomain ordering in a cylinder forming block-copolymer melt. The time resolution of SFM allows the observation of elementary processes of defect motion on a large range of time scales: density undulations on a time scale below a second, collective deformation of microdomains on a timescale of tens of seconds, and temporal morphological structures with the lifetimes ranging from a minute to hours. Computer simulations based on the dynamic density functional theory (DDFT) reproduce the observed temporal phase transitions as a pathway of structural evolution.

7.2 Experimental

7.2.1 Polymer

The material was a polystyrene (PS)-blockpolybutadiene (PB) diblock copolymer (SB) with molecular weights of the PS and PB blocks as 13.6 and 33.7 kg/mol respectively, and a polydispersity of 1.02. The volume fraction of the PS (25.5%) corresponds to bulk morphology of hexagonally ordered cylinders. This was confirmed with SAXS measurements on a bulk specimen: SB forms PS cylinders embedded in a PB matrix with a characteristic distance of 32.9 ± 0.3 nm between the next-nearest cylinders (at 120°C). The glass transition temperature of the homopolymers PB and PS is $T_{g,PB} = -83$ to -107°C and $T_{g,PS} = 80 - 100^\circ\text{C}$ correspondingly.¹⁴

7.2.2 Scanning Force Microscopy (SFM)

In-situ thermal annealing and scanning were performed under a flow of dry nitrogen in a SFM heating stage (*MultiMode*, DI/Veeco Metrology Group) allowing for precise control of both the sample and the tip temperature. Standard silicon cantilevers (with the resonance frequency in the range of 200-300 kHz) have been used for the tapping mode scanning under an amplitude setpoint of ~ 0.96 . No measurable effect of the tip on the structural evolution has been detected. With custom built software¹⁵ the continuously saved SFM phase images were flattened, registered and compiled into a movie.

7.2.3 Experimental conditions

SB film with a thickness of about 50 nm was prepared by spincoating of a 1.2 wt% SB solution in toluene on a carbon coated silicon substrate. Stabilizer was added in amount 0,03% of the polymer weight to prevent cross linking of the PB block during the thermal annealing. A 6 ± 1 nm carbon layer was evaporated onto a silicon wafer using a Cressington 208HR sputter coater. The sample was mounted into the *Multimode* heating stage, first annealed at 140°C for 40 minutes and then quenched to 105°C for SFM imaging. At these temperatures the combined Flory-Huggins parameter χN is about 30-35^{16,17} which corresponds to the intermediate segregation regime.¹⁸

7.2.4 Simulations

We have modeled the thin film behavior of cylinder forming block copolymer using the Mesodyn code which is based on mean-field dynamic density functional theory (DDFT). A melt

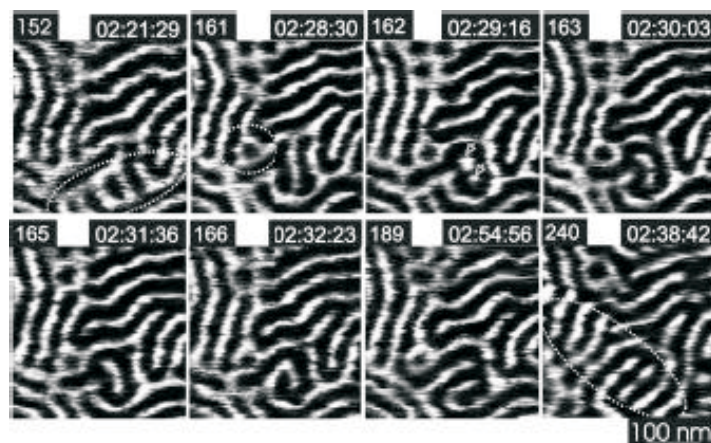


Figure 1: Selected frames from a continuously saved sequence of SFM phase images. The labels indicate the number of the frame and the elapsed time of the imaging. The frames show the annihilation of a small elongated grain (Frame 152) which is replaced on a time-scale of ~ 70 minutes by another small grain with the perpendicular orientation (Frame 240). The transient dotlike structures are indicated by arrows in Frame 162. The temporal PL phase (marked by a circle in Frame 161) with a lifetime of ~ 60 min can be seen in the following frames with shape undulations (Frames 163 and 166) or different number of connected cylinders (Frames 163 and 189).

of $A_3B_{12}A_3$ Gaussian chains was used as a model system. A and B correspond to PS and PB in experiments, correspondingly. For the bead-bead interaction potential a Gaussian kernel is used, which is characterized by ϵ_{AB} and related to Flory-Huggins parameter χN . The value of ϵ_{AB} was set to 6.5 kJ/mol in order to have cylinders as the bulk structure.¹⁹ It corresponds to $\chi N \sim 35$, analogous to the experiment (see above). A substrate supported thin film (with one free surface) was modeled as in Ref.20 Here the interaction with the hard wall (substrate) was set to be -3 kJ/mol. The interactions with the void component were set to $\epsilon_{VA} = 16$ kJ/mol and $\epsilon_{VB} = 10$ kJ/mol. The film has the possibility to change its height. All other parameters are same as in Ref.19

7.3 Results

7.3.1 Transient perforated lamella phase (experiment)

In-situ imaging reveals small patches of non bulk PL phase that appear during structural rearrangements. Few examples of transient PL structures with different life-times and different cluster size are presented in Figures 1 and 2.

Often we observe structural defects in the cylinder phase such as a single PL ring (see an

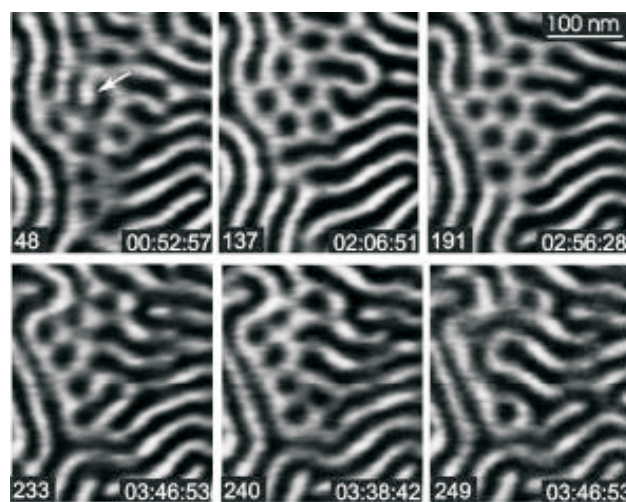


Figure 2: Crops from selected frames showing the transient PL phase at the boundary between the cylinder grains. In Frame 48, an array of PL rings is aligned along the grain boundary and grouped around a horse-shoe defect. In Frame 249 the transient phase is annihilated into the $+1/2$ disclination. The total evolution of the PL phase is about four hours.

example in Frame 161 of Figure 1). Such single PL rings generally originate from three-arms connections between cylinders and can be considered as a minimal nucleus of the PL phase during the cylinder to PL phase transition.¹³ In our case, the formation of the single PL ring appears to be an elementary process of annihilation of the small elongated grain (shown in Frame 152). This local PL cell existed over a time period of ~ 60 minutes, however with different numbers of connected cylinders (compare Frames 161 and 189) and periodic breaks in its structure prior to the annihilation of this defect.

Figure 2 presents the four hours lasting evolution of a cluster of the PL rings at the boundary between the cylinder grains. Initially, an array of PL rings was aligned along the grain boundary and grouped around a horse-shoe defect (Frame 48). The elementary processes of the PL phase evolution, such as additional connections between cylinders (Frame 137), the movement of kinks parallel to the cylinder/PL border (Frame 233) are very similar to that observed earlier during the cylinder to PL phase transition in a swollen film of a triblock copolymer.¹³ The final annihilation into the $+1/2$ disclination (Frame 249) proceeded in less than 5 minutes, much faster than the life-time of this temporal phase.

7.3.2 Transient perforated lamella phase (simulations)

Figure 3 captures the reorientation of a cylindrical grain via the formation and annihilation of the PL phase. The initial film thickness was chosen to be 1.5 microdomain spacing in order

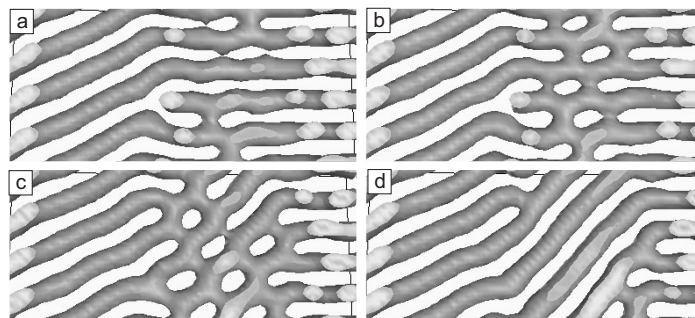


Figure 3: *Snapshots of the MesoDyn simulations, which model a thin supported film of a $A_3B_{12}A_3$ cylinder forming block copolymer in a $128 \times 32 \times 26$ simulation box. Crops of the middle layer, visualizing the reorientation of cylinders via the transient PL phase are shown after a) 56 000, b) 57 200, c) 58 400 and d) 59 600 time steps. The thin film morphology is shown by the isodensity surface of A component for a threshold value of $\rho_A = 0.33$.*

to accelerate terrace formation in a natural way similar to the experiment. In the simulation, the initially flat film shows perpendicular cylinders and cylinders with necks facing the wetting layer. After 8000 time steps the film starts to roughen. Simultaneously, in the lower terrace the structures transform into lying cylinders. After 30 000 simulation steps the second layer of lying cylinders starts to form via interconnection of necks. At 56 000 time steps the film shows two layers of cylinders on top of the wetting layer. Remarkably, on a small patch the cylinder orientation of the top layer and that of the bottom layer do not match each other. The relative disorientation is about 60° . The following adjustment of the bottom layer to the orientation of the cylinder layer above it is captured in Figure 3. First, the undulations of interfacial walls and developing dislocation are visible (Figure 3a). The newly forming connections between neighboring cylinders serve as nucleation centers for the PL domains (Figure 3b). The PL patch grows via the undulations in cylindrical domains which eventually connect to form the PL lattice sites (Figure 3c). Presumably, the domains of the PL phase support redistribution of local densities. Finally, the microdomains reorganize into new cylinder orientation (Figure 3d).

From earlier in-situ experiments we know, that the real experimental time of ~ 1 s can be assigned to one simulation step.¹³ This estimate suggest that in this particular simulation the reorganization of cylinders proceeds on a time scale of tens of minutes (3 600 time steps), which is in a good agreement with experimental observations.

7.4 Discussion

Our studies of the phase behavior in SB films demonstrated that on carbon coated substrates the PL phase is stabilized at transition film thickness, either at the bottom of a step or in areas with minor thickness variation.¹² The characteristic spacing of the PL phase was shown to be $\sim 10\%$ larger compared to that of the cylinder phase. The morphological phase transition from the cylinder to the PL phase provides a local adjustment of the microdomain structures under the thickness constraint. In-situ dynamic measurements in similar SB films melts demonstrate that annihilation of topological defects in many instances proceeds via local temporal phase transitions. The low interfacial tension of $\sim 2.5 \mu\text{Nm}^{-1}$ between the cylinder and the PL phase¹³ is likely to account for the energetically favorable pathway of structural rearrangements via temporal phase transitions and explains the stabilization of PL patches under long term annealing in highly defective areas of the cylinder phase. We remark, that the phase transitions from metastable to equilibrium morphologies as well as thermally reversible order-order transitions have been extensively studied before.^{21–24} Here we describe local excited states in the equilibrium phase that are induced by energetically unfavorable defect configurations.

The simulations conceptually match the experimentally observed ordering and growth of grains of cylinders via temporal phase transitions. We emphasize that the simulation method is not biased to any particular microdomain structure and has no a priori knowledge of the macroscopic mechanisms of structural transitions. All structures form spontaneously from an initially homogeneous polymer mixture and the structural evolution proceeds through the pathways determined by its natural diffusion dynamics.

Acknowledgements

This work was supported by the Deutsche Forschungsgemeinschaft (SFB 481). R. M. acknowledges support from the VolkswagenStiftung. L.T. and A.H. acknowledge support from the HWP-Program.

References

1. Park, M.; Harrison, C.; Chaikin, P. M.; Register, R. A.; Adamson, D. H. *Science* **1997**, *276*, 1401-1404.
2. Thurn-Albrecht, T.; Schotter, J.; Kastle, G. A.; Emley, N.; Shibauchi, T.; Krusin-Elbaum, L.; Guarini, K.; Black, C. T.; Tuominen, M. T.; Russell, T. P. *Science* **2000**, *290*, 2126-2129.
3. Park, C.; Yoon, J.; Thomas, E. L. *Polymer* **2003**, *44*, 6725-6760.

4. Harrison, C.; Adamson, D. H.; Cheng, Z.; Sebastian, J. M.; Sethuraman, S.; Huse, D. A.; Register, R. A.; Chaikin, P. M. *Science* **2000**, *290*, 1558-1561.
5. Harrison, C.; Cheng, Z.; Sethuraman, S.; Huse, D. A.; Chaikin, P. M.; Vega, D. A.; Sebastian, J. M.; Register, R. A.; Adamson, D. H. *Phys. Rev. E* **2002**, *66*, 011706-011706.
6. Hammond, M. R.; Cochran, E.; Fredrickson, G. H.; Kramer, E. J. *Macromolecules* **2005**, *38*, 6575-6585.
7. Segalman, R.; Hexemer, A.; Kramer, E. *Phys. Rev. Lett.* **2003**, *91*, 196101.
8. Segalman, R. A.; Hexemer, A.; Hayward, R. C.; Kramer, E. J. *Macromolecules* **2003**, *36*, 3272-3288.
9. Rehse, N.; Knoll, A.; Konrad, M.; Magerle, R.; Krausch, G. *Phys. Rev. Lett.* **2001**, *87*, 035505.
10. Knoll, A.; Horvat, A.; Lyakhova, K. S.; Krausch, G.; Sevink, G. J. A.; Zvelindovsky, A. V.; Magerle, R. *Phys. Rev. Lett.* **2002**, *89*, 035501.
11. Knoll, A.; Magerle, R.; Krausch, G. *J. Chem. Phys.* **2004**, *120*, 1105-1116.
12. Tsarkova, L.; Knoll, A.; Krausch, G.; Magerle, R. *Macromolecules* **2006**, Web Release Date: 30 April 2006.
13. Knoll, A.; Horvat, A.; Lyakhova, K. S.; Krausch, G.; Sevink, G. J. A.; Zvelindovsky, A. V.; Magerle, R. *Nature Materials* **2004**, *3*, 886-891.
14. Brandrup, J.; Immergut, E. H.; Grulke, E. A., Eds. *Polymer handbook*, 4th ed.; J. Wiley & Sons: New York, 1999.
15. Knoll, A. Ph.D. Thesis; Universitt Bayreuth, Germany, 2003.
16. Owens, J. N.; Gancarz, I. S.; Koberstein, J. T.; Russell, T. P. *Macromolecules* **1989**, *22*, 3380-3387.
17. Sakurai, S.; Mori, K.; Okawara, A.; Kimishima, K.; Hashimoto, T. *Macromolecules* **1992**, *25*, 2679-2691.
18. Fredrickson, G. H.; Bates, F. S. *Annu. Rev. Mat. Sci.* **1996**, *26*, 501-550.
19. Horvat, A.; Lyakhova, K. S.; Sevink, G. J. A.; Zvelindovsky, A. V.; Magerle, R. *J. Chem. Phys.* **2004**, *120*, 1117-1126.

Publications

20. Lyakhova, K. S.; Horvat, A.; Sevink, G. J. A.; Zvelindovsky, A. V. *Langmuir* **2006**, in press.
21. Sakurai, S.; Momii, T.; Taie, K.; Shibayama, M.; Nomura, S.; Hashimoto, T. *Macromolecules* **1993**, *26*, 485-491.
22. Hajduk, D. A.; Ho, R.-M.; Hillmyer, M. A.; Bates, F. S.; Almdal, K. *J. Phys. Chem. B* **1998**, *102*, 1356-1363.
23. Kimishima, K.; Koga, T.; Hashimoto, T. *Macromolecules* **2000**, *33*, 968-977.
24. Sota, N.; Sakamoto, N.; Saijo, K.; Hashimoto, T. *Macromolecules* **2003**, *36*, 4534-4543.

8 Time evolution of surface relief structures in thin block copolymer films

Horvat A., Knoll A., Krausch G., Tsarkova L., Lyakhova K. S., Sevink G. J. A, Zvelindovsky A. V. and Magerle R.
published in **Macromolecules**, 2007, 40, 6930-6939.

The dynamics of early stage of terrace formation in thin supported films of cylinder forming triblock copolymers was studied both theoretically using self-consistent-field theory (DSCFT) and experimentally by insitu scanning force microscopy (SFM). In experiment, an initially flat film of incommensurable thickness was imaged continuously, and the evolution of a vertical orientation of cylinders into a parallel one as well as the respective development of thickness gradient (terrace formation) was captured in detail. On the grounds of these experimental observations, the parameters of the computational model $A_3B_{12}A_3$ were determined to match the structures in experiment. Both systems show excellent agreement in details of structural phase transitions and in the dynamics of the step development, suggesting that the underlying transport mechanisms are governed by diffusion. The early stage of terrace formation is characterized by the development of the step height up to 80% of its equilibrium value and associated reorientation of cylindrical domains.

8.1 Introduction

Block copolymers belong to the class of ordered fluids, which self-assemble into microdomains with characteristic lengths ranging from 10 to 100 nm. The morphology type and the characteristic dimensions are controlled by the block copolymer composition, the interaction between the blocks, and by the total chain length N .¹

The specific behavior of block copolymers in thin films is primarily dictated by the enhanced role of surface/interfacial energetics, as well as by the interplay between the characteristic block copolymer spacings and the film thickness.²⁻⁵ Preferential attraction of one of the blocks to the surface breaks the symmetry of the structure and favors layering of microdomains parallel to the surface plane through the entire film thickness. As a result the energetically favored film

thicknesses are then quantized with the characteristic structure period in the bulk (denoted here as c_0 for cylinder-forming block copolymers). The surface topography depends on the initial film thickness h_0 of as-cast substrate-supported film. When h_0 deviates from nc_0 (for symmetric wetting conditions), topographical features of macroscopic size such as islands, holes or bicontinuous patterns with two distinct thicknesses nc_0 and $(n + 1)c_0$ are formed to satisfy the thickness constraint. Experimentally, nucleation and subsequent growth of surface relief structures, also called **terrace formation**, have been investigated mostly for lamellar systems as a function of surface fields,^{6–8} molecular architecture,⁹ film thickness,^{10,11} and annealing conditions.^{9,11,12}

The coarsening of the surface macrodomains is typically followed by time-resolved optical micrographs or surface force microscopy (SFM) topographs, and the averaged macrodomain radius as a function of annealing conditions is determined. The development of surface roughness on an initially smooth film starts already during the early stages of annealing. The terrace heights continuously change with time until the commensurable thicknesses are achieved. The difference in the neighboring terraces heights up to 80% of its equilibrium value was shown to develop already during the early stage of terrace formation.¹³ On a longer time scale, the pattern of terraces is still coarsening. This process is due to the effective line tension of the two-dimensional islands (holes) which tends to minimize the total length of the terrace edges with time. However, on a smaller length scale (a few microdomain spacings), the film thickness and the step profile can be considered constant. An extended summary of these studies can be found in recent reviews.^{5,14–16}

It is now well established that a cylinder-forming block copolymer under confinement and strong surface fields forms microstructures that deviate from that of the corresponding bulk material. Surface structures like lamella (L), perforated lamella (PL), perpendicular cylinders (C_{\perp}), cylinders with necks ($C_{\parallel}C_{\perp}$), spheres on a top of a perforated lamella (PL-S) are examples of simulated^{17–19} and experimentally observed morphologies^{20–26} that are formed in thin films of bulk cylinder-forming block copolymers. While the equilibrium structures in thin films of block copolymer have widely been investigated, the dynamics of nanostructured fluids in thin films are an issue of a recent interest.^{27,28}

The modelling part of this paper was inspired by unique *in-situ* SFM measurements of terrace formation, where both the macroscale development of the thickness gradient and the related microscale phase transitions were resolved. The calculational method based on the Dynamic Self-Consistent Field Theory (DSCFT), originally proposed by Fraaije,²⁹ has been previously used to model the pattern formation in confined environment. The calculations matched the SFM experiments in great detail. The computational method provides decisive understanding of the experimental results as it allows more extensive variation of the system parameters than

one could achieve in experiments. In our earlier work we identified deviations from the cylinder bulk morphology as surface reconstructions²⁴ and constructed phase diagrams which allow to distinguish between surface field and confinement effects.^{18,19,24} In recent study we found that the *dynamics* of elementary structural transition in experiment and simulation well accord. We demonstrated that DSCFT describes the microdomain dynamics on long time scales in great detail.²⁷ Furthermore, quantitative analysis of defect motion led to an estimate of the interfacial energy between the cylinder and the PL phases.

In our previous work³⁰ we have introduced a DSCFT-based model of a block copolymer film with a free surface, and considered the dynamics of terrace development. Here, we rationalize the parametrization choice of this earlier study and focus on a detailed quantitative comparison of the early stage of terrace formation with the actual experiment. The paper is organized as follows: First, we introduce the computational model of free surface and related parameters. Next we describe continuous *in-situ* SFM measurements of the dynamics of the surface relief structures and phase transitions in thin triblock copolymer film under solvent annealing. Then we present the results of the parametrization of the model system aiming to match the experimentally observed structures. Finally, we analyze and compare the development of the thickness variation (terrace formation) and the related phase transitions in computational simulation and in *in-situ* experiment and discuss the underlying mechanisms.

8.2 Method

8.2.1 Theoretical model

The mesoscopic DSCFT employs a coarse-grained field description of the polymer system. The free energy, however, is based on a microscopic Hamiltonian and therefore explicitly incorporates the specificity of the polymer chain. Furthermore, we use a separation of scales and consider a time scale at which, for given fields, the polymer chains are fully relaxed. The field dynamics is then given by a standard set of stochastic Langevin equations, where the stochastic terms represent mesoscopic fluctuations, according to the fluctuation-dissipation theorem. An overview, and details of this type of method, can be found in refs 29 and 31. The chain conformations at each point in time are specified by fields, and the dynamic equations for the fields describe the collective diffusive dynamics of the polymer system; hydrodynamic effects are neglected. We remark that hydrodynamic phenomena are known to play only a minor role in the evolution of many systems, in particular in dense block copolymer systems.

In the following we shortly review the DSCFT that was also used in our earlier experimen-

tal/computational studies^{24,27,30,45} and discuss the coarse-grained variables and parameters we have chosen for the model.

Molecular model and the free energy functional

An ideal Gaussian chain is used as molecular model in the microscopic Hamiltonian. The chemical composition of the polymer molecule is reflected by beads of different types, labelled by the index I . On a coarse grained level, the microstructure patterns of polymeric systems are described by the density fields $\rho_I(\mathbf{r})$. We consider a system of volume V which contains n molecules of the length N . The free energy for such a system can be expressed as:

$$F[\rho] = -kT \ln \Psi^n / n! - \sum_I \int_V U_I(\mathbf{r}) \rho_I(\mathbf{r}) d\mathbf{r} + F^{nid}[\rho] \quad (8.1)$$

Here Ψ is the partition function for the ideal Gaussian chain of the length N in the external fields U_I . The external potentials U_I and the density fields ρ_I are bijectively related³² in a self-consistent way via a density functional for the Gaussian chain.³³ F^{nid} is the contribution due to the non-ideal mean-field interactions. For the cohesive interaction between the beads a Gaussian kernel is used:

$$\varepsilon_{IJ}(\mathbf{r} - \mathbf{r}') \equiv \varepsilon_{IJ}^0 \left(\frac{3}{2\pi a^2} \right)^{3/2} e^{-\frac{3(\mathbf{r} - \mathbf{r}')^2}{2a^2}}.$$

The strength of the interaction, ε_{IJ}^0 (in kJ/mol) is directly related to the Flory-Huggins parameter ($\chi_{IJ} = 1000\varepsilon_{IJ}^0 / N_a kT$). The input to the free energy functional is:

$$F^{coh}[\rho] = \frac{1}{2} \sum_{I,J} \int_V \int_V \varepsilon_{IJ}(\mathbf{r} - \mathbf{r}') \rho_I(\mathbf{r}) \rho_J(\mathbf{r}') d\mathbf{r} d\mathbf{r}' \quad (8.2)$$

The compressibility of the system is included via:

$$F^e[\rho] = \frac{k_H}{2} \int_V \left(\sum_I v_I (\rho_I(\mathbf{r}) - \rho_I^0) \right)^2 d\mathbf{r} \quad (8.3)$$

Here k_H is Helfand coefficient, ρ_I^0 is the average concentration of the component I , and v_I is the bead volume.

Solid substrate

The solid surfaces are treated like hard walls also called "mask fields", which constrain a thin film by keeping the flux perpendicular to the substrate equal zero.^{34,35} In the unconstrained directions, periodic boundary conditions are used. The interactions with the masks are taken

into account in the same way as the interaction between the beads. The surface field induced term in F^{nid} is:

$$F^{surf}[\rho] = \frac{1}{2} \sum_{\alpha} \sum_I \int_V \int_V \epsilon_{IM\alpha}(|\mathbf{r} - \mathbf{r}'|) \rho_I(\mathbf{r}) \rho_{M\alpha}(\mathbf{r}') d\mathbf{r} d\mathbf{r}' \quad (8.4)$$

where $\rho_{M\alpha}(\mathbf{r}')$ describes the position of the mask ($\rho_{M\alpha}(\mathbf{r}')$ is equal 1 if \mathbf{r}' belongs to the mask, or 0 if \mathbf{r}' belongs to the polymer film).

The free surface

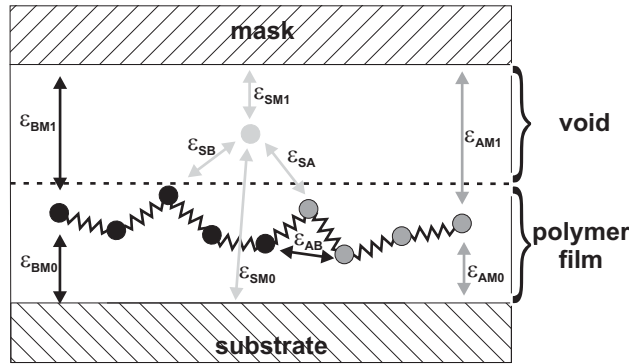


Figure 1: Schematic representation of the simulation setup. The corresponding interactions between system components are indicated by arrows. Block copolymer molecule is represented by the beads-and-springs model. An A_5B_4 molecule is shown for simplicity.

The free surface is created via introducing a void component. The void component is treated as a single-bead bad solvent.^{30,36} Initially, the block copolymer film is macroscopically phase separated from the void component. The interactions with this void component are taken into account in the same way as the interaction between the polymer beads (via additional interaction parameters ϵ_{IS}).

Input configuration

The numerical schemes explicitly consider the external potential fields U_I ³³ instead of the density fields. Therefore the input densities ρ_I^{input} can not be imported directly. They are generated by iterative optimization of $U_I(\mathbf{r})$ with initial values $U_I(\mathbf{r}) = 0$ prior to the application of the dynamic scheme. An update of the external potentials is accepted when the difference between the input densities ρ_I^{input} and $\rho_I(U_I)$ is smaller than some preset value $\delta \ll 1$.

Dynamic equations

The thermodynamic forces, that drive the phase separation and the structure formation, are local gradients in the intrinsic chemical potential. The chemical potentials are derived from the functional differentiation of the free energy

$$\mu_I(\mathbf{r}) = \frac{\delta F}{\delta \rho_I(\mathbf{r})} \quad (8.5)$$

We assume a diffusive dynamics of the density fields and solve the Langevin diffusion equations numerically:

$$\frac{\partial \rho_I}{\partial t} = M_I \nabla \cdot \rho_I \nabla \mu_I + \eta_I \quad (8.6)$$

where M_I is a constant mobility of bead I (diffusion coefficient) and η_I is a thermal noise, distributed according to the fluctuation-dissipation theorem.

8.2.2 Simulation parameters of the free surface model

General considerations

To model the behavior of supported block copolymer films we use the following starting configuration. Two masks M_0 and M_1 confine the simulation box from top and from bottom, respectively. The lower half of the box is occupied by the block copolymer film, while the upper half is the void component. Initially, the copolymer film is flat. The boundary between the void phase and the polymer film corresponds to a free surface and is expected to show undulation instabilities.³⁶ The model system is schematically represented in Figure 1. The simulation parameters of choice are the initial height of the film and the pairwise interaction parameters (see Figure 1). There are altogether nine interaction parameters: the interaction parameter between the polymer beads ϵ_{AB} , the interaction parameters of the polymer beads with the void component ϵ_{AS} and ϵ_{BS} , the interaction parameters of the polymer beads with the lower (ϵ_{AM_0} and ϵ_{BM_0}) and with the upper mask (ϵ_{AM_1} , ϵ_{BM_1}), and the interactions between the void component and the two masks (ϵ_{SM_0} , ϵ_{SM_1}). In the following part we describe the determined choice of each parameter.

Molecular model

Both the Gaussian chain topology ($A_3B_{12}A_3$) and the interaction parameter between the polymer beads ϵ_{AB} (6.5 kJ/mol) are the same as in our earlier comparative theoretical^{18,19,30} and experimental studies.^{24,25,27}

Interaction of the polymer beads with the substrate

In the earlier works^{18,24} on thin films we have shown that the calculated structures with the effective surface interaction $\epsilon_M = \epsilon_{AM_0} - \epsilon_{BM_0}$ of 6 – 7 kJ/mol match in great detail the experimentally observed structures.

Interaction of the polymer beads with the void component

The values of ϵ_{AS} and ϵ_{BS} determine the interaction of the polymer beads with the void component and are analogous to the surface tension of the block copolymer components in experiments. They can be calculated directly from the surface tension values of the polymers.^{37–39} However, due to the extra constraints resulting from the periodic boundary conditions this approach is not effective, as it was shown in our previous publication.³⁰ Therefore, we determine the values of ϵ_{AS} and ϵ_{BS} by a parametrization procedure (see section 8.3.2). As a starting point, we assume the difference $\epsilon_{AS} - \epsilon_{BS}$ to be similar to the effective surface interaction in a slit (6 – 7 kJ/mol).¹⁸

Simulation box

We set the initial thickness to the incommensurable situation corresponding to 1.5 layers of cylinders, analogous to the experiment. The height of the simulation box is set to be twice the film thickness and, additionally, two grid units are occupied by the mask fields. Lateral dimensions of 128×32 grid units are chosen to keep the computational time within reasonable limits.

Film setup

In order to avoid floatening of the film from the substrate, we set the void-upper mask M_1 interaction to a negative value (attractive) and the void-bottom mask M_0 interaction to a positive value (repulsive). Additionally, the polymer beads are repelled from the upper mask. For this purpose we set $\epsilon_{SM_1} = -4 \text{ kJ/mol}$ and $\epsilon_{AM_1} = \epsilon_{BM_1} = \epsilon_{SM_0} = 8 \text{ kJ/mol}$.

Time scale

In our previous paper²⁷ one simulation step was calculated to be about 6 seconds of the experimental measurement time. We assume the time scaling to be of the same order of magnitude in the present setup with the void component. Under this assumption, calculations over 30000 time steps are comparable to an experimental annealing of the SBS film for several hours, when well developed terraces are observed.

Notation

Structure notations used in the present study are similar to that in our previous works³⁰ and are summarized in Table 1.

<i>structure</i>	<i>notation</i>
perpendicular cylinders	C_{\perp}
short perpendicular cylinders, spheres	S
one layer of parallel cylinders	$C_{\parallel,1}$
two layers of parallel cylinders	$C_{\parallel,2}$
three layers of parallel cylinders	$C_{\parallel,3}$
parallel cylinders with necks to the polymer-air interface	$C_{\parallel}C_{\perp}$
parallel cylinders with necks to the substrate	$C_{\perp}C_{\parallel}$
wetting layer	W
perforated lamellae	PL
lamellae	L
coexistence of structures in one layer	*/*
coexistence of separate layers with different structures	* - *

Table 8.1: Structure notation

8.2.3 Experiment

Sample preparation

As an experimental reference system we studied a thin film of a polystyrene-*block*-polybutadiene-*block*-polystyrene (SBS) triblock copolymer (from Polymer Source Inc.) with weight averaged molecular weights of the polystyrene (PS) blocks of $M_{W,PS} = 14 \text{ kg/mol}$ and $M_{W,PS} = 15 \text{ kg/mol}$ and of the polybutadiene (PB) block of $M_{W,PB} = 73 \text{ kg/mol}$. The glass-transition temperatures of the respective homopolymers range from -83 to $-107 \text{ }^{\circ}\text{C}$ for PB and from 80 to $100 \text{ }^{\circ}\text{C}$ for PS.⁴⁰ The surface tension of PB, $\gamma_{(PB)} = 31 \text{ mN/m}$, is considerably smaller than the surface tension of PS, $\gamma_{(PS)} = 41 \text{ mN/m}$.⁴⁰ A $70 \pm 2 \text{ nm}$ thick film was spin cast from a toluene solution onto a silicon substrate. The sample was placed in a fluid cell of a Multimode SFM (Digital Instruments, Veeco Group) and exposed to a controlled chloroform vapor.²⁵ The chloroform vapor pressure was adjusted to set the polymer volume concentration in the film to $\phi = 0.73$. In bulk, at this concentration SBS forms cylinders with a characteristic spacing of $39.0 \pm 0.5 \text{ nm}$.²⁵

SFM imaging and movie

The changes in the surface topography and in the microdomain structure have been followed with *in-situ* scanning force microscopy (SFM) using standard silicon cantilevers (with a resonance frequency of 300-kHz; Nanosensors) in tapping mode. Light tapping conditions resulted in a phase contrast of 2° . The acquisition rate for a $4 \times 4 \mu\text{m}^2$ -image (512×512 pixels) was 2.5 min per image. The resulting SFM images were flattened, registered, corrected for image distortion and compiled into an SFM-movie⁴¹ using a home made software. Because of a rather large thermal drift, the analysis of the same spot of the sample is possible only by picking a small area of one frame and tracking it into earlier and later frames. The movie⁴¹ covers 6.75 h of annealing the SBS film under controlled vapor pressure and captures the early stage of terrace formation. For further experimental details see Ref. 13, 25 and 27.

Comparative dimensions

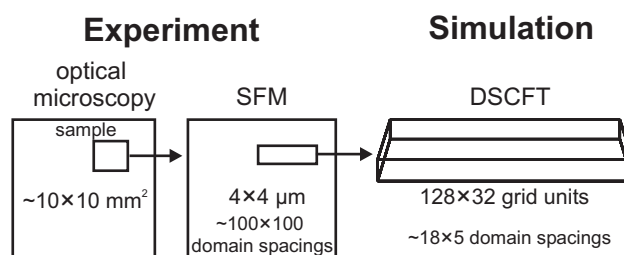


Figure 2: Schematic comparison of typical lateral scales that are covered in experimental measurements (optical microscopy and surface force microscopy) and in our simulation box.

Figure 2 compares the sample dimensions of the experiment with that of the computational simulation. In experiments a typical film surface area available for the optical microscopy or SFM measurements is about a square centimeter with an averaged terrace size of about several μm^2 . In SBS films, each terrace accommodates in the lateral direction up to several hundreds of microdomains.

8.3 Results

8.3.1 Film evolution in experiment

The detailed phase behavior in SBS films after annealing in a neutral solvent has recently been studied at varied thickness and polymer content in a swollen film.²⁵ The initial dry film thickness ($\sim 70 \text{ nm}$) and annealing vapor pressure were chosen in accordance with the phase diagram of

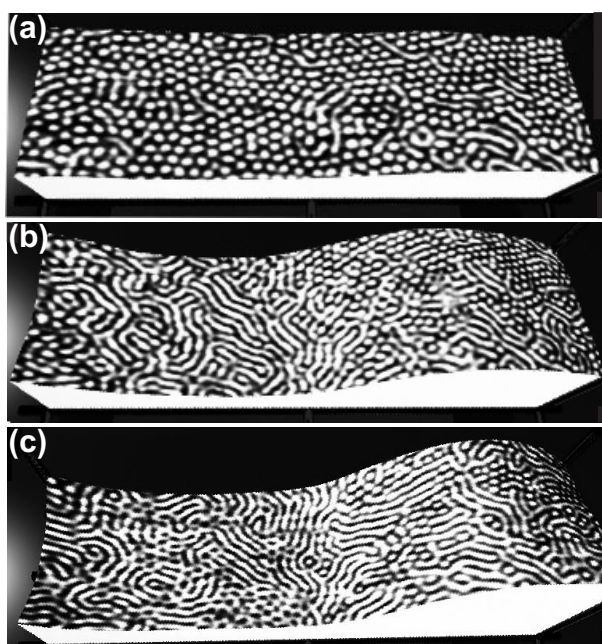


Figure 3: *Snapshots of the in-situ SFM movie ($0.675 \times 2.625 \mu\text{m}$) illustrating the dynamics of terrace formation at (a) 0.5 h, (b) 4 h, and (c) 6.75 h of annealing in solvent vapor. 3D pictures are constructed by using the height image as a topography and the phase image as a texture. The SFM movie can be found in supporting information [40]*

this polymer such as to make the thickness of the swollen film (at polymer volume fraction $\phi_p = 0.73$) equal to 1.5 layers of cylindrical structures. These films of incommensurable thickness are not stable upon annealing and form terraces with one and two layers of structures. As it was shown earlier in Ref.25 the PL structure is expected within the lower terrace, while the second terrace shows a cylindrical structure ($C_{\parallel,2}$). Perpendicular cylinders (C_{\perp}) are stabilized at the transition region between these terraces.

In the dynamic measurements described below, we start with the initially smooth spin-coated film. The associated microstructure (a random coexistence of white stripes, lying polystyrene cylinders C_{\parallel} and white dots without a long-range order, presumably perpendicular cylinders C_{\perp} ²⁵) is formed during the spin-coating procedure by the fast removal of the solvent. The initial stage of the surface-relief-structure development upon annealing was imaged with *in-situ* SFM, and the data was processed into a SFM-movie⁴¹. Below we describe in detail the observed evolution of the local thickness gradient (terrace formation) and the accompanying phase transitions.

Figure 3 displays the SFM movie snapshots which correspond to 0.5 h (a), 4 h (b), and 6.75 h (c) of annealing. At the initial stage of annealing the swollen SBS film already shows a slight height modulation (Figure 3(a)). As can be followed in the SFM movie⁴¹ the microstructure development proceeds first via ordering of dots into a hexagonally-ordered pattern. During the

time interval between 3 h and 5 h the bright PS dots rearrange into bright PS stripes (C_{\parallel}) within the lower terrace (see Figure 3(b)). Afterward, the PS-rich cylinders transform into PL (dark dots in bright matrix) (Figure 3(c)). The C_{\parallel} to PL phase transition takes about 10 hours and has been described recently in great detail for constrained film thickness.²⁷ Here we focus on the first 7 h of the structure development upon annealing, where the thickness gradient develops gradually and the step height reaches about 80% of its equilibrium value.

It should be noted that the interpretation of the structures in the SFM phase images can not be done unequivocal. In particular, the bright dots can be associated with the C_{\perp} structure, as well as with the hybrid structures, such as $C_{\parallel}C_{\perp}$ with the necks facing the free surface. Structure information provided by the SFM technique is limited to information of the upper film layer. Computational modeling, however, provides direct structural information throughout the polymer film and thereby complements and extends the SFM experiment. On the other side, the experimental data can be used to coordinate and parameterize the theoretical model. Moreover, searching in the parameter space allows to study the effect of the system parameters at a much wider range than is typically available in experiments.

8.3.2 Simulation setup versus Experiment

We performed a number of simulation runs in order to match the structures and transitions observed in the experiment.⁴¹ In particular, we varied the interaction of the blocks with the surface and with the void component. The choice of the parameter range is based on the considerations presented earlier in the parametrization section 8.2. The studied systems are summarized in Table 8.2.

<i>run</i>	ϵ_{SA} kJ/mol	ϵ_{SB} kJ/mol	ϵ_{AM0} kJ/mol	ϵ_{BM0} kJ/mol	H grid units
<i>A</i>	17	10	3	-4	9
<i>B</i>	16	10	2	-4	9
<i>C</i>	16	9.5	3	-4.5	9
<i>D</i>	16	9.5	12	0	9
<i>E</i>	16	9.5	0	3	12

Table 8.2: Parameter sets of simulations

Figure 4(b) presents a structure analysis of the calculation results after 30000 time steps for these particular systems. For comparison, we have included data for a wedge shaped slit (symmetric case $\epsilon_M = 6$, first column in Figure 4(b))¹⁸, which we had found to match the equilibrium behavior of SBS films in great detail²⁴. In these simulations, a thickness gradient is imposed and the structure adjusts to this varying height. For the parameter set A (Table 8.2) the

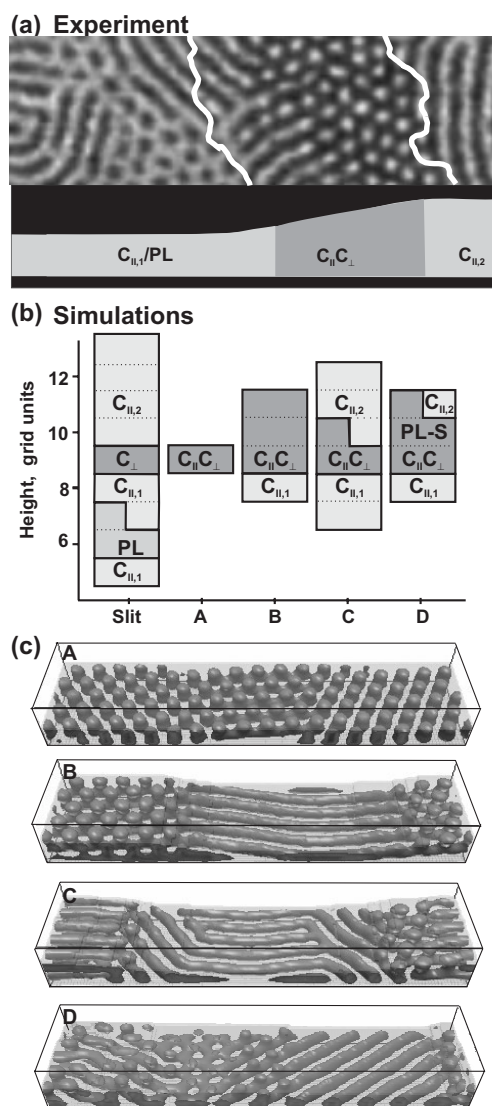


Figure 4: (a) SFM phase image of a slope between the first and the second terraces in SBS film which have been equilibrated in the solvent vapor during 7 h [24]. The sketch below the image illustrate the observed sequence of the morphologies at the commensurable and intermediate thicknesses. (b) Calculated diagram of the system structure vs. height (thickness) for the systems A-D (Table 8.2) after 30000 time steps. The system in a slit from Ref. [18] is shown as a reference only. (c) Simulated structures for the systems A-D shown in (b). Gray structure is the A-component (isodensity level $\rho_A = 0.42$); transparent gray volume indicates the film topography (isodensity level of polymer is larger than 0.9)

void/polymer interface (the free surface of the film) remains flat after 30000 time steps. $C_{\parallel}C_{\perp}$ structures are stable for this thickness. For the slit system an equivalent surface structure (C_{\perp}) is found for this particular film thickness. At a slightly reduced interaction of the bead A with the void component ($\epsilon_{SA} = 16$ instead of 17) and with the substrate ($\epsilon_{AM_0} = 2$ instead of 3) (parameter set B) the film shows pronounced surface roughening. A depression associated with one layer of parallel cylinders ($C_{\parallel,1}$) is formed in the middle of the simulation box. For the other thicknesses in the box the $C_{\parallel}C_{\perp}$ is found. In the parameter set C (Table 8.2) the selectivity of the surface and of the substrate to the blocks are slightly increased, still yielding the structures similar to that in system B. However, the formation of a second layer of cylinders is promoted by the joining necks (Figure 4(c), parameter set C). Additionally, defects appear in the lower terrace. These T-junctions are known to serve as nucleation centers for the PL-phase.²⁷

For the parameter set D (where the surface field value $\epsilon_{AM_0} - \epsilon_{BM_0}$ is increased) the free surface of the film also shows roughening. At the lowest thickness a $C_{\parallel,1}$ structure appears. At intermediate thickness, the film shows a mixture of $C_{\parallel}C_{\perp}$ and of one layer of a perforated lamella with weakly segregated drops on top of it (PL-S). At the largest thickness, a small amount of $C_{\parallel,2}$ develops.

Although systems B to D reproduce the experimental results reasonably well (Fig 4(c)), the structures formed in the case of the parameter set C after 30000 time steps fit the experimental heights and the slope structures (Fig 4(a)) the best. Moreover, the parameter set C is comparable to the matching simulation in the earlier slit study.²⁴

Earlier, height measurements in SBS films suggested an additional layer of material underneath the film, which corroborated the existence of a wetting layer everywhere at the film substrate interface.²⁵ Further development of the computational model was done by introducing a wetting layer next to the substrate (parameter set E). The interactions with the void component are the same as in the system C . The interactions with the substrate are set to $\epsilon_{MA} = 0$ and $\epsilon_{MB} = 3$ in order to get wetting layer.¹⁸ In addition, the initial height of the polymer film is increased to 12 grid units (box size $128 \times 32 \times 26$). Due to the wetting layer, this initial thickness corresponds to 1.5 layers of cylinders. System E shows structures similar to the system C in the presence of an A -rich wetting layer. The comparison of these two systems provides insight into the possible role of the wetting layer on structure formation and microdomain dynamics. In the remainder we refer to the calculation with parameter set C as "the simulation without wetting layer", and the simulation with parameter set E "the simulation with wetting layer".

8.3.3 Film evolution in simulation

Both systems were simulated up to 100 000 time steps. Within the first 200 – 1000 time steps, the formation of A - and B -rich layers is initiated by the solid surface in the initially flat and

homogeneous film. Next, the in-plane separation takes place. In the system without wetting layer the film forms parallel cylinders near the substrate and droplets of the A -rich phase next to the free surface. The droplets connect with cylinders, and thus a transition to $C_{\parallel}C_{\perp}$ takes place. In the system with the wetting layer the A component preferentially covers the surface causing an unstructured wetting layer. The two layers above this wetting layer interconnect and form C_{\perp} , rather than $C_{\parallel}C_{\perp}$ as in the system without wetting layer. Since the dynamics of structure formation immediately after microphase separation can not be compared with our *in-situ* SFM experiment, where the structure is affected by the spin-coating process, we will not focus on the very first stages (below 5000 time steps). We note that the early stage of structure formation has been recently described for a system analogous to the system D (Table 8.2).³⁰

Simulation without wetting layer

The dynamics of thickness gradient formation and structure development for the system C is captured as a movie⁴², and analyzed in Figure 5. The simulated structures and heights are analyzed from the same region in the middle and along the longest axis of the simulation box each 5000 steps. Gray levels indicate different structures. The borders between the structures are determined by visual analysis, and therefore are drawn arbitrarily. As a reference we also present iso-height⁴³ lines (in black). Examples of the structural evolution are shown as simulation snapshots at the indicated time steps.

With time, the amplitude of the thickness fluctuations becomes sufficient to induce terrace formation. After 8000-9000 time steps we observe in the thinnest region a structural transition to one layer of cylinders. In the regions with higher film thickness after 20000 time steps two layers of parallel cylinders are formed. Together with a small decrease of the film thickness, the PL phase appears at the lower terrace of the film (after 40000 time steps). As the thickness of the lower terrace decreases further, the PL phase first changes to one layer of defect-free cylinders and later to a disordered layer. The height lines on the graph (Figure 5) accord with the contour lines of the phase regions. The approximate borders are 10.5 grid units for the transition between $C_{\parallel,2}$ and $C_{\parallel}C_{\perp}$; 8.5 grid units for $C_{\parallel}C_{\perp}$ to $C_{\parallel,1}$; 4.5 grid units for the $C_{\parallel,1}$ to disordered phase. The structures below 4.5 grid units can be divided into two regions. Between 4.5 and 2.5 grids the film is unstructured (phase separated material with no symmetry) and below 2.5 grids the system is disordered/mixed. The PL structure and the $C_{\parallel,1}$ structure coexist at a certain film thicknesses and time conditions, like in the experiment.

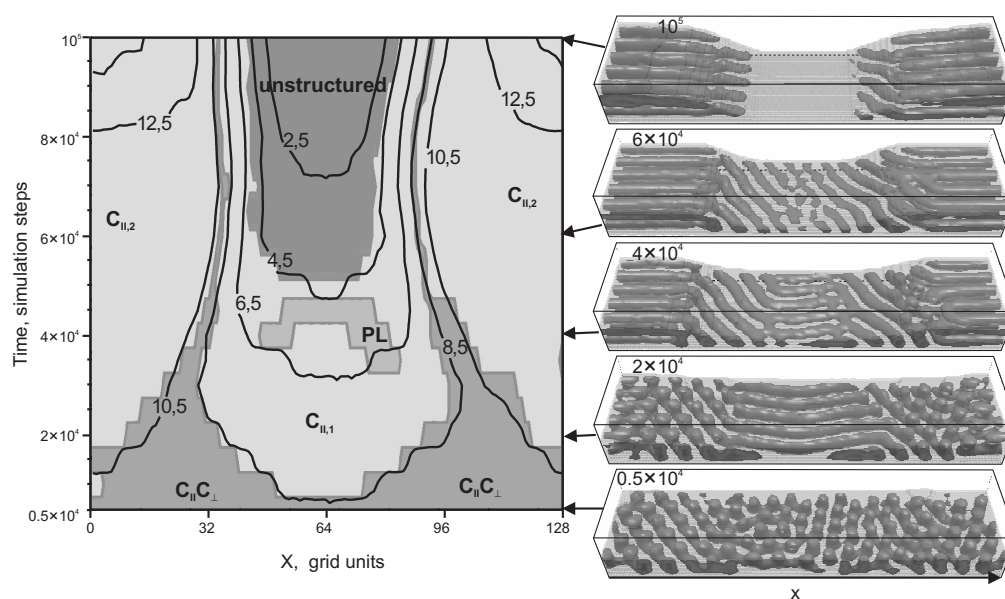


Figure 5: *Graphic representation of the film structure and corresponding heights as a function of time for the system without wetting layer. Different tints of gray correspond to indicated structures; the black lines are the isoheight lines. Right-hand pictures are representative examples of simulation snapshots as indicated by arrows. The movie⁴² can be found in Supporting Information.*

Simulation with wetting layer

Generally, transitions in the system with wetting layer (asymmetric wetting conditions) are similar to the system described above (see ref 44). However, in the presence of the wetting layer, the C_{\perp} structure is formed initially, in contrast to the $C_{||}C_{\perp}$ structure in the system without wetting layer. Indeed, after the transition to $C_{||,1}$ in the lower terrace has taken place, the remaining C_{\perp} interconnect to form $C_{||}C_{\perp}$ structures. When increasing the local thickness after 30000 time steps the $C_{||}C_{\perp}$ changes to $C_{||,2}$. At the same time the order of the cylinders in the thinner part of the film (in the first terrace) is improved. As the difference in local heights increases, necks start to form on the top of $C_{||,2}$, indicating a transition to $C_{||,3}$ (90000 time steps). The $C_{||,1}$ phase becomes thinner and less phase separated. Importantly, the PL phase was not observed. This result is in a good agreement with the experiments on thin films of SB diblock copolymer, which is a structural analogue of SBS triblock copolymer. In this study the PL phase was stabilized under symmetric wetting conditions and was not observed in SB films with a wetting layer.²⁶

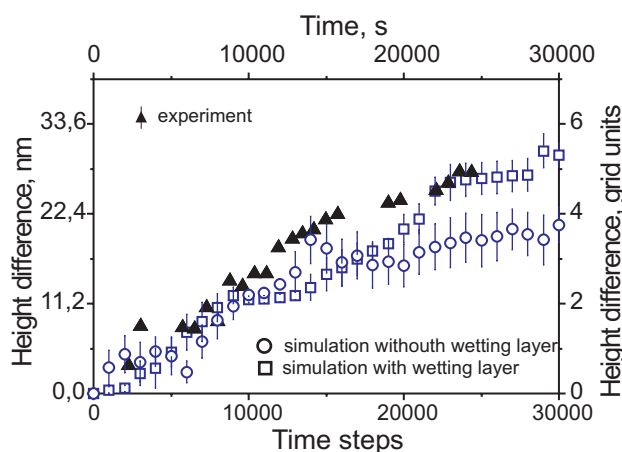


Figure 6: *The difference between the maximum and the minimum heights on the free surface in simulations [open symbols] (right-hand axis) and in experiment [black triangles] (left-hand axis) plotted as a function of the simulation time (bottom axis) and annealing time (top axis), respectively.*

8.4 Discussion

We focus on the evolution of local morphology and its relationship to thickness and terrace formation in block copolymer films of incommensurate height. The time-elapsed SFM measurements are compared to the numerical modeling using DSCFT. It should be noted that the latter approach does not directly explore the microscopic dynamics of chain motion. As mentioned before, DSCFT rather describes the evolution of density fields, under the conditions that diffusion/relaxation of single (coarse-grained) chains within the field is rapid compared to the coordinated motion of many chains. The good match between the film development in simulations and in the experimental annealing suggests that the kinetic model in DSCFT is applicable. In particular, on time scales beyond single chain relaxation, where this coarse-grained approach is valid, this model adequately describes the microdomain dynamics in the experimental system. Moreover, the computational method allows for a time-resolved study of the morphology of the film beyond the surface layer to which the experimental studies are limited.

8.4.1 Comparison of simulation and experiment

Dynamics of surface relief structures

Both in experiment and in simulations, the structural transition is accompanied by a change in local height of the film. In Figure 6 we compare the step height, the difference between the maximum height on the top of the island and minimum height inside the hole, as a function of time in experiment and in simulations for the systems with and without wetting layer. At the

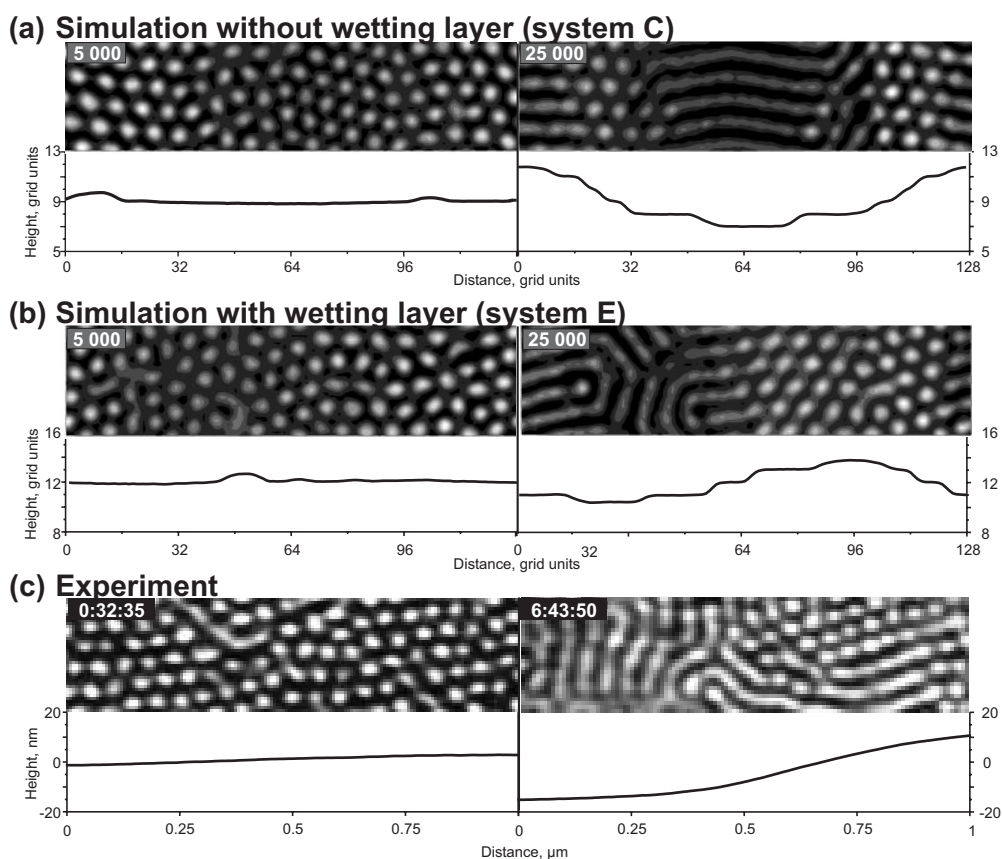


Figure 7: Simulation snapshots showing system C (a) and system E (b) from Table 8.2 at indicated time steps. The surface structures are calculated as the average density of A-component over the top two layers. Plotted heights are determined as described in Ref.43. (c) Snapshots from the SFM movie showing the surface structures (phase image of Taping mode SFM) and surface topography of the same spot on the terrace slope at indicated annealing time.

early stage of terrace formation the two simulation systems show structural transitions similar to that in the experiment. The relation between the experimental heights and grid units was determined beforehand from the comparison of bulk spacings in experiment and in the calculation (1 grid unit corresponds to 5.6 nm).¹⁸

The time axis was scaled by matching the simulation and the experimental graphs. The best fit is found for 1 computational time step = 0.8 – 1 s of real experimental time (on the graph we use 1 step equaling 1 s). Our comparison merely focusses on the early stage of terrace formation where phase transitions are the same in the experiment and in the simulations.

The results of structure calculation are shown after 5000 and 25000 time steps in Figure 7(a-b) in a form of surface structures imaged with SFM.³⁰ In Figure 7(c) the same spot on the slope between the neighboring terraces in the experimental system is shown after 0.5 h and 6.75 h of annealing. The height difference after 6.75 h of annealing is ~ 27 nm corresponding to about 80% of the equilibrium step height. Along the pathway the initial bright dots transform to bright stripes and small patches of dark dots at thinner regions. They can be interpreted as a PL phase.²⁴ At intermediate thickness, bright dots are the dominating structures. At the largest thickness white stripes are formed. The comparison of surface structures in Figure 7(a-b) and (c) suggests that the initial white-dots pattern as well as the dots-and-stripes pattern after 25000 time steps in the simulations (see Fig 7(a-b)) are similar to the experimental images after 0.5 and 6.75 h of vapor treatment Fig 7(c)).

The dots-to-stripes transition represents the transition from C_{\perp} and $C_{\parallel}C_{\perp}$ to $C_{\parallel,1}$ in the lower terrace or to $C_{\parallel,2}$ in the upper terrace. The details of these transitions in the experiment and in the simulations are considered below.

$C_{\perp}/C_{\parallel}C_{\perp}$ -to- $C_{\parallel,1}$ transition

The pathway of the experimental dots-to-stripes transition in the lower terrace is shown in Figure 8(a). The details of the underlying structure transition, away from the air-polymer interface can be extracted from the simulation results.

In the system without the wetting layer, the $C_{\parallel}C_{\perp}$ transforms into modulated or elongated cylinders. A further decrease of the film thickness in the middle of the hole leads to the development of $C_{\parallel,1}$. The distance between the lying cylinders in $C_{\parallel}C_{\perp}$ and in $C_{\parallel,1}$ is the same, therefore large scale reorientation is redundant for matching the natural lateral domain spacing. The spacing between the dots (necks) is about 15% larger ($\frac{2}{\sqrt{3}}a_0$) than the spacing of lying cylinders a_0 (due to the hexagonal packing).²³ The necks can form a perfect hexagonal matrix even if the underlying cylinders form separate grains which orient 60° (or 120°) to each other.

For the system with wetting layer the upright cylinders (C_{\perp}) first elongate in the plane of the film toward the neighboring cylinders and finally coalesce. They form lying cylinders ei-

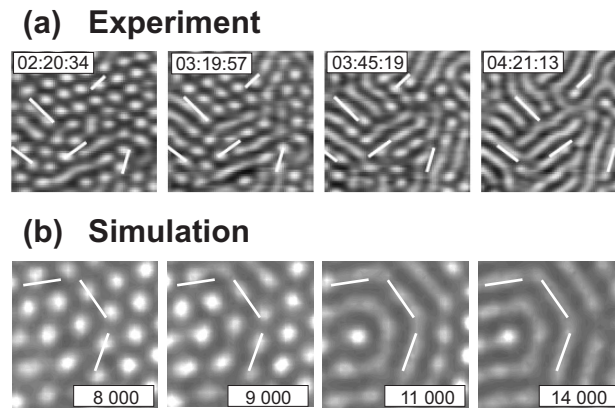


Figure 8: (a) Experimental snapshots at indicated times of solvent vapor annealing showing the dots-to-stripes phase transition. (b) Simulation snapshots of the surface structures (see Figure 7) for the system with wetting layer from Figure 6 showing the C_{\perp} -to- C_{\parallel} phase transition. The time steps are indicated at the bottom of the images. In (a) and (b) white bars are drawn parallel to the cylinders in the last image of each sequence and are superimposed onto the earlier images as a guide to eye to illustrate the structure development

ther directly or via intermediate structure of modulated cylinders (cylinders with necks). The connection between C_{\perp} cylinders initially appears preferentially at grain boundaries in the C_{\perp} structure (or at defects), and serves as a nucleus of the new $C_{\parallel,1}$ structure. The top view of this transition is shown in Figure 8(b). Comparing the directions of the grains in the C_{\parallel} phase to the direction of the grains in the earlier C_{\perp} phase we detect a rotation of the cylinders. The whole grain of parallel cylinders rotate by an angle of approximately 10° . The final grain size is typically no larger than 3 to 4 cylinder spacings.

We find that the initial structure (C_{\perp} or $C_{\parallel}C_{\perp}$) strongly influences the resulting C_{\parallel} phase. If the transition proceeds by interconnecting perpendicular cylinders, the spacing of the in-plane cylinders will only be $c_0 = \frac{\sqrt{3}}{2}a_0$. The initial grains of the C_{\parallel} phase are therefore formed with an unfavorably reduced spacing of the cylinders. This affects the further growth of the $C_{\parallel,1}$ phase. The C_{\perp} structure cannot simply transform into the C_{\parallel} structure by interconnecting cylinders without inducing strain. Therefore the transition is slow (compared to $C_{\parallel}C_{\perp}$ -to- C_{\parallel}), and starts from several nuclei close to each other. The outcome is a much smaller grain size of the C_{\parallel} phase in comparison to the C_{\perp} grain size before transition. The grains try to relax their spacing by rotating the cylinders in the plane of the film. The rotation in the system with wetting layer is similar to the mechanism observed in the experiment (Figure 8); therefore we concluded, that white dots in SFM images correspond to perpendicular oriented cylinders rather than to cylinders with necks.

The structural transition shown in Figure 8 takes place in about two hours of the experimental

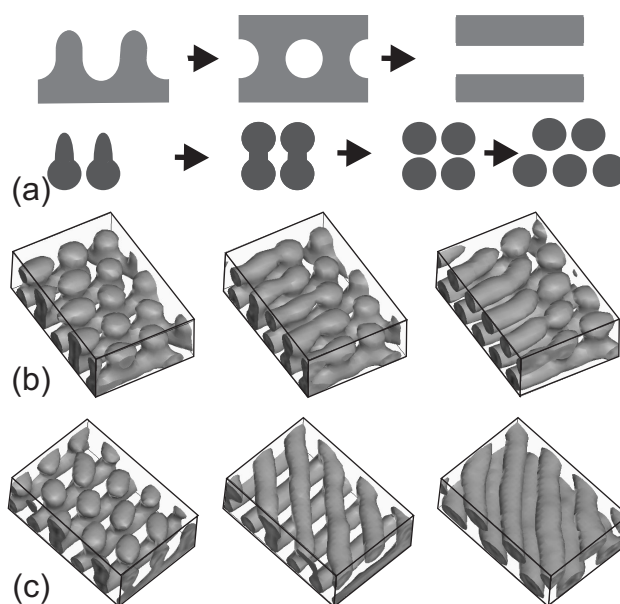


Figure 9: (a) Schematic representation of the $C_{\parallel}C_{\perp}$ -to- $C_{\parallel,2}$ transition shown as a side view (top row) and as a front view (bottom row); (b) simulation snapshots of the system C (Table 1) after 19000, 22000 and 30000 time steps (from left to right); (c) simulation snapshots of the system E (Table 1) after 43600, 47000 and 60000 time steps (from left to right).

time and in ~ 6000 simulation steps. Therefore the time scale is the same as the time scale obtained from terrace growth (1 simulation step ~ 1 s of real time), showing good consistency with the dynamics of surface topography.

$C_{\perp}/C_{\parallel}C_{\perp}$ -to- $C_{\parallel,2}$ transition

Another type of dots-to-stripes transition is a transition to two layers of lying cylinders. In the simulation, the formation of the second layer proceeds only from the $C_{\parallel}C_{\perp}$ phase. The schematic details of this transition are shown in Figure 9(a). When the film height reaches 11 grid units (14 grid units in the system with wetting layer), the deformed necks interconnect and a ladder-like structure is formed (see the second sketch in Figure 9(a)). The interconnection of $C_{\parallel}C_{\perp}$ to $C_{\parallel,2}$ starts either parallel to the cylinders in the bottom layer (Figure 9(b)) or under an angle of 60° (Figure 9(c)). As the structure evolves, the connections between the necks can be broken and formed again. The lifespan of this process is 1000 simulation steps, which corresponds to 10 minutes of the experimental time. This meets the experimental observation of the same phenomena, where fluctuations are visible at successive SFM scans (which also takes some minutes between reconnections). Cylinders in the layers adjust their position in the space to achieve hexagonal packing. The transformation requires translational (Figure 9(b)) or

rotational (Figure 9(c)) rearrangement of cylinders on a large scale. In the example shown on Figure 9(c) the reorientation takes place via formation of a transient perforated lamella phase.⁴⁵

At the late stage of the terrace development the C_{\perp} structure has disappeared, and the $C_{\parallel}C_{\perp}$ persists only at the intermediate thicknesses between one and two layers of cylinders.

8.4.2 Mechanisms of transitions, early and late stages

It was experimentally demonstrated that the behavior of supported thin films of block copolymers involve multiple time and length scales. On the one hand the microphase separation and structure formation in the block copolymer phase occur on a short time scale (typically seconds or minutes) and cover distances of some tens of nanometers.^{45,46} Terrace formation is a much slower process (typically hours) involving material transport over micrometer range. In this work we focus on the early stage of terrace formation. In the studied cylinder-forming systems this stage is associated with considerable development of the height difference (up to 80% of the equilibrium step height) and related structure transitions.

We observe a spontaneous splitting of the initially homogeneous film thickness into continuously developing terraces with different heights. Height change and structural transitions are inseparable. Moreover, the pathways of the $C_{\perp}/C_{\parallel}C_{\perp}$ -to- $C_{\parallel,2}$ and $C_{\perp}/C_{\parallel}C_{\perp}$ -to- $C_{\parallel,1}$ transitions suggest the diffusion of block copolymer chains along the structure interface. We distinguish phase transitions which occur at constant height: (C_{\parallel} -to-PL and PL-to- C_{\parallel}). The formation of an intermediate PL phase enhances the connectivity and enables the defect annihilation or reorientation of whole domains (C_{\parallel} -to-PL-to- C_{\parallel}).⁴⁵

We conclude that in the early stage of terrace formation interconnected structures/defects in domain-edges are of great importance. In contrast to lamella forming block copolymers,¹⁰ in cylinder forming systems the $C_{\parallel}C_{\perp}$ structures are natural channels for the material transport between the lower and the upper terraces.

The late stages of terrace formation have recently been investigated.^{7,28,47} In particular, the kinetics of the late-stage islands growth was described as Ostwald ripening process. Three mechanisms were suggested to describe the kinetics of surface relief development (the movement of individual islands)⁷: diffusional movement of whole islands, tunneling of individual block copolymer chains between layers (for the lamellar system) and flow of individual chains through defects in the structure. It was concluded that the flow of block copolymer chains through the defect structures is the primary mechanism for the late stages of island development.⁷ Recently, the material transport mechanisms between terraces in cylinder forming block copolymer film were investigated theoretically and experimentally,⁴⁸ and the time dependence of the flow at later stages was found to be diffusion-like. For the systems studied here it was shown earlier that the terrace formation at later stage is dominated by coalescence

of surface structures and microdomains ordering.²⁷

Finally, we remark that the development of an ultrathin disordered layer in the simulation movie 2 (system C) at late time steps resembles the droplet formation (or autophobic dewetting). In experimental systems with high chain mobility undesired dewetting leads to the rupture of block copolymer films already at very short experimental time scales (few minutes of annealing). As a result, the formation of the equilibrium microstructures cannot be followed experimentally. To our knowledge, there are no published studies which compare the kinetics of the competitive dynamic processes (terrace formation and dewetting) in block copolymer films. We can only state that both the macrodomain spacings and the orientational order are affected by the shear fields in dewetting rims.^{5,49} Understanding the film stability toward dewetting requires a detailed analysis of several factors, including surface tension and surface field strength. Since the definition of surface tension for nanopatterned surfaces is ambiguous, there is a severe lack of theoretical guidance. The parameter set in system C could serve as a starting point for a detailed computational study on film stability, which is beyond the scope of the present work.

8.5 Conclusions

We have studied terrace formation in a thin film of a cylinder forming block copolymers by a computational DSCFT method and have compared the results with the dynamic SFM measurements of the SBS block copolymer thin films. The complex dynamics exhibited by this system enriches the fundamental understanding self-assembly in block copolymers, highlighting the special relationship between morphology and dynamic processes in thin films.

Apart from the introduction of a free surface via a void component (and relevant new parameters for the free surface interactions) we have chosen a simulational system equal to the one considered in earlier publications.^{18,19,24,27} We have focused on the early stage of terrace formation, where 80% of height changes occur. On the very early stage, not accessible in the experiment, we observe microphase separation and structure formation in the block copolymer film. The formation of the microstructure starts at the substrate. Subsequently, the initially flat film develops terraces. Experimental and simulation results agree that the change of the local height is strongly connected to the changes in the local microstructure. The detailed pathways of the structural transitions, as revealed by simulations, suggest a diffusion of block copolymer chains along the microstructure interfaces and indicate an important role of $C_{\parallel}C_{\perp}$ (necks) structure as material-transport-channel between neighboring terraces in thin cylinder forming films.

Kinetics of both the terrace height growth and the structural transition was found to be quantitatively similar in experiment and in simulations; 1 time step equals 1 s. The accordance

between the simulation and the experiment supports the assumption that the early stage of terrace formation is governed by diffusion.

Acknowledgment

This work was supported by the Deutsche Forschungsgemeinschaft (SFB 481, TP B7 and A9). A.H. thanks the support of the State of Bavaria (HWP-Program).

Supporting Information Available:

SFM movie: In-situ tapping mode SFM movie showing the development of the surface topography and the microdomain structures at early stage of terrace formation in a swollen SBS film with a polymer volume fraction of $\phi = 0.73$. The SFM images were rendered into 3D pictures with Pov-RayTM. The SFM topography images were used as a height field, while the SFM phase signal is represented as a texture. Bright structures correspond to polystyrene component. The movie starts after 5 min of equilibration of the spin-coated SBS film in chloroform vapor pressure. The displayed area is $(2.625 \times 0.675 \times 0.06) \mu\text{m}^3$. The frame rate is 152 s/frame, total capture time is 6 h 45 min.

Simulational movie, system C: Computer simulation (DSCFT method) of the early stage of the surface topography and microstructure development in the system with parameter set C (Table 8.2). For each displayed time step, grey structures represent the microstructure A-component (isodensity level $\rho_A = 0.42$). In addition transparent grey volumes show the film topography (isodensity level of polymer is larger than 0.9). The structure evolution is plotted every 200th time step, for 100000 time steps in total. The dimension of the simulation box is $128 \times 32 \times 20$ grid elements.

Simulational movie, system E: Detailed structural evolution obtained with the computational DSCFT method. The movie shows the early stage of the surface topography and microstructure development in the system with parameter set E (Table 8.2). Grey structures represent the A-component (isodensity level $\rho_A = 0.42$); transparent grey volumes show the film topography (isodensity level of polymer is larger than 0.9). The structure evolution is plotted every 200th time step, for 100000 time steps in total. The dimension of the simulation box is $128 \times 32 \times 26$ grid units.

References and Notes

1. Bates, F. S.; Fredrickson, G. H. *Ann.Rev.Phys.Chem.*, **1990**, *41*, 525–557.
2. Fredrickson, G. H. *Macromolecules*, **1987**, *20*, 2535–2542.
3. Anastasiadis, S. H.; Russell, T. P.; Satija, S. K.; Majkrzak, C. F. *Phys.Rev.Lett.*, **1987**, *62*, 1852–1855.
4. Fasolka, M. J.; Banerjee, P.; Mayes, A. M.; Pickett, G.; Balazs, A. C. *Macromolecules*, **2000**, *33*, 5702–5712.
5. Tsarkova, L. In *Nanostructured Soft Matter: Experiment, Theory, Simulation and Perspectives*, Zvelindovsky, A. V.; Ed.; Springer Verlag: Heidelberg, 2007; p. 226-261.
6. Peters, R. D.; Yang, X. M.; Nealey, P. F. *Macromolecules*, **2002**, *35*, 1822–1834.
7. Heier, J.; Kramer, E. J.; Groenewold, J.; Fredrickson, G. H. *Macromolecules*, **2000**, *33*, 6060–6067.
8. Heier, J.; Sivaniah, E.; Kramer, E. J. *Macromolecules*, **1999**, *32*, 9007–9012.
9. Liu, Y.; Zhao, W.; Zheng, X.; King, A.; Singh, A.; Rafailovich, M. H.; Sokolov, J.; Dai, K. H.; Kramer, E. J.; Schwarz, S. A.; Gebizlioglu, O.; Sinha, S. K. *Macromolecules*, **1994**, *27*, 4000–4010.
10. Carvalho, B. L.; Thomas, E. L. *Phys.Rev.Lett.*, **1994**, *73*, 3321–3324.
11. Menelle, A.; Russell, T. P.; Anastasiadis, S. H.; Satija, S. K.; Majkrzak, C. F. *Phys. Rev. Lett.*, **1992**, *68*, 67–70.
12. Maaloum, M.; Ausserre, D.; Chatenay, D.; Coulon, G.; Gallot, Y. *Phys.Rev.Lett.*, **1992**, *68*, 1575–1578.
13. Knoll, A. Ph.D. thesis, Universität Bayreuth, Bayreuth, Germany, 2003.
14. Segalman, R. A. *Materials Science & Engineering, R: Reports*, **2005**, *R48*, 191–226.
15. Fasolka, M. J.; Mayes, A. M. *Ann. Rev. Mater. Res.*, **2001**, *31*, 323–355.
16. Green, P. F.; Limary, R. *Adv. Coll. & Int. Sci.*, **2001**, *94*, 53–81.
17. Huinink, H. P.; van Dijk, M. A.; Brokken-Zijp, J. C. M.; Sevink, G. J. A. *Macromolecules*, **2001**, *34*, 5325–5330.

18. Horvat, A.; Lyakhova, K. S.; Sevink, G. J. A.; Zvelindovsky, A. V.; Magerle, R. *J. Chem. Phys.*, **2004**, *120*, 1117–1126.
19. Lyakhova, K. S.; Sevink, G. J. A.; Zvelindovsky, A. V.; Horvat, A.; Magerle, R. *J. Chem. Phys.*, **2004**, *120*, 1127–1137.
20. Henkee, C. S.; Thomas, E. L.; Fetters, L. J. *J. Mater. Sci.*, **1988**, *23*, 1685–1694.
21. Radzilowski, L. H.; Carvalho, B. L.; Thomas, E. L. *J. Polym. Sci. Part B*, **1996**, *34*, 3081–3093.
22. Kim, G.; Libera, M. *Macromolecules*, **1998**, *31*, 2569–2577; **1998**, *31*, 2670–2672
23. Konrad, M.; Knoll, A.; Krausch, G.; Magerle, R. *Macromolecules*, **2000**, *33*, 5518–5523.
24. Knoll, A.; Horvat, A.; Lyakhova, K. S.; Krausch, G.; Sevink, G. J. A.; Zvelindovsky, A. V.; Magerle, R. *Phys. Rev. Lett.*, **2002**, *89*, 035501/1–4.
25. Knoll, A.; Magerle, R.; Krausch, G. *J. Chem. Phys.*, **2004**, *120*, 1105–1116.
26. Tsarkova, L.; Knoll, A.; Krausch, G.; Magerle, R. *Macromolecules*, **2006**, *39*, 3608–3615.
27. Knoll, A.; Lyakhova, K. S.; Horvat, A.; Krausch, G.; Sevink, G. J. A.; Zvelindovsky, A. V.; Magerle, R. *Nature Materials*, **2004**, *3*, 886–891.
28. Segalman, R. A.; Schaefer, K. E.; Fredrickson, G. H.; Kramer, E.; Magonov, S. *Macromolecules*, **2003**, *36*, 4498–4506.
29. Fraaije, J. G. E. M. *J. Chem. Phys.*, **1993**, *99*, 9202–9212.
30. Lyakhova, K. S.; Horvat, A.; Zvelindovsky, A. V.; Sevink, G. J. A. *Langmuir*, **2006**, *22*, 5848–5855.
31. Mermin, N. D. *Physical Review*, **1965**, *137*, 1441.
32. Fraaije, J. G. E. M.; van Vlimmeren, B. A. C.; Maurits, N. M.; Postma, M.; Evers, O. A.; Hoffmann, C.; Altevogt, P.; GoldbeckWood, G. *J. Chem. Phys.*, **1997**, *106*, 4260–4269.
33. Sevink, G. J. A.; Zvelindovsky, A. V.; van Vlimmeren, B. A. C.; Maurits, N. M.; Fraaije, J. G. E. M. *J. Chem. Phys.*, **1999**, *110*, 2250–2256.
34. Huinink, H. P.; Brokken-Zijp, J. C. M.; van Dijk, M. A.; Sevink, G. J. A. *J. Chem. Phys.*, **2000**, *112*, 2452–2462.

35. Morita, H.; Kawakatsu, T.; Doi, M. *Macromolecules*, **2001**, *34*, 8777–8783.
36. Helfand, E.; Tagami, Y. *J. Chem. Phys.*, **1972**, *56*, 3592–3601.
37. Broseta, D.; Fredrickson, G. H.; Helfand, E.; Leibler, L. *Macromolecules*, **1990**, *23*, 132–139.
38. Linse, P.; Hatton, T. A. *Langmuir*, **1997**, *13*, 4066–4078.
39. Brandrup, J.; Immergut, E.H.; Grulke, E. A. *Polymer Handbook*, Wiley: New York, 1989.
40. SFM movie. Supporting information is available via the Internet at <http://pubs.acs.org>
41. Simulational movie, system C. Supporting information is available via the Internet at <http://pubs.acs.org>
42. The density field values are only known at the lattice positions (although the calculations themselves are not restricted to the lattice). And we have a steep density gradient between the void component and polymer film. The mixture of these two phases appear only on the boundary. We use the following definition for the interface between void and polymer: $H(x,y) = z - (\rho_S)/(\rho_A + \rho_B + \rho_S) \sim z - \rho_S$, here z is the height where the mixture of void and polymer appears. The height profiles for different y after 5000 simulation steps are similar, the calculated deviations were below 0.5 grid units.
43. Simulational movie, system E. Supporting information is available via the Internet at <http://pubs.acs.org>
44. Tsarkova, L.; Horvat, A.; Krausch, G.; Zvelindovsky, A. V.; Sevink, G. J. A.; Magerle, R. *Langmuir*, **2006**, *22*, 8089–8095.
45. Tsarkova, L.; Knoll, A.; Magerle, R. *Nano Letters*, **2006**, *6*, 1574–1577.
46. Grim, P. C. M.; Nyrkova, I. A.; Semenov, A. N.; Tenbrinke, G.; Hadziioannou, G. *Macromolecules*, **1995**, *28*, 7501–7513.
47. Belyi, V.; Witten, T. *J.Chem.Phys.*, **2004**, *120*, 5476–5485.

9 Summary

In this thesis modeling results on structure formation in thin films of cylinder-forming block copolymers are presented and discussed. The computational study of the equilibrium phase behavior in thin films is complemented by detailed comparison with a real experimental system. Additionally, the dynamics in such films at various length and time scales (the dynamics of individual defects and the dynamics of surface relief structures) is studied. The strength of the presented thesis is the comparison of thin block copolymer film equilibrium and dynamic behavior in experiments and in computer simulations. This comparison supplies an in-depth understanding of the processes in thin films and near the surfaces in thick films and allows to identify the important control parameters of nanopattern formation.

Chapters 4 and 5 report on the phase behavior of thin films of asymmetric block copolymers. In addition to the surface induced alignment of hexagonally ordered cylinders, an adjustment to the planar symmetry of the surface by formation of surface reconstructions is found to dominate the phase behavior in thin films. The large parameter space covered by the simulations allows to distinguish the effects of the two constraints characteristic for thin films: the surface field and the film thickness. The deviations from the bulk cylinder structure, both in the vicinity of surfaces and in thin films are identified as surface reconstructions. The stability regions of different phases are modulated by the film thickness via interference and confinement effects. The results give evidence of a general mechanism that govern the phase behavior in thin films of modulated phases: The interplay between the strength of the surface field and the deformability of the bulk structure determines how the system rearranges in the vicinity of the surface.

Chapters 6 and 7 present a systematic study of defects in thin films of cylinder-forming block copolymers. In particular, the peculiarities of both classical and specific topological are considered in detail, and a strong relationship between the defect structures and the chain mobility in block copolymers is observed. In the systems studied, representative defect configurations provide connectivity of the minority phase in the form of dislocations with a closed cylinder end or classical disclinations with incorporated alternative, nonbulk structures with planar symmetry.

In solvent-annealed films with enhanced chain mobility, the neck defects (bridges between parallel cylinders) were observed. This type of nonsingular defect has not been identified in block copolymer systems before. It is shown, that topological arguments and 2D defect representation, sufficient for lamellar systems, are not sufficient to determine the stability and mobility of defects in the cylindrical phase. *In-situ* scanning force microscopy measurements are compared with the simulations based on DDFT. The close match between experimental measurements and simulation results suggests that the lateral defect motion is diffusion-driven. Finally, the morphological evolution is considered with the focus on the motion and interaction of the representative defect configurations.

Chapter 7 reveals dynamic simulations and in-situ SFM measurements of defect annihilation. Along with the lateral movement of defects, the annihilation frequently proceeds through local structural transitions. The role of the observed structural evolution is discussed in the context of the equilibrium phase behavior of cylinder-forming thin films, studied in chapters 4 and 5.

Chapter 8 presents a study of terrace formation in thin films of a cylinder-forming block copolymers by a computational DDFT method. The results are compared with *in situ* SFM measurements of SBS block copolymer thin films. This chapter focuses on the early stage of terrace formation, where 80% of height changes occur. Experimental and simulation results agree that the change of the local height is strongly connected to the changes in the local microstructure. The detailed pathways of the structural transitions, as revealed by simulations, suggest a diffusion of block copolymer chains along the microstructure interfaces and indicate an important role of cylinders with necks as a material-transport-channel between neighboring terraces in thin cylinder-forming films. Both systems (in experiment and in simulations) show excellent quantitative agreement in detail of structural phase transitions and in the dynamics of the step development, suggesting that the underlying transport mechanisms are governed by diffusion.

Zusammenfassung

In einer Vielzahl von synthetischen und biologischen Materialien führen Selbstordnungsprozesse zu mesoskopischen Strukturen, die die makroskopischen Eigenschaften und, daher auch die Einsatzmöglichkeiten der Materialien entscheidend beeinflussen. Ein Beispiel dafür sind Blockcopolymeren. Hier bilden sich als Folge des Wechselspiels zwischen der Phasenseparation und der Konnektivität der Blöcke regelmäßige mesoskopische Strukturen mit Längenperioden zwischen 5 und 100 nm aus. Für diese Nanostrukturen wurden in den letzten Jahren eine Reihe von neuen Anwendungsmöglichkeiten aufgezeigt. Besondere Beachtung haben dabei dünne Filme gefunden, in denen die Wechselwirkung mit den Grenzflächen nicht nur zu einer Ausrichtung der Domänen führt, sondern auch das Phasenverhalten bereichert. Dünne Filme sind einerseits von Interesse für die Anwendung (zum Beispiel als photonische Kristalle oder für die Lithographie). Andererseits sind sie aber auch hervorragende Modellsysteme für die Grundlagenforschung im Bereich der Oberflächenphysik, da sich die Mikrostruktur in dünnen Filmen und die Dynamik des Strukturbildungsprozesses direkt (im Realraum) visualisieren lassen.

Für eine gezielte Herstellung oder Manipulation von nanometergroßen Strukturen aus Blockcopolymeren ist deren theoretische Beschreibung unabdingbar. Theoretische Beschreibungen bringen Einsicht in den Selbstorganisationprozess und ermöglichen die wichtigen Kontrollparameter der Strukturbildung zu bestimmen. Dies führt zur Rationalisierung der Experimente durch gezielte Auswahl von molekularen Parametern und/oder externer Einflüsse. Andererseits, kann eine theoretische Beschreibung nur durch Experimente auf ihre Gültigkeit überprüft werden.

Im Rahmen dieser Doktorarbeit wurde das Verhalten von Blockcopolymeren mit zylindrischer Volumenmikrodomänenstruktur in dünnen Filmen mit Hilfe einer mesoskopischen Modellierung untersucht. Die Computersimulationen basieren auf einer dynamischen Dichtefunktionaltheorie, mit der sowohl das Gleichgewichtsphasenverhalten als auch die Dynamik im System untersucht werden kann. Als wichtiger Bestandteil der Arbeit wurde ein direkter Vergleich mit den Ergebnissen einer experimentellen Untersuchung eines realen Dünnsfilmsystems – der Charakterisierung der Oberflächenmorphologie per Rasterkraftmikroskop (SFM) – durchgeführt. Die gute Übereinstimmungen zwischen Simulationen und Experimenten im Gleichgewichtsphasenverhalten sowie erste Simulationsergebnisse zur Dynamik gaben dabei Anstoß *in-situ* SFM-Messungen zu etablieren, so dass der Vergleich zwischen Simulationen und Experimenten auch auf die Systemdynamik ausgedehnt werden konnte.

Der erste Teil der Arbeit befasst sich mit Gleichgewichtsstrukturen. Kapitel 4 und 5 enthalten eine systematische Untersuchung des Einflusses der Filmdicke, der Grenzflächen und der Wechselwirkung zwischen den einzelnen Polymerkomponenten auf das Phasenverhalten von Blockcopolymeren in dünnen Filmen. Als Gleichgewichtsstrukturen zeigen sich Zylinder, die

parallel oder senkrecht zur Filmebene ausgerichtet sind, aber auch – in der Nähe der Oberfläche – nicht-zylindrische Morphologien, wie zum Beispiel eine Lamelle oder eine perforierte Lamelle. Diese Abweichungen von der Volumenstruktur werden als *Oberflächenrekonstruktion* identifiziert. Der Stabilitätsbereich einer jeden Struktur ist durch die Filmdicke und die Wechselwirkung zwischen den Polymerkomponenten und den Grenzflächen bestimmt. Der große Parameterraum, der durch die Simulationen abgedeckt wird, erlaubt es, den Effekt dieser beiden Parameter zu trennen. Die gute Übereinstimmung zwischen Simulation und experimentellen Ergebnissen deutet auf ein allgemeines Verhalten in allen Blockcopolymeren mit zylindrischer Volumenmikrodomänenstruktur hin.

Anschließend, wurden die Kinetik der Strukturbildung und entsprechende Transportmechanismen untersucht. Am Beispiel von Defekten und deren Annihilation (Kapitel 6 und 7) wird ein starker Zusammenhang zwischen der Struktur von Defekten und der Kettenmobilität beobachtet. Neben den klassischen Defekten kommen auch die besonderen Eigenschaften der dünnen Polymerfilme zur Geltung: manche Defekte enthalten als Fragmente auch Nicht-Volumenstrukturen, so dass sich die Verbundenheit der Minoritätsphase erhöht. Lokale Abweichungen von der Volumenstruktur können nicht nur durch Oberflächenrekonstruktion verursacht werden, sie dienen auch als temporäre Übergangsstrukturen bei der Annihilation von Defekten.

Schließlich wurde die Anfangsphase der Terrassenentwicklung untersucht (Kapitel 8). Dabei wurde gezeigt, dass Veränderungen der lokalen Höhen mit Phasenübergängen in der lokalen Mikrostruktur verbunden sind. Die genaue Betrachtung des Übergangspfades in den Simulationen lässt darauf schließen, dass sich die Blockcopolymerketten entlang der Struktur Grenzflächen bewegen. Dabei spielt die "Zylinder-mit-Hals"-Morphologie eine wichtige Rolle für den Materialtransport zwischen den Terrassen. Die quantitative Übereinstimmung zwischen Simulationen und experimentellen Ergebnissen deuten darauf hin, dass sowohl die Strukturbildung als auch die Ausrichtung von Domänen durch Diffusion erfolgen.

Die Ergebnisse zeigen, dass die vorgestellte Kombination aus dynamischen Simulationen und *in-situ* SFM-Messungen geeignet ist, das Phasenverhalten von Blockcopolymeren in Realzeit und im dreidimensionalen Realraum zu analysieren. Damit kann diese Kombination als Alternative oder zu mindestens als Ergänzung zu üblichen Streumethoden dienen.

Zusammenfassend betrachtet bietet diese Arbeit einen wichtigen Beitrag zum Verständnis der Strukturbildung und Transportmechanismen in dünnen Filmen phasenseparierter Flüssigkeiten. Die Erkenntnisse können helfen maßgeschneiderte, nanostrukturierte Filme herzustellen.

List of publications

1. Knoll, A.; **Horvat, A.**; Lyakhova, K. S.; Krausch, G.; Sevink, G. J. A.; Zvelindovsky, A. V.; Magerle, R. *Phase behavior in thin films of cylinder-forming block copolymers*, **Phys.Rev.Lett.**, 2002, 89, 035501/1–4.
2. **Horvat, A.**; Lyakhova, K. S.; Sevink, G. J. A.; Zvelindovsky, A. V.; Magerle, R. *Phase behavior in thin films of cylinder-forming ABA block copolymers: mesoscale modeling*, **J.Chem.Phys.**, 2004, 120, 1117–1126.
3. Lyakhova, K. S.; Sevink, G. J. A.; Zvelindovsky, A. V.; **Horvat, A.**; Magerle, R. *Role of dissimilar interfaces in thin films of cylinder-forming block copolymers*, **J.Chem.Phys.**, 2004, 120, 1127–1137.
4. Knoll, A.; Lyakhova, K. S.; **Horvat, A.**; Krausch, G.; Sevink, G. J. A.; Zvelindovsky, A. V.; Magerle, R. *Direct imaging and modeling of phase transitions in a nanostructured fluid*, **Nature Materials**, 2004, 3, 886–891.
5. Tsarkova, L.; **Horvat, A.**; Krausch, G.; Zvelindovsky, A. V.; Sevink, G. J. A.; Magerle, R. *Defect evolution in block copolymer thin films via temporal phase transitions*, **Langmuir**, 2006, 22, 8089–8095.
6. Lyakhova, K. S.; **Horvat, A.**; Zvelindovsky, A. V.; Sevink, G. J. A. *Dynamics of terrace formation in a nanostructured thin block copolymer film*, **Langmuir**, 2006, 22, 5848–5855.
7. Tsarkova, L.; **Horvat, A.**; Krausch, G.; Magerle, R. *Structural ordering in thin films of cylinder forming block copolymers*, PMSE preprint, 232nd ACS National Meeting, San Francisco, 2006, 95.
8. **Horvat, A.**; Knoll, A.; Krausch, G.; Tsarkova, L.; Lyakhova, K. S.; Sevink, G. J. A.; Zvelindovsky, A. V.; Magerle, R. *Time evolution of surface relief structures in thin block copolymer films*, **Macromolecules**, 2007, 40, 6930-6939.
9. **Horvat, A.**; Sevink, G. J. A.; Zvelindovsky, A. V.; Krekhov, A.; Tsarkova, L. *Specific features of defect structure and dynamics in cylinder phase of block copolymers*, **ACS Nano**, 2008, 2, 1143-1452.
10. **Horvat, A.**; Sevink, G. J. A.; Zvelindovsky, A. V.; Tsarkova, L. *Defect structure and dynamics in cylinder phase of block copolymers*, PMSE preprint, 236nd ACS National Meeting, Philadelphia, 2008, 99.

Danksagung

Ich möchte mich ganz herzlich bei all denjenigen bedanken, die zum Gelingen dieser Arbeit beigetragen haben:

An erster Stelle danke ich Herrn Prof. Dr. Georg Krausch (z.Z. Universität Mainz) für das in mich gesetzte Vertrauen und für die Möglichkeit, an seinem Lehrstuhl diese Arbeit anfertigen zu können. Diese Arbeit wäre nicht möglich gewesen ohne seine Unterstützung in vielen, auch nicht-wissenschaftlichen Angelegenheiten.

Ich danke Prof. Dr. Ballauff dafür, dass er für mich das Erstgutachten übernahm.

Prof. Dr. Robert Magerle (z.Z. Universität Chemnitz) hat mein Interesse an dünnen Blockcopolymerfilmen geweckt und deren Modellierung als Thema vorgeschlagen. Er hat die Arbeit während der Anfangsphase betreut und stand mir mit Rat und Tat zu Seite. Mehrere Teile dieser Arbeit sind als Ergebnis zahlreicher gemeinsamer Diskussionen mit ihm entstanden.

Auch Frau Dr. Larisa Tsarkova bin ich in vielerlei Hinsicht zur Dank verpflichtet: Dadurch dass sie die Betreuung der Doktorarbeit übernommen hat, hat sie mir den Wiedereinstieg nach einer längeren Kinderbetreuungspause ermöglicht. Ihre aufmunternde Worte, ihre Zuversicht und Unterstützung gaben mir Kraft in der Endphase. Larisa Tsarkova hat auch durch das Korrekturlesen der Dissertation wesentlich zu deren Verbesserung beigetragen.

Ich danke Agur Sevink und Andrej Zvelindovski für die Bereitstellung und das Anpassen des MesoDyn Codes, aber auch besonders für die Geduld, mit der sie immer meine Fragen beantwortet haben.

Ein großer Dank geht an Armin Knoll für die Bereitstellung von experimentellen Ergebnissen zum Vergleich mit Simulationen und seine ständige Diskussions- und Hilfsbereitschaft.

Ich danke Markus Hund, Helmut Hänsel, Frank Schubert, Kristin Schmidt, Heiko Schobert für eine exzellente Systemadministration und Unterstützung bezüglich aller auftretender Computerprobleme.

Ein besonderer Dank gilt Frau Sybille Zimmermann für die Hilfsbereitschaft in bürokratischen und organisatorischen Belangen und für leckere Süßigkeiten zum Naschen.

Einen riesengroßen Dank gilt allen oben noch nicht erwähnten Leuten die mich während meiner Promotion in der einen oder anderen Weise unterstützt haben und ich hoffe keinen vergessen zu haben: Katya Lyakhova, Alexander Böker, Wolfgang Häfner, Marina Knoll (Lysetska), Nico und Sabine Rehse, Heiko und Ute Zettl, Rasa Beinoraviciute-Kellner, Olga und Thomas Dürrschmidt, Olena Shafransyka und Andrej Voronov, Carmen Kunert, Sabine Ludwigs, Tracy Chun Wang und Gustav Sauer.

Nicht zuletzt danke ich meiner Familie: meinen Eltern für ihre ständige liebevolle Unterstützung; und Hubert, Anna und Stefan für ihre Liebe, Geduld und Verständnis.

Diese Arbeit wurde unter anderem von der DFG über den SFB 481 (Teilprojekte A9 und B7) und über ein Stipendium des HWP-Programms des Freistaates Bayern finanziert.